The Study of Diffusion Dominant Solute Transport in Solid Host Rock for Nuclear Waste Disposal

Submitted by:

Omar Khader

and

Dr. Kent Novakowski

to

Canadian Nuclear Safety Commission

Department of Civil Engineering

Queen's University

Kingston, ON

March 20, 2012
2012

Contract title: *Coordinated Assessment and Research Program on Safety-Related Aspects of a Radioactive Waste Repository in Sedimentary Rock Formation: Natural Tracers*

Contract No.: *87055-08-R413.4*

Omar Khader

PhD candidate, Dept. of Civil Engineering, Queen’s University

Dr. Kent Novakowski

Professor, Dept. of Civil Engineering, Queen’s University

Preface

The project is funded by the Canadian Nuclear Safety Commission (CNSC) to review, study and model natural tracer profiles at the Bruce Deep Geological Repository site in southern Ontario. The purpose is also to review, study and compare similar mathematical modeling on results from two different sites in Europe (Tournemire-France and Benken-Switzerland). The study of natural tracer profiles is based on an understanding of the paleo-hydrogeologic conditions of each site and the construction of a representative mathematical model which describes transport over thousands to hundreds of thousands of years. The report provides the state of understanding on the subject, the results of the study, and suggestions for future work to resolve the uncertainties.

THIS PAGE HAS BEEN LEFT BLANK INTENTIONALLY

Executive Summary

Ontario Power Generation (OPG) is proposing the construction of a Deep Geologic Repository (DGR) at the Bruce nuclear site in southern Ontario for the disposal of Low and Intermediate Level Waste (L&ILW). The repository will be constructed at a depth of about 680 mBGS (below ground surface) in the Paleozoic argillaceous limestone of the Cobourg Formation.

In this report we present a study supported by the Canadian Nuclear and Safety Commission (CNSC) on the interpretation of paleo-hydrogeolgical conditions at three sites using numerical simulation of the distribution of natural tracers. In the study we test the hypothesis that diffusion is the dominant means of solute transport in the low permeability formations of the Bruce site. We combine composition profiles of $\delta^{18}O$ and $\delta^{2}H$ measured in porewater and groundwater samples and the understanding of the paleo-hydrogeologic conditions to test this conceptual model. To do this we have simulated groundwater flow systems developed due to hydraulic head generated from glacial loading and unloading cycles and the effects of this on advective solute transport. The hydro-mechanical loading of the Pleistocene glacial cycles on the Michigan sedimentary basin is assessed using numerical analysis of coupled stress and porewater pressure. The effects of several factors were considered in the analysis of different glacial loading scenarios, including the number of loading cycles, the effect of a wet/dry glacial-soil interface, the effect of glacial advance direction and the effect of the Cambrian aquifer on the development of anomalous pressure heads. The analyses show the change in total head with time within the formations of the Michigan basin under different loading scenarios.

The impact of glaciation and deglaciation on the groundwater flow system was investigated for single 100,000-yr cycles and multiple-cycle scenarios. The results show high porewater pressure developed within the formations during loading periods followed by the development of underpressure during the interstadial periods, especially in the lowest permeability formations. The results also show that the formations have not reached hydrostatic conditions at the present time due to loading cycles that ended around 12000 yrs ago. Our results illustrate the difference in generated total heads in the rock formations between applying mechanical loads on land surface and applying an equivalent hydraulic head. The base case simulations with wet based one glacial loading cycle show that at the present time, regions of underpressures occur in the upper Ordovician and lower Silurian formations characterized by very low hydraulic conductivity and adjacent to the Cambrian aquifer. These results were verified by comparison to measured environmental heads from the Bruce site. To achieve this simulation result, it was necessary to allow draining from aquitards to the Cambrian layer by having an outcrop to the Cambrian layer to dissipate high porewater pressure and the use of wet base glacial loading. This study presents a tool to evaluate the

effects of future glacial events on long term performance of a nuclear waste deep geological repository.

Furthermore, upscaling flow and solute transport parameters measured at field or lab scale to the large spatial and temporal scale of nuclear waste disposal in deep geological formations means the use of these parameters to model the evolution time of natural isotopes profiles. The evolution time should fall in a plausible hydro-geological range. Natural isotopes of water ($\delta^{18}O$ and $\delta^{2}H$) were determined from rock samples extracted from six deep boreholes at the Bruce site (Southern Ontario, Canada) by using vacuum distillation at 150°C (Hobbs et al., 2008). Also diffusion coefficients were measured using X-ray radiographic technique and diffusion cells and hydraulic testing (pulse, slug, and drill-stem tests) for hydraulic conductivities (Raven et al., 2011). The Bruce site falls at the Eastern edge of the Michigan basin. The domain Paleozoic sedimentary rocks have a thickness of 860 m, and divided into 38 different layers of a sequence of dolostones, limestones and shale (Raven et al., 2011). The domain is characterized by anomalous pressures measured in different deep boreholes. The domain is bounded by the Cambrian aquifer from the bottom and 150 m of conductive layers at the top, and characterized by conductive horizontal layers at depths of 180 and 320 mBGS (Below Ground Surface).

We performed a series of diffusion and advection & diffusion models and compared the results with the natural isotopes profiles. Initial and boundary conditions evolution time agrees with hydro-geological history. This confirms that parameters measured at small scales are plausible for formation scale. The results also show the important of advection on solute transport from the upper and lower boundaries. The activation time was reduced by an order of magnitude when taking the effect of advection transport.

The report consists of five sections, the content of these sections are summarized as follows. The 1st section presents an introduction to the issues addressed in the report and the objectives of the study. The 2nd section presents the Hydro-Mechanical model analyses of the Michigan Basin under past glacial loading cycles. The 3rd section presents the solute transport model and analyses for the Bruce site. The 4th section presents an analytical model for diffusion dominant solute transport in a finite domain that can be used to assist in the discretization of numerical models. The 5th section presents the main findings, Conclusions, and recommended future work. The report also includes four appendices. The 1st appendix presents the verification of Hydro-Mechanical model. The 2nd appendix presents the verification of the numerical solute transport model. The 3rd appendix presents the mathematical details of the new analytical model. The 4th appendix includes a FORTRAN model built on the analytical model and its verification. The 5th appendix includes natural isotopes raw data measured in deep boreholes.

TABLE OF CONTENTS

LIST OF FIGURES

LIST OF TABLES

THIS PAGE HAS BEEN LEFT BLANK INTENTIONALLY

1 Introduction

1.1 Waste disposal in bedrock

Since the discovery of radioactivity at the end of the 19th century, the applications of radioactive isotopes have become a part of our daily life in many different fields. Those activities produce radioactive wastes, which emit ionising radiation that is potentially harmful to health and the environment. The protection of living beings against these radiations is achieved fundamentally by incorporating suitable barriers between source and potential receptors (ENRESA, 2006).

The deep subsurface has inherently favourable features for high level waste (HLW) disposal, and is the most extensively studied disposal option presently considered around the world. There is widespread consensus about the merits of this option (Kari, 1997). Geological disposal is considered an effective way to isolate HLW from the human environment using current technologies and without requiring any long-term active control. This is internationally accepted and forms the backbone of HLW management programs in most countries (NUMO, 2002a). The main arguments put forward are that deep disposal can sufficiently isolate humans and the environment over very long periods, and that final disposal does not impose an excessive technical, financial or social burden on the future generations. For example “It is generally accepted that the generation that benefited from the nuclear technology should also support the burden without transferring it to the future generations” (ONDRAF, 2001).

The basic idea behind geological disposal is to select an area with a stable geological situation for sitting of the repository so as to isolate the nuclear wastes in this using both engineered and natural barriers (NUMO, 2002a). The deep underground environment has preserved ore deposits and fossils for millions of years. This is possible in environments where the movement of deep groundwater is very slow, and the environment is chemically stable. It is common to find deep rock formations that have not changed perceptibly since they were formed, many millions of years ago. The Uranium ore of Cigar Lake, Canada is considered an example of a natural analogue that has been isolated for over 1,300 million years since its formation. Despite the high grade Uranium ore 430 meters underground, there are no signs on the surface of its presence.

The rate of deep groundwater movement can be determined from the age of deep groundwater calculated from concentrations of natural isotopes. In many locations, water may be tens of thousands to millions of years old. The stable chemical conditions result from the interaction of only small volumes of water with large volumes of rock over very long times without major disturbance (NUMO, 2002b).

The long-term performance of an underground repository for radioactive waste is largely determined by transport properties of radionuclides released occasionally through the engineered barriers into the surrounding geological formation (Mell et al., 2005). Migration of contaminants from the disposal site to the far field mainly depends on the physical condition of the porous media and interaction of the rock mass with the aqueous phase containing contaminants (Golubev and Garibyants, 1971). Mechanisms which control the contaminant migration through the rock mass are advection, dispersion, diffusion and/or retardation (IAEA, 1994). In low permeability geological formations, solute transport through fluid-filled fractures is likely to be very rapid compared to that in the solid rock where molecular diffusion is probably the major mass transport process within the discontinuous pores in the rock (Peck, 1967).

In the present study we investigate the potential movement of contaminants from a deep underground repository under conditions of advection and diffusion. The unfractured, intact host bedrock is considered a low permeability and low porosity domain where groundwater movement is negligible. The transport of the natural isotopes of water (^{18}O and ^{2}H) is simulated over the Pleistocene epoch.

1.1.1 Objectives

The goals of the present study are to:

(1) Study and model the effects of Pleistocene glacial loading and unloading cycles on groundwater systems in the Michigan Basin and the anomalous hydraulic heads that have developed. Use coupled stress and porewater pressure numerical analysis to assess the effects of the hydro-mechanical loading including different glacial loading scenarios, number of loading cycles, wet/dry glacial-soil interface, glacial advance direction and the effect of the Cambrian aquifer on the development of anomalous pressure heads.

(2) Study and model natural tracer profiles from three different sites in order to evaluate the upscaling process and estimate the veracity of using a single diffusion coefficient over the time scales relevant for the migration of radioactive contaminants. The study sites are Benken (Switzerland), Tournemere (France) and Bruce (Canada). This includes development of accurate large-scale models based on paleogeological characteristics, and the use of accurate numerical models to simulate measured profiles of isotope concentrations. The effect of density dependant convection, heterogeneity, and advection due to the effects of the glaciations are also considered.

(3) Develop an analytical solution for diffusion limited solute transport in three dimensions. This solution can be used to simulate concentrations in homogenous rock formations, with different diffusion coefficients perpendicular and parallel to the bedding and using different boundary conditions which simulate various internal and external sources. The purpose of the analytical model is as a screening tool for the investigation of diffusion and retardation effects and for assisting in the discretization of numerical models that are limited to finite domains.

1.2 Literature Review

In the following section, we review the literature on diffusion processes, natural isotopes, and numerical modeling. The intent of this section is to provide the reader with the state of scientific understanding on these processes.

On a microscopic scale, rocks are pervaded by an intricate network of micro fractures and connected pores where advective water flow, which may carry radionuclides released from a repository for radioactive waste, is either absent or plays only a minor role. Solute transport occurs primarily through pores or micro-cracks by diffusion processes. The absence of large fractures in the host geological formations means the effect of matrix diffusion is negligible. The prevailing type of diffusion will depend on species molecular size and on the pore size distribution in the rock. The three primary modes of diffusion are:

- **Molecular (Fickian) Diffusion**

  Molecular diffusion occurs when the mean free path is relatively short compared to the pore size, and is described by Fick's law (Fick, 1855). The transport diffusivity relates the macroscopic flux of molecules in a system to a driving force in the concentration. This diffusion mode is applicable to Brownian motion, where the movement of each particle is random and not dependent on its previous motion.

- **Knudsen Diffusion**

  Knudsen diffusion occurs when the mean free path is relatively long compared to the pore size, so the molecules collide frequently with the pore wall. Knudsen diffusion is dominant for pores that range in diameter between 2 and 50 nm (Malek and Coppens, 2003).

- **Surface Diffusion**

  Surface diffusion is used to explain a type of pore diffusion in which solutes adsorb on the surface of the pore and hop from one site to another through interactions between the surface and molecules (Jaguste and Bhatia, 1995).

1.2.1 Pore-scale model

Diffusion in porous media is affected by molecular mechanisms at the macroscopic scale, and the influence of pore structure on the microscopic scale (Kozuskanich et al., 2007). To predict the values of pore water diffusion coefficients in macroscale models, a factor is multiplied by the free water diffusion coefficient to account for the bulk properties and heterogeneity of the porous material. This approach is widely employed through the use of the geometric factor (sometimes called the tortuosity factor) or parameters derived from Archie's law.

1.2.2 Effective diffusion coefficient

Several methods to estimate effective diffusion coefficients from free water diffusion have been provided in the literature. For example, the diffusion coefficient for spherical particles in a liquid, D_o, is related to temperature T, viscosity of the liquid μ, and the hydrodynamic radius of the particles r. The diffusion coefficient, D_o, was calculated by the Stokes–Einstein equation (Einstein, 1905):

$$D_o = \frac{KT}{6\pi\mu r} \tag{1.1}$$

where K is the Boltzman Constant.

The diffusivity of an aqueous species through the interconnected pore space, D_P, in a rock matrix is often assumed to be proportional to its diffusivity in bulk solution (D_o) and to the tortuosity of the rock (Shackelford, 1991).

$$D_P = \tau D_o \tag{1.2}$$

where τ is the tortuosity factor and is defined as the ratio of the path length the solute would follow in water alone, L, relative to the tortuous path length it would follow in porous media L_e (Bear, 1972) and its value is always < 1.

$$\tau = ({}^{L}/_{L_e})^2 \tag{1.3}$$

Jacob (2004) defined the geometric factor that relates pore geometry and diffusivity:

$$G = \frac{\delta_D}{\tau^2} \tag{1.4}$$

$$D_e = \theta_P G D_o \tag{1.5}$$

Where
$$F = \theta_P G \tag{1.6}$$

And where Constrictivity δ_D ($\delta_D < 1$) accounts for the changes in the cross section of individual pores, D_e is the effective diffusion coefficient of the tracer in the pore water (L^2T^{-1}) and F is the formation factor.

The total porosity of rocks is subdivided into (1) flow porosity, (2) diffusion accessible porosity θ_P, and (3) residual porosity. The flow porosity is the part of the void space which is affected by flowing groundwater (Jardine et al., 1999). The diffusion-accessible porosity is the part of the total porosity where solutes can only have access by pure diffusion, where the water is stagnant and where the effect of a hydraulic pressure gradient is negligible. These parts of the void space are very often dead-ended. The residual porosity is the non-accessible, isolated pore space (Jacob, 2004).

Parkhomenko (1967) used electrical conductivity to define an empirical relationship between the geometric and formation factors in terms of porosity for crystalline rocks as shown in equation (2.7). This is known as Archie's law. Archie's law is often used to empirically describe the electrical conductivity of porous rocks, as a function of fluid resistivity, and porosity (Archie, 1942).

$$F = 0.71\theta_P{}^{1.58} \text{ and } G = 0.71\theta_P{}^{0.58} \qquad (1.7)$$

Boving and Grathwohl (2001), using another analogue of Archie's law, proposed a relationship between effective diffusion and total porosity from diffusion experiments done on different samples of limestone and sandstone. They concluded that the dominating parameter of diffusion is the total porosity. They also defined the value of tortuosity in equation (1.2) to be equal to porosity to the power (1.2). This works for rock samples of porosities > 20%. However, Kong et al. (2002) showed that the pore size distribution is the primary parameter affection diffusion processes.

The relationship between hydraulic conductivity (K) and effective diffusion (D_e) was studied by Boving and Grathwohl, (2001). There is however limited theoretical support for these and thus uncertainty as to how the parameters might behave at temporal scales beyond what we can measure.

Samson et al. (1999) used transport and mass conservation equations at the microscopic scale to describe the movement of particles in the fluid phase of the saturated cement based materials under diffusion mechanism. These equations are then averaged over the entire volume of the material using homogenization technique. They concluded that this technique can describe the transport of ions at the material scale.

1.2.3 Modeling of natural tracers

Environmental tracers have become a common tool in groundwater study where numbers of methods have been developed in order to understand groundwater flow and transport processes (Kazahaya et al., 2007). One of these methods is the use of natural tracers, ^{18}O and ^{2}H for their stability in water and their inherent isotopic ratios that can be correlated with the recharge elevation, distance from the coast, or the local topography.

The very low fluid flow velocities in low conductivity media and time constraints generally preclude artificial tracers for evaluating mass transport. It is therefore necessary to consider the utility of natural tracers already present in the system. This may help to characterize water flow and solute transport (Patriarche et al., 2004). The Study of the concentration patterns allows for evaluating model concepts and material properties in relevant formations.

Transport properties of the host rock are usually assessed by determining diffusion coefficients and the permeability of rock samples at laboratory scale, or by hydraulic tests in boreholes. Then field experiments at larger scales are used to verify transport properties obtained at smaller scales. Up-scaling the experiments in time and space to the extent which are relevant to the case of disposal of radioactive waste are, however, impossible (Gimmi et al., 2007 and Savoye et al., 2008).

The main challenges of using natural tracers are not only to obtain both hydrogeological and geochemical boundary and initial conditions of the system that are valid over long time intervals; but also to estimate the transport processes and rock parameters properly (Patriarche et al., 2004 and Gimmi et al., 2007).

1.2.4 Numerical modeling:

Several numerical models were reviewed in order to select a suitable model for the present study. The selection criteria are based on a model with capabilities to simulate three dimensional flow and solute transports in low permeable heterogeneous medium. The model also should be capable of simulating diffusion dominant transport, density dependant flow and remnant overpressures from glaciations. The models 3DFEMFAT, SWIFT, FEFLOW, FEMWATER and HGS were reviewed for their suitability in terms of availability, cost, ease-of-use, applicability and capabilities. Table 1.1 is showing a comparison between the applications of different models (Deeds and Jones, 2011).

Table 1-1 Comparison between different numerical models applications (Deeds and Jones, 2011)

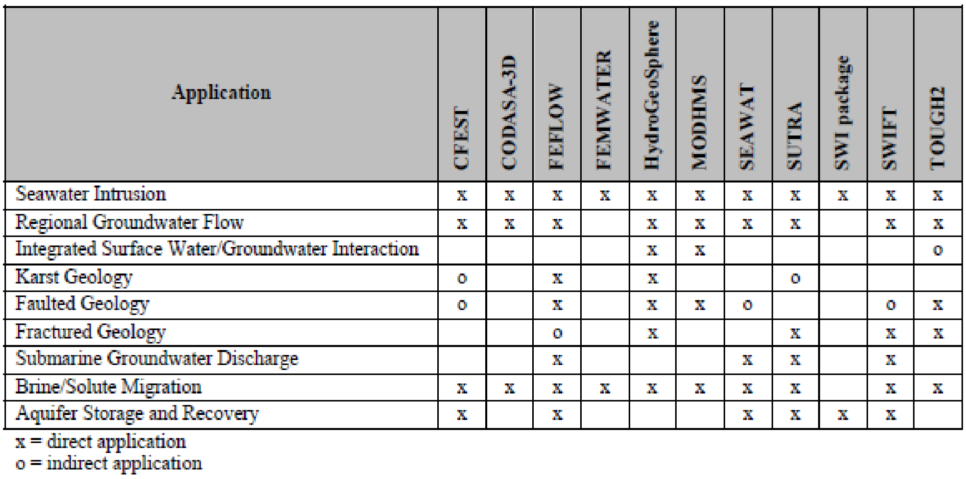

Application	CFEST	CODASA-3D	FEFLOW	FEMWATER	HydroGeoSphere	MODHMS	SEAWAT	SUTRA	SWI package	SWIFT	TOUGH2
Seawater Intrusion	x	x	x	x	x	x	x	x	x	x	x
Regional Groundwater Flow	x	x	x		x	x	x	x		x	x
Integrated Surface Water/Groundwater Interaction					x	x					o
Karst Geology	o		x		x			o			
Faulted Geology	o		x		x	x	o			o	x
Fractured Geology			o		x			x		x	x
Submarine Groundwater Discharge			x				x	x		x	
Brine/Solute Migration	x	x	x	x	x	x	x	x		x	x
Aquifer Storage and Recovery	x		x				x	x	x	x	

x = direct application
o = indirect application

The model selected for this study is *HydroGeoSphere* (HGS), which has wide capability for accommodating diffusion in complex settings. In particular, HGS has a robust formulation which well-simulates the free convective flows which occur as a result density gradients in saline systems. Remnant overpressures from glaciations can also be captured using this model (Therrien et al., 2008).

The hydrodynamic dispersion tensor D [L^2 T^{-1}] used in HGS is given by Bear, (1972), where the effective diffusion coefficient is the result of multiplying D_o by porosity and tortuosity:

$$\theta_s S_w D = (\alpha_l - \alpha_t)\frac{qq}{|q|} + \alpha_t |q| I + \theta_s S_w D_{free} \tau I \qquad (1.8)$$

where $\alpha_l$and α_t are the longitudinal and transverse dispersivities [L], respectively, $|q|$ is the magnitude of the Darcy flux, τ is the matrix tortuosity [dimensionless], D_{free} is the Free solution diffusion coefficient [L^2 T^{-1}] , and I is the identity tensor.

For grid discritization, Weatherill et al., (2007) examined the required spatial discretization in the fracture-matrix interface for numerical simulation of solute transport. The study compared numerical model (HGS) results with an analytical solution (Tang et al., 1981). The study showed that the degree of grid refinement and the rate in which the grid coarsens significantly affect numerical error and depend on whether the transport occurs due to advection/dispersion or diffusion. The study of grid discritization for a pollutant volume source, i.e. repository, in a low permeable domain needs to be studied.

Different concentrations of the transported species directly affect the fluid density, thus producing a flow pattern under gravity forces. This phenomenon is called density driven flow, or buoyancy induced flow (Frolkovic, 2000). Even for relatively low density contrasts, the effects of density driven flow are usually not negligible (Johannsen et al., 2002). This phenomenon of density driven flow can be modeled by a system of two nonlinear coupled partial differential equations (Johannsen et al., 2002).

The Darcy equation describing density-dependant subsurface flow used in HydroGeoSphere is given by Frind (1982):

$$q_i = -K_{ij}\frac{\mu_o}{\mu}(\frac{\partial h^*}{\partial X} + \rho_r\frac{\partial Z}{\partial X}) \qquad (1.9)$$

Where q_i is the Darcy flux, K_{ij} is the hydraulic conductivity tensor, μ_o is the reference viscosity, μ is the actual fluid viscosity as a function of the fluid temperature and fluid composition, h^* is the equivalent freshwater head defined by Frind (1982) as:

$$h^* = \frac{\rho}{\rho_o g} + Z \qquad (1.10)$$

Where ρ_o is the reference density or density of freshwater, p is fluid pressure, g is gravitational acceleration, Z is elevation above the datum and ρ_r is the relative density given by:

$$\rho_r = \frac{\rho}{\rho_o} - 1 \qquad (1.11)$$

1.3 References

Archie, G.E., (1942), The electrical resistivity log as an aid in determining some reservoir characteristics, Trans. AIME 146, 54–62.

Bear, J. (1972), Dynamics of fluids in porous media, American Elsevier Publishing, New York.

Boving, T. B. , and Grathwohl, P. (2001), Tracer diffusion coefficients in sedimentary rocks: correlation to porosity and hydraulic conductivity, Journal of Contaminant Hydrology 53,85–100.

Deeds, N.E. and Jones, T.L. (2011). Assessment of Groundwater Modeling Approaches for Brackish Aquifers. Final Report.

Einstein, A. (1905), On the movement of small particles suspended in a stationary liquid demanded by the molecular kinetics of heat. Ann. Phys. 17:549–560.

ENRESA (2006), Sixth General Radioactive Waste Plan [6th GRWP], The Spanish radioactive waste management agency, June 2006.

Fick, A. (1855), V. On liquid diffusion, Philosophical Magazine Series 4, 10: 63, 30 — 39.

Frind, E.O. (1982), Simulation of long-term transient density-dependant transport in groundwater, Advances in water Resources, 5(2), 73-88.

Frolkovic, P., and Schepper, H. (2000), Numerical modelling of convection dominated transport coupled with density driven Flow in porous media, Advances in Water Resources 24, 63±72.

Gimmi, T., Waber, H.N., Gautschi A., and A. Rubel (2007), Stable water isotopes in pore water of Jurassic argillaceous rocks as tracers for solute transport over large spatial and temporal scales, Water Resour. Res., 43, W04410, doi:10.1029/2005WR004774.

Golubev, V.S., and Garibyants, A.A. (1971), Heterogeneous Processes of Geochemical Migration, Consultants Bureau, New York-London, p. 150.

IAEA (1994), Classification of radioactive waste, International Atomic Energy Agency, Vienna, SAFETY SERIES No. 111-G-1.1-1994.

Jaguste, D.N. and S.K. Bhatia, Combined Surface and Viscous-Flow of Condensable Vapor in Porous-Media. Chemical Engineering Science, 1995. 50(2): p. 167-182.

Jakob, A. (2004), Matrix diffusion for performance assessment - experimental evidence, modeling assumptions and open issues. Report - IISN 1019-0643, Nucleur Energy and Safety Research Department Laboratory for Waste Management, Paul Scherrer Institut (PSI), Villigen PSI, Switzerland.

Jardine, P. M., Sanford, W. E., Gwo, J. P., Reedy, O. C., Hicks, D. S., Riggs, J. S., and Bailey, W. B. (1999). Quantifying diffusive mass transfer in fractured shale bedrock, Water Resour. Res., 35(7), 2015– 2030.

Johannsen, K., Kinzelbach W., Oswald S., and Wittum G. (2002), The saltpool benchmark problem – numerical simulation of saltwater upconing in a porous medium, Advances in Water Resources 25, 335–348.

Kazahaya, K., Yasuhara, M., Takahashi, H.A., Morikawa, N., Ohwada, M., Tosaki, Y. and Kazuyoshi ASAI (2007), Groundwater studies using isotopes and noble gases as a tracer: Review and prospect, JAHS, 37(4), 221

Kong, C.S., Kim, D.Y., Lee H.K., Shul, Y.G. and Lee, T.H (2002). Influence of pore-size distribution of diffusion layer on mass-transport problems of proton exchange membrane fuel cellsJournal of Power Sources. 108 (1-2), pp. 185-191.

Kozuskanich, J., Kumar G.S., and Novakowski K. (2007), Theory and literature review of diffusive mass transport at the molecular level in a microcrack network, NWMO TR.

Malek, K. and M.O. Coppens (2003), Knudsen self- and Fickian diffusion in rough nanoporous media. Journal of Chemical Physics. 119(5): p. 2801-2811.

Mell P., J. M., Riess L., Máthé Z., Hámos G., and Lázár K. (2006), Diffusion of Sr, Cs, Co and I in argillaceous rock as studied by radiotracers, Journal of Radioanalytical and Nuclear Chemistry, Vol. 268, No.2 (2006) 411–417.

NUMO (2002a), Repository Concepts, Nuclear Waste Management Organization of Japan, URL: http://www.numo.or.jp.

NUMO (2002b), Open Solicitation for Candidate Sites for Safe Disposal of High-Level Radioactive Waste, Nuclear Waste Management Organization of Japan, URL: http://www.numo.or.jp.

ONDRAF (2001), Towards a sustainable management of radioactive waste, the Belgian National Agency for Radioactive Waste and enriched Fissile Material, Belgian agency for radioactive waste and enriched fissile materials, NIROND 2001-07E.

Patriarche, D., Ledoux, E., Michelot, J.L., Simon-Coinc¸ R. and Savoye, S. (2004), Diffusion as the main process for mass transport in very low water content argillites: 2. Fluid flow and mass transport modeling,Water Resour. Res., 40,W01517, doi:10.1029/2003WR002700.

Peck, A.J. (1967), Mass Transport in Porous Rocks, Mineralium Deposita 2, 243—247.

Samson, E., Marchand, J. and Beaudoin, J.J. (1999), Describing ion diffusion mechanisms in cement-based materials using the homogenization technique, Cement and Concrete Research 29, 1341–1345.

Savoye, S., Michelot, J.L., Bensenouci, F., Matray, J.M., and Cabrera, J. (2008), Transfers through argillaceous rocks over large space and time scales: Insights given by water stable isotopes, Physics and Chemistry of the Earth 33, S67–S74.

Schackelford, C.D. (1991), Laboratory diffusion testing for waste disposal - review, Journal of Contaminant Hydrology, 7, 177-217.

Tang, D.H., Frind, E.O., and Sudicky, E.A. (1981). Contaminant transport in fractured porous media: analytical solution for a single fracture. Water Resources Res., Vol. 17(3), pp. 467–480.

Therrien, R., McLaren, R.G., Sudicky, E.A., and Panday, S.M. (2008), HydroGeoSphere A Three-dimensional Numerical Model Describing Fully-integrated Subsurface and Surface Flow and Solute Transport. Software Manual.

Weatherill, D., Graf, T., Simmons, C.T., Cook, P.G., Therrien, R., and Reynolds, D.A. (2007), Discretizing the Fracture-Matrix Interface to Simulate Solute Transport, Vol. 46, No. 4, GROUND WATER, (pages 606–615).

THIS PAGE HAS BEEN LEFT BLANK INTENTIONALLY

2 Impacts of Pleistocene Glacial Loading on Abnormal Porewater Pressure in the Eastern Michigan Basin

Abstract

The hydro-mechanical effects of the Pleistocene glacial loading cycles on the Michigan sedimentary basin is assessed using coupled stress and porewater pressure numerical analysis. The effects of several factors were considered in the analysis of different glacial loading scenarios including i) the number of loading cycles, ii) the effect of a wet/dry glacial-soil interface, iii) the direction of glacial advance, and iv) the effect of the deep Cambrian aquifer on the development of anomalous pressure heads. The analyses are intended to show the change in total head with time in the formations of the Michigan basin and underlying basement rock under different loading scenarios. The results show high porewater pressure developed within the formations during loading periods especially in low permeability units. In addition, the results show that the formations have not reached hydrostatic conditions at the present time due to the effect of the last loading cycle that ended around 12000 yrs. ago. Our results also illustrate the difference between applying mechanical loads on the land surface and applying an equivalent hydraulic head in the generated total heads in the rock formations. Furthermore, the overpressure in the Cambrian aquifer was generated by topographic head at the Cambrian formations outcrop. The results for present day define regions of underpressure in the upper Ordovician and lower Silurian formations characterized by very low hydraulic conductivity and adjacent to the Cambrian aquifer. The results were verified against measured environmental heads from the Bruce Deep Geological Disposal Repository site. This study presents a tool to evaluate the effects of future glacial events on long term performance of deep nuclear waste repositories.

Key words: Michigan basin, hyrdromechanical, modeling, glacial cycles.

2.1 Introduction

Abnormal fluid pressures occurs in low permeability formations where the ability to gain or drain water is less than changes that have occurred in fluid or pore volumes. The causes of this phenomenon might be physical, chemical or both (Chilingar et al., 2002) and they are unique for every sedimentary basin (Matusevich et al., 1997). Defining the causes of abnormal pressure and its progress with time is important in defining groundwater movement and solute transport over a long time scale especially for nuclear waste disposal. Abnormal fluid pressures have been observed in the eastern side of the Michigan basin, where six deep boreholes were drilled to the Precambrian. Multi-level monitoring systems were installed in these boreholes to observe pressure heads in the rock formations and to obtain groundwater samples (Jensen et al., 2009). Similar fluid pressure patterns have been observed in other sedimentary basins in North America and Europe (Neuzil, 1993; Corbet & Bethke, 1992; Michael & Bachu, 2011; Vinard, Bobet, & Einstein, 2001) under the mechanical unloading of erosion and/or glacial unloading. However, glacial loading and unloading are considerably faster processes than sedimentation and erosion (Bense & Person, 2008).

The hydromechanical loading forces exerted by ice sheets on earth crust caused large surface depression, where maximum crustal depressions excess of 500 m at Last Glacial Maximum (LGM) from equibrium level (Peltier, 2011). The dramatic over-pressurization of pore water fluids caused by surface loading influenced the dynamics of groundwater flow systems in the underlying sedimentary basins (Lemieux et al., 2008).

In this study, numerical modeling of the Michigan basin is used to provide insight into the impacts of Pleistocene glaciation on the development of anomalous pressure heads in the stratigraphic sequence. Specifically, we tested the hypotheses that: (i) Under-pressure can be related to surface rebound due to glacial unloading; (ii) The Cambrian Aquifer should not be considered as a no-flow lower boundary for flow ; and (iii) Groundwater flow occurs through the Cambrian aquifer from and to deeper parts of the Michigan basin. Moreover, the model provides a tool to calculate pore-water pressure under any hydromechanical loading conditions that might be hypothesized. This can be used to help unravel the glacial loading scenarios that have been developed using models for glacial advance. This modeling approach can also be helpful for solute transport modeling of potential nuclear waste repository sites.

2.2 Hydrogeology of Michigan basin

The Michigan Basin (Figure 2.1) is a nearly-circular, deep intracratonic basin with minor structural disruption, where the diameter and depth are approximately 700 km and 5 km respectively (Howell et al., 1999). The basin characteristics are well known through hydrocarbon explorations. The basement of the Michigan basin is the Precambrian crystalline rocks that vary in age from 2690 to 990 Ma and were deformed and metamorphosed during the Grenville Orogeny (Percival et al., 2007). The Precambrian underlies the Paleozoic sedimentary rocks, which are divided into a total of approximately 27 formations in the eastern Michigan Basin, ranging from the Cambrian sandstones at the bottom to the Devonian dolostones at the top (Sykes et al., 2011) A summary of the main formations identified at the Bruce Site (Raven et al., 2011), shown in table 2.1.

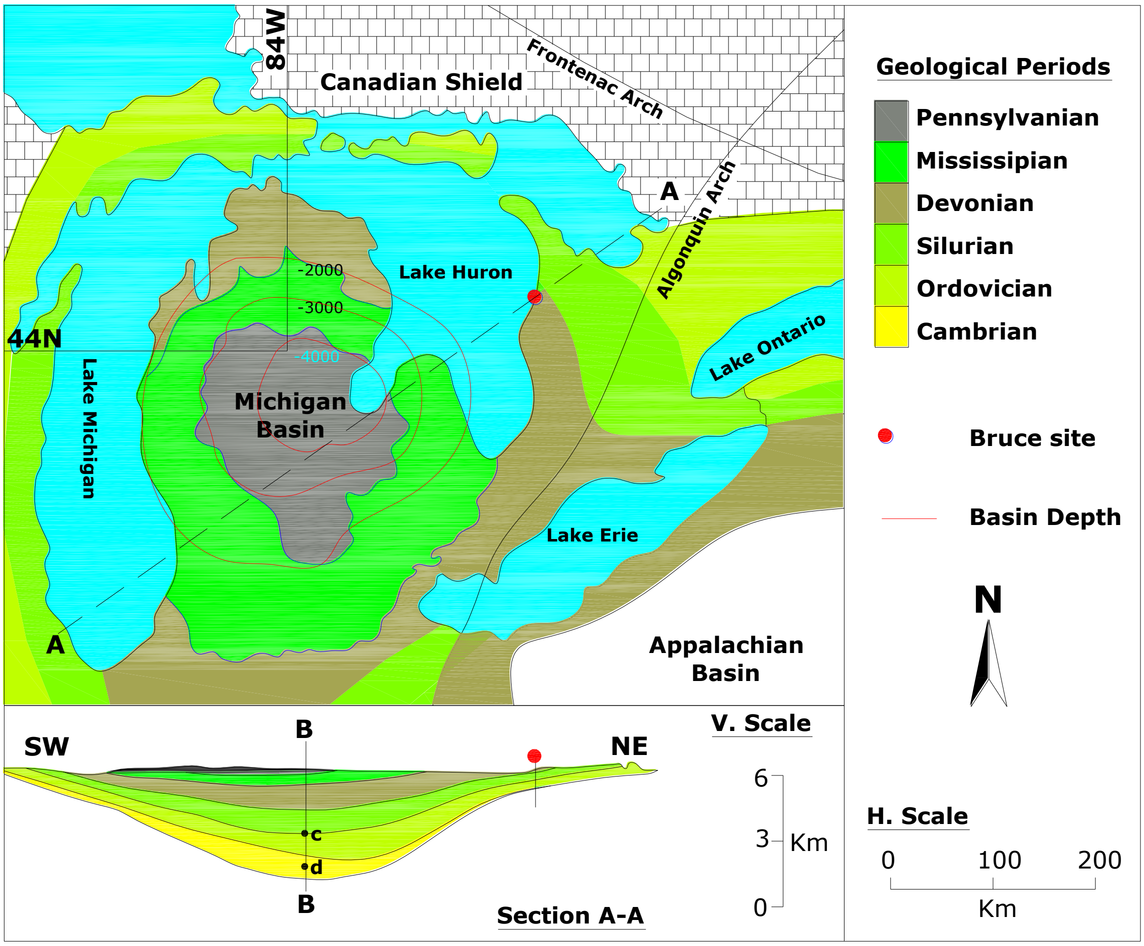

Figure 2.1: Bedrock geology map, and cross-sectional view of the Michigan basin [section A-A], adapted from Frizzell et al. (2008), Vertical line B-B and pointes c and d will be used to show the generated Total Head later.

Armstrong and Carter (2006) summarized the Paleozoic rocks for southern Ontario. The Cambrian units consist of quartzose sandstones with dolomitic quartz sandstones and sandy dolostones with higher permeability than adjacent layers. The Ordovician rocks overlay the Cambrian rocks or directly overlay the Precambrian basement rocks towards the Algonquin Arch (eastern margin of Michigan basin) and are divided into several groups. The lower group is composed of argillaceous sandstones/dolostones, overlain with fine grained limestone that includes the Cobourg formation. The upper group consists of non-calcareous shale with minor limestone. The Silurian rocks, overlay the Ordovician, consist of layers of dolostones/limestones, argillaceous dolostones/limestones. The top Devonian rocks consist of layers of dolostones/limestones.

Underpressures were observed in the Ordovician shale and limestone units (at depths of 450-750 mBGS) while overpressures were observed in the Black River limestone (depth of 400 mBGS)and the Cambrian sandstone (at depths of 800-860 mBGS) (Al et al., 2011) as shown in Figure 2.2.

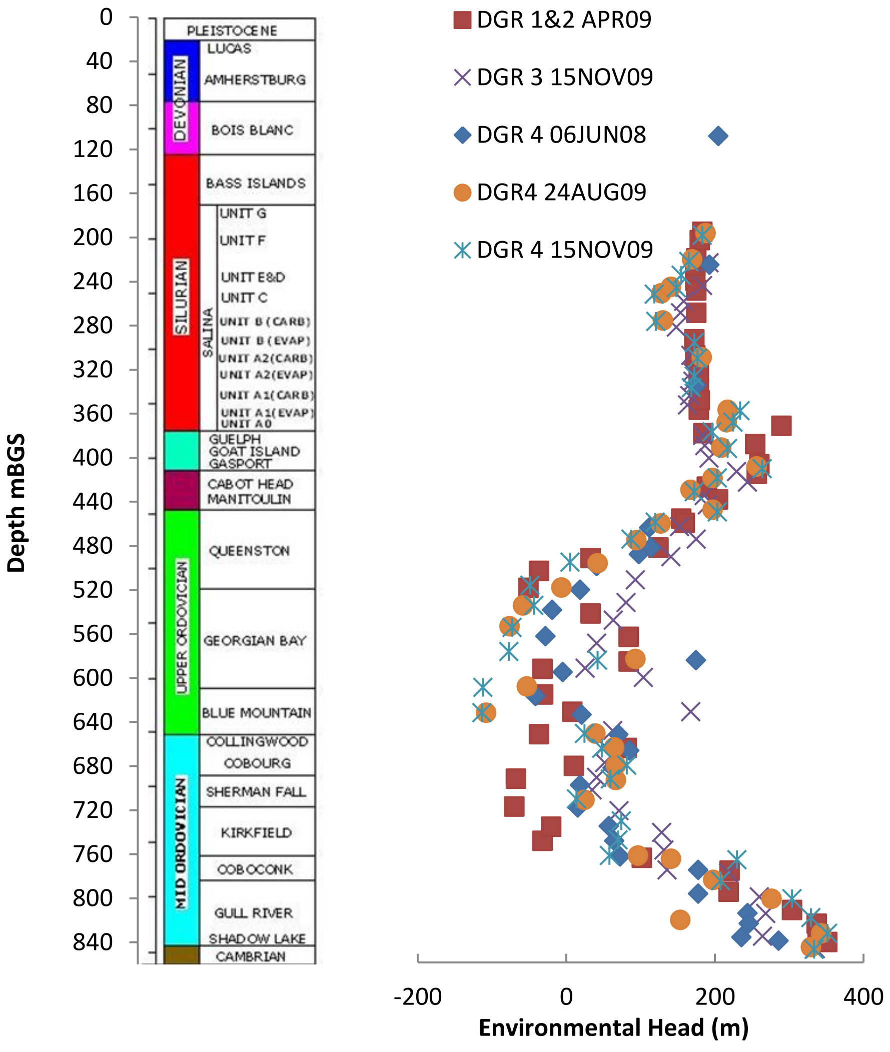

Figure 2.2: Measured Environmental Head (m) with Depth (m), Measurements was taken at the Bruce site as shown in Figure 2.1. Measurements are at different times in 2008 and 2009 and at different boreholes DGR1&2, DGR3 and DGR4 (Al et al., 2011).

2.3 Glacial history

Pleistocene glaciations have occurred over cyclic periods of about 100 ka as a result of climatic variations (Imbrie et al., 1993). These climatic variations are the result of changes in the geometry of Earth's orbit around the Sun, which causes small changes in the Sun effective intensity (Hays et al., 1976). These cycles most likely took place in the last 2.6 Ma with a minimum of 20 cyclic periods, where the most extensive occurred in the last 0.9 Ma (Ehlers and Gibbard, 2007). During these periods ice sheets grew covering North America up to the current USA-Canada border and some portions of the northern United States. Concentration of ^{18}O in ocean drilling shows that glacial recharge in Mississippi river from northern hemisphere started 2.3 Ma (Joyce et al., 1993). Balco and Rovey (2010) states the first recorded advance of laurentide ice in central north America started 2.4 Ma. The Michigan Basin was entirely overrun by ice sheets, and ice thickness exceeded 2.5 km over Southern Ontario during the last glacial maximum (LGM) (Peltier, 2011). Ice sheet thickness, permafrost and generated melt water for the eastern Michigan basin were simulated using the Glacial Systems Model (GSM) developed by (Peltier, 2011).

2.4 Previous modeling efforts in the Michigan basin

There are several previous studies which have been conducted to explain the under/over pressure and explore the groundwater flow systems in sedimentary basins. Nasir et al., (2011) developed one- and two-dimensional hydro-mechanical models for the Michigan basin. Past glacial cycles generated by Peltier (2011) were applied on land surfaces for different scenarios. They concluded that glacial loads had a significant impact on the pore water pressure gradient and effective stress distribution within the sedimentary rocks of southern Ontario. The model results however did not capture all the features of the measured head profiles, in particular the underpressuring was approximated poorly. The section they introduced for the 2-D model was at the edge of the basin and did not include an outcrop for the Cambrian aquifer.

Table 2-1 Hydrogeological properties of Michigan Basin formations used in the numerical model

Geologic Age	Formation	n	K_h m/s	K_v m/s	E GPa	Poisson's Ratio
Quaternary	Drift*	0.25	1.6x10^{-7}	1.6 x10-8	10	0.2
Pennsylvanian	Saginaw	0.1	1.0 x10^{-5}	1.0 x10^{-8}	40	0.2
Mississippian	Michigan	0.1	1.0 x10^{-11}	1.0 x10^{-12}	18	0.2
	Marshall	0.1	5.0 x10^{-7}	5.0 x10^{-7}	18	0.2
	Coldwater	0.1	1.0 x10^{-9}	1.0 x10^{-10}	18	0.2
Devonian	Berea Bedford	0.1	1.0 x10^{-7}	1.0 x10^{-8}	7.7	0.18
	Kettle Point	0.1	3.0 x10^{-9}	3.0 x10^{-10}	7.7	0.18
	Hamilton Group	0.1	2.2 x10^{-11}	2.2 x10^{-12}	7.7	0.18
	Dundee	0.1	8.4 x10^{-8}	8.4 x10^{-9}	7.7	0.18
	Detroit River Group	0.077	5.9 x10^{-7}	5.9 x10^{-8}	7.7	0.18
	Bois Blanc	0.077	1.0 x10^{-7}	1.0 x10^{-8}	7.7	0.18
Silurian	Bass Islands	0.056	5.0 x10^{-5}	5.0 x10^{-6}	4.0	0.3
	F unit	0.1	5.0 x10^{-14}	5.0x10^{-15}	22.6	0.3
	Niagaran	0.026	3.6 x10^{-9}	2.5 x10^{-13}	37.0	0.3
	Cabot Head	0.116	9.0 x10^{-14}	9.0 x10^{-15}	13.8	0.3
	Manitolian	0.028	9.0 x10^{-14}	9.0 x10^{-15}	13.8	0.3
Ordovician	Queenston	0.073	2.0 x10^{-14}	2.0 x10^{-15}	13.8	0.3
	Georgian Bay	0.07	3.5 x10^{-14}	3.2 x10^{-15}	13.8	0.3
	Trenton Group	0.018	1.2 x10^{-14}	1.0 x10^{-15}	13.8	0.3
	Black River Group	0.023	6.5 x10^{-11}	9.9 x10^{-16}	13.8	0.3
	Ancell Group	0.02	3.5 x10^{-5}	3.5 x10^{-5}	13.8	0.3
	Prairie Du Chien Group	0.02	3.5 x10^{-5}	3.5 x10^{-5}	13.8	0.3
Cambrian	Trempealeau Fm	0.02	3.5 x10^{-10}	3.5 x10^{-11}	76.6	0.25
	Francania Fm	0.02	3.5 x10^{-10}	3.5 x10^{-11}	76.6	0.25
	Galesville Sandstone	0.071	3.0 x10^{-6}	3.0 x10^{-6}	76.6	0.25
	Eau Claire Fm	0.071	3.0 x10^{-6}	3.0 x10^{-6}	76.6	0.25
	Mount Saimon Fm	0.071	3.0 x10^{-6}	3.0 x10^{-6}	76.6	0.25
Precambrian	Basement*	0.01	3.2 x10^{-13}	3.2 x10^{-15}	76.6	0.25

Reproduced from [Sykes et al., (2011) and McIntosh et al.*, (2011)]

Lemieux et al., (2008) constructed a three-dimensional numerical model that includes Canada and most of northern United States to investigate the impacts of the impact of glacial advances and retreats during the Wisconsinian glaciation on groundwater flow and brine transport in the Paleozoic sedimentary basins. Coupled processes, such as groundwater flow and glaciation modeling, density dependent flow, hydromechanical loading, subglacial infiltration, isostasy, and permafrost were incorporated into the model. Model results show that infiltration of subglacial meltwater occurs during ice sheet progression and that groundwater mainly exfiltrates on the surface during ice sheet regression, in both the subglacial and periglacial environments. The coarse discretization of the model made it impossible to evaluate the impacts of glaciation on individual Michigan basin layers, as the Basin was represented as one hydrogeologic unit.

Sykes et al., (2011) developed a three-dimensional regional and site-scale hydrogeological model of the eastern margin of the Michigan Basin using FRAC3DVS-OPG, for the proposed (DGR) Bruce site intended for nuclear waste disposal. The impact of glacial loading and unloading on the groundwater system was investigated in several paleohydrogeologic scenarios. The paleohydrogeologic scenarios estimated that it is unlikely that either the under/over-pressures measured in the DGR boreholes are related to glacial un/loading.

Bense and Person, (2008) developed a two-dimensional numerical model for intracratonic sedimentary basins to assess the effects of mechanical ice sheet loading and unloading, permafrost formation and thawing, variable density fluids, and lithospheric flexure during glaciation on solute and isotope transport, groundwater residence times, and transient hydraulic head distributions. The simulations can be applied, in a generic sense, to intercratonic sedimentary basins such as the Williston, Michigan, and Illinois basins that would have been near the southern limit of the Laurentide Ice Sheet during the last glacial maximum. The model results show the development of complex fluid flow patterns that help to explain observations of both over/underpressures within sedimentary basins.

McIntosh et al., (2011) Constructed a transient two-dimensional finite-element model of the northern half of the Michigan basin using CPFLOW to simulate density dependant flow, heat and solute transport under both modern and Late Pleistocene hydrologic conditions. The model was used to test explanations for the low salinity formation waters observed at depth in Michigan basin. Model simulations showed that high water head due to glaciation reorganized the salinity gradients in rock formations at depth despite the presence of dense brines while modern groundwater was restricted to shallow glacial drift aquifers. The model has no surface mechanical loading component, so for glacial loads, the hydraulic head was compensated for ice loads and added to the modern land surface elevation. No significant underpressurring in the low-permeability formations were observed in the simulations.

The previous models by [Lemieux et al., (2008), Sykes et al., (2011) and Bense and Person, (2008)] use the same governing equation for vertical surface loading that is aerially homogeneous so lateral strains will be neglected. The governing equation was modified by (Neuzil, 2003), where one-dimensional loading efficiency defines the ratio of change in fluid pressure to change in mean total stress under undrained conditions.

2.5 Methods

The previous models were compared with SIGMA/W model for the condition of the presence of lower boundary seepage face see (Appendix I). In this study we used a commercially available software product SIGMA/W (Geo-Slope International, 2007). The model is capable of performing coupled analysis under external loads, where equations for stress-deformation and seepage dissipation are solved simultaneously.

2.5.1 Model geometry

A 2-D numerical finite element model was built for the Michigan basin using SIGMA/W. The cross section of the Michigan basin modeled starting from the south west towards the north east was modified from (Frizzell et al. 2008) as shown in (Figure 2.1).

The finite element mesh for the basin includes 21861 nodes and 24470 elements with dimensions of 1x1 km or smaller to fit layers thickness as small as 20 m (Figure 2.3). Linear time step intervals were used of 40 years. The grid size and time step were chosen to minimize numerical errors, and were defined by performing several preliminary model runs. The values for different parameters of each layer including values of specific storage, compressibility, poisson’s ratio, permeability and porosity were compiled from NWMO, (2011) and McIntosh et al., (2011) and reported in table 2.1. The Values of hydraulic conductivity range between 1×10^{-5} m/s to 1×10^{-14} m/s. The basin consists mainly of low permeability formations separated by permeable layers.

The material properties for the models layers were set for purely linear elastic conditions so the response of the aquifer compressibility will be the same during ice advance or retreat. The domain was assumed to be fully saturated with water as any possible gas phase would affect the porewater pressure and increase the effective stresses on the rock structure.

Adding the weight of the layers to a coupled stress and pore water pressure analysis generates high porewater pressures. This pressure will not totally dissipate even when running the model for long time prior to applying glacial loading. That contradicts the sedimentation processes that would occur naturally in these layers. This sedimentation occurs gradually over a long time period and that in nature allows for pressure dissipation. To overcome this, in-situ analysis was first run with the rock weight, to establish the initial in situ stress conditions using the submerged weight of the rock prior to application of the glacial loading. The initial water pressure was obtained from the specified initial water table assigned at ground surface.

In general, the ice sheet advanced from north to south across the basin. The Direction of snow advance is from the north east as suggested by Peltier (2011) or North West (Piotrowski, 1987). Two different loading scenarios were assumed for the modeling, where the glacial loading advance direction was parallel or perpendicular to the direction of the 2-D section of the model.

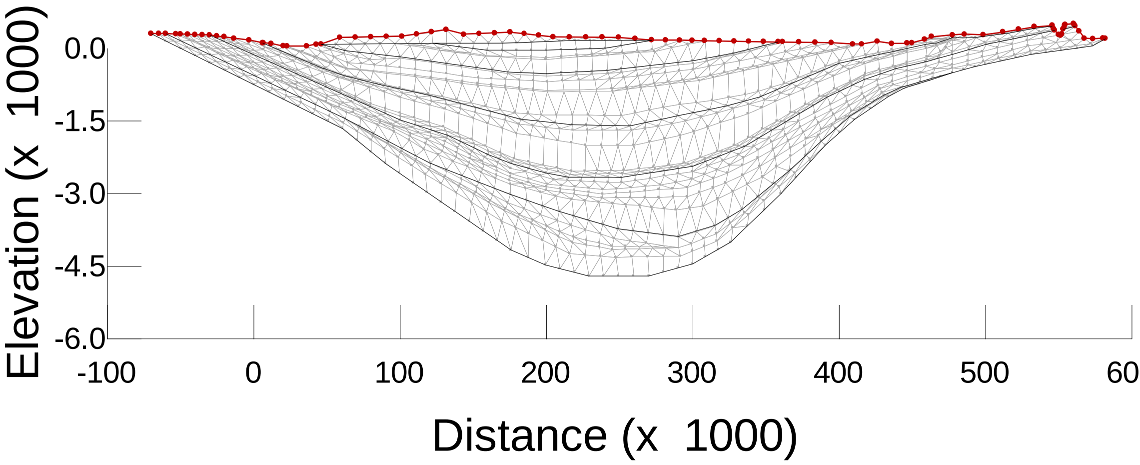

Figure 2.3: Two dimensional mesh of the Michigan Basin excludes the Precambrian. For legibility, The mesh is coarser than used in the simulations by one order of magnitude from 1 to 10 Km , distance and elevations in (m).

2.5.2 Glaciation Scenarios

Two scenarios for the Late Pleistocene Laurentide Ice are used as the hydro-mechanical loads in the SIGMA/W model. These glacial events are developed by the University of Toronto Glacial Systems Model (UofT GSM) (Peltier, 2011). The two scenarios (model runs nn9921 and nn9930) began approximately 120,000 years ago as shown in Figure 2.4. The Ice sheets developed in the Arctic regions and advanced to cover the Michigan basin, with a thickness that reached 2.8 km during the last glacial maximum (LGM) (Peltier, 2011). The values at the Bruce site are shown in Figure 2.4, and the glacial heights at other locations are interpreted from Peltier (2011). Approximately nine episodes of complete glacial cycles have occurred during the last million years over the North American continent. (Peltier, 2002).

2.5.3 Boundary conditions

Initial water pressure was set to hydrostatic conditions. The model was then run until steady state conditions under topography-driven flow are achieved. Boundary conditions then are set to the values described below.

The north east and south west sides of the model correspond to hydrologic divides and were set as no flow boundaries. The lower boundary was set also as a no flow boundary and the thickness of the Precambrian was increased to around 10Km below the Cambrian layer to eliminate the effects of lower boundary on the model results. The water table was set equal to the land surface. Wet-based ice sheet conditions were assumed where direct hydraulic connection existed directly between the glacier layer and land surface. Hydraulic head was set on the top boundary equal to the glacial height multiplied by a factor ranging between (0.3-0.8). Dry-based cases were also used in some scenarios.

For the stress/strain component of the model, the north east and south west sides of the model domain are fixed from moving in the horizontal direction and allowed to move in vertical direction. The lower boundary is fixed from moving in both horizontal and vertical directions, and the upper boundary is free in both directions. Glacial loadings are applied on the upper boundary with time. The ice thicknesses are given by Peltier (2011), where two of the developed loading scenarios were used (nn9921 and nn9930) as shown in Figure 2.4. The number of glacial cycles applied varies between model runs from one to ten cycles. The glacial loading also varies with distance in the case of glacial advance perpendicular to the 2-D model domain, where the glacial loads decrease towards the south.

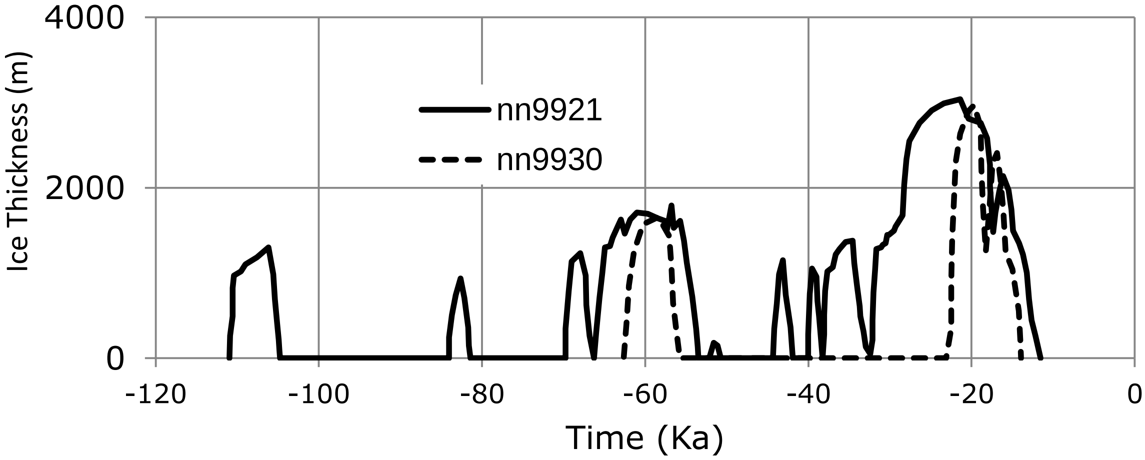

Figure 2.4: Ice loading scenarios at the Bruce site interpolated by the University of Toronto Glacial Systems Model (UofT GSM), Peltier (2011). Model runs nn9921 and nn9930 are shown.

As previously suggested, we considered six sets of model scenarios using the fully coupled stress and pore water pressure model (table 2.2). In the base case scenario, the model was loaded for one glacial cycle. The domain was assumed fully saturated with constant fluid density and a wet base case was assumed for the rock-glacier interface. The glacial advance was assumed from a north western direction which is perpendicular to the cross section. The model was used to test the effects of these glacial loads on the development of anomalous pressure heads that can exist until the present time. The number of glacial cycles was increased from 1 to 10 in the second scenario. All other factors remain unchanged from the first scenario. The purpose was to find whether the anomalous pressures will increase with more cycles or whether maximum values are reached quickly. The Cambrian layer outcrop from the south western edge of the model was removed in the third scenario. The importance of the Cambrian layer as a lower boundary for the Michigan basin and its effects on developing underpressure was tested in this case. In the fourth scenario, the direction of glacial advance was changed from the North West to the north east.

In the fifth scenario, the mechanical loads and the hydraulic heads resulted from glacial loads were isolated and tested alone. For the Mechanical loads, dry base case was assumed at the rock-glacial interface. For hydraulic head, mechanical loads were set to zero and water heads equivalent to the glacial loads were applied on the top boundary. In the last scenario, the elevation of the Cambrian formations at the SW end was raised to 400 m. The model is used to test the topographic effects on the overpressure measured in the Cambrian formations. The model was loaded by one glacial cycle. The rest of factors remain unchanged from the first scenario.

Table 2-2 Summary of the model scenarios

	Base Case	**Multiple Cycles**	**Cambrian Extend**	**Advance Direction**	**Mechanical Load**	**Equivalent Head**	**Topographic effect**
Loading Case	nn9930& nn9921	nn9921	nn9921	nn9921	nn9921	nn9921	nn9930& nn9921
No. Loading cycles	1	10	1	1	1	1	1
Hydraulic Head	0.8 x ice thickness	0.8 x ice thickness	0.8 x ice thickness	0.8 x ice thickness	0.0 x ice thickness	$H = \frac{W_{Ice}}{\rho_{water}}$	0.8 x ice thickness
Advance Direction	NW	NW	NW	NE	NW	NW	NE

Where W_{Ice} is the ice weight, and ρ_{water} is the water density.

2.6 Results and Discussion

2.6.1 Base Case

Three snap shots of the total transient head distributed along the domain for the glacial loading cases nn9921 and nn9930 are shown in Figure 2.5 and Figure 2.6 respectively. The first point in time represents the peak loading point at the LGM. The second point is just after the end of the LGM and the third point is at the present time.

During the peak at the LGM, pore water pressure is raised in the entire domain. The amount of increase depends on how fast the domain will dissipate the pressure gained. The Cambrian formations, with a relatively higher hydraulic conductivity, are raised by 10% of the increase in low conductivity formations. Just after the LGM, underpressure is formed in the Precambrian, upper Ordovician and lower Silurian formations. Underpressures were formed in the middle Silurian formations toward the edges of the domain. The values of underpressure are greater toward the basin edges. The underpressures in the Cambrian formations dissipated in a short period as shown in Figure 2.7. The results at present time show that underpressures continue dissipating from underpressured formations. Thus, under hydromechanical loading and unloading, the response of the domain layers depends strongly on hydraulic conductivity.

2.6.2 Multiple cycles

The model was loaded for 10 cycles using the glacial load scenario nn9921. Other initial and boundary conditions remain unchanged. The results show an increase in the underpressure in the Precambrian and lower Silurian formations (Figure 2.8). A slight change in underpressure in the upper Ordovician is shown in Figure 2.9.

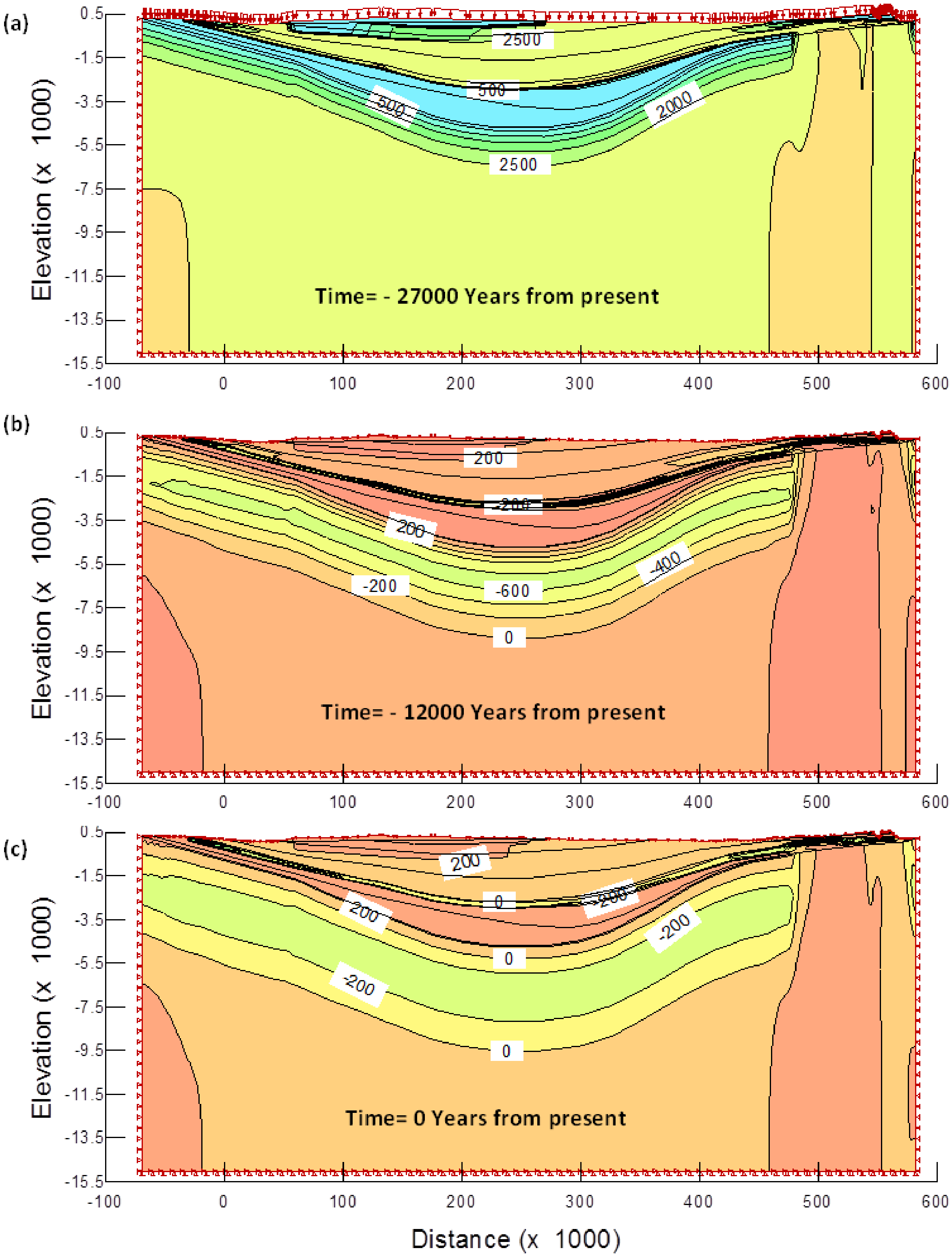

Figure 2.5: Total head at different times under loading scenario nn9921 for one loading cycle. Total heads are in m, and dimensions in m.

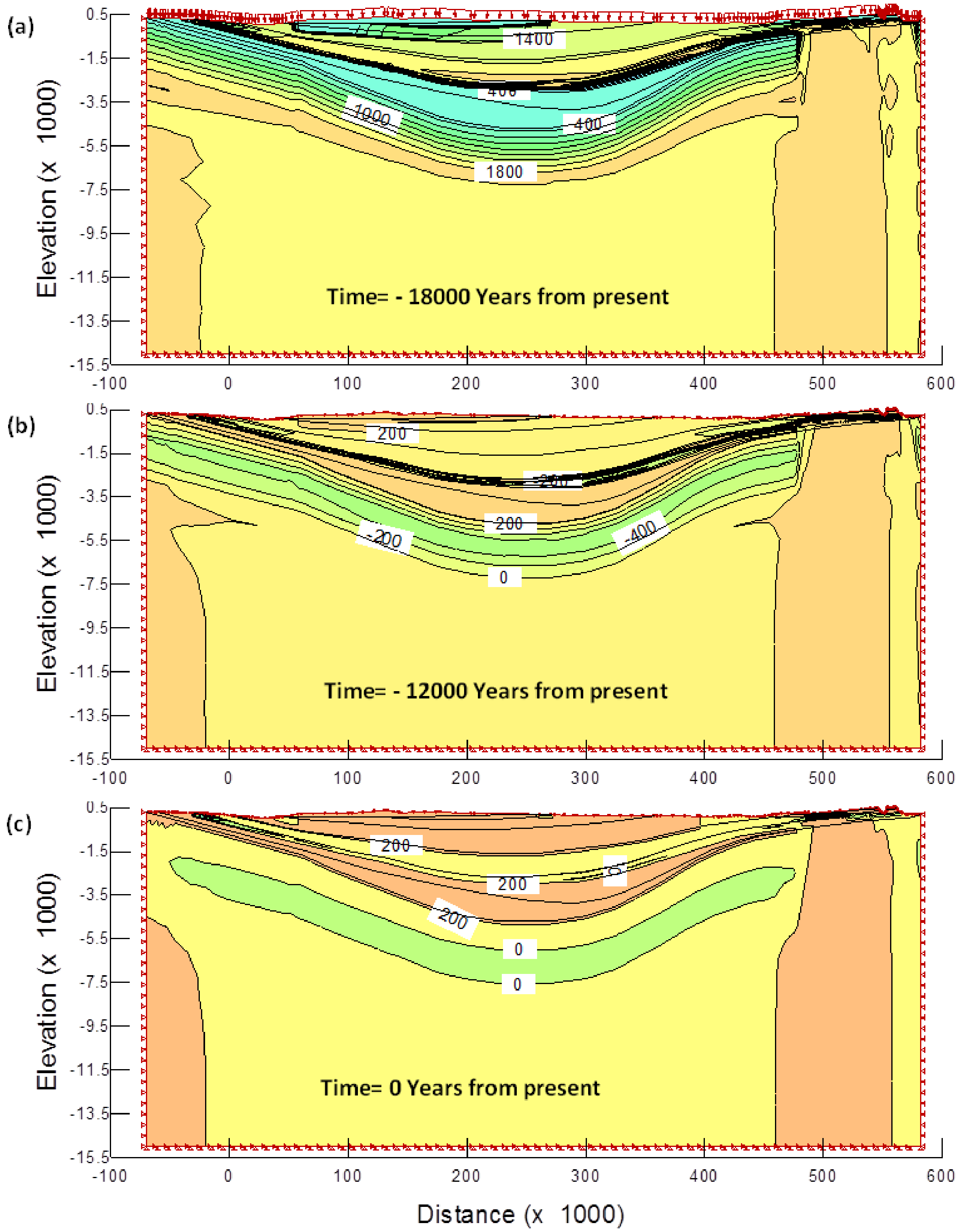

Figure 2.6: Total head at different times under loading scenario nn9930 for one loading cycle. Total heads are in meters, dimensions in (m).

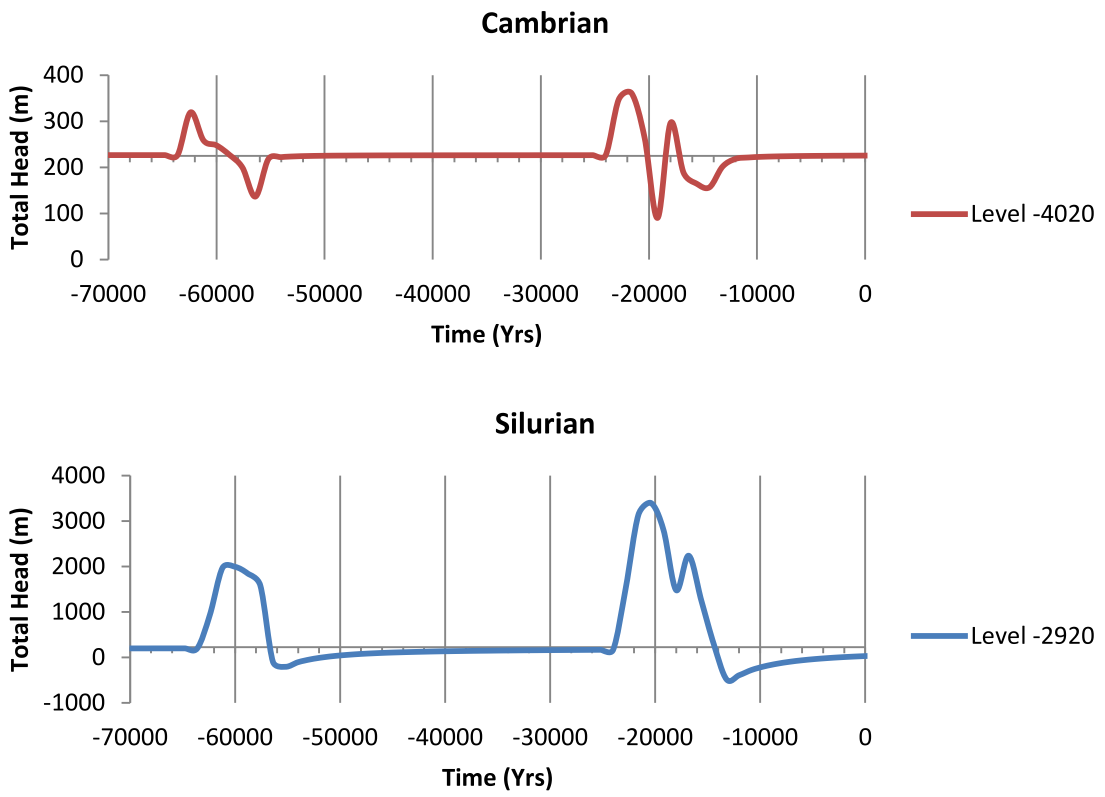

Figure 2.7: Total Head with time at the middle of Michigan basin under one loading cycle (nn9930). a) at the Cambrian aquifer at point (d) shown in figure (3.1) at a land level of -4020 m, b) at the Lower Silurian at point (c) shown in Figure 2.1 at a land level of -2920 m.

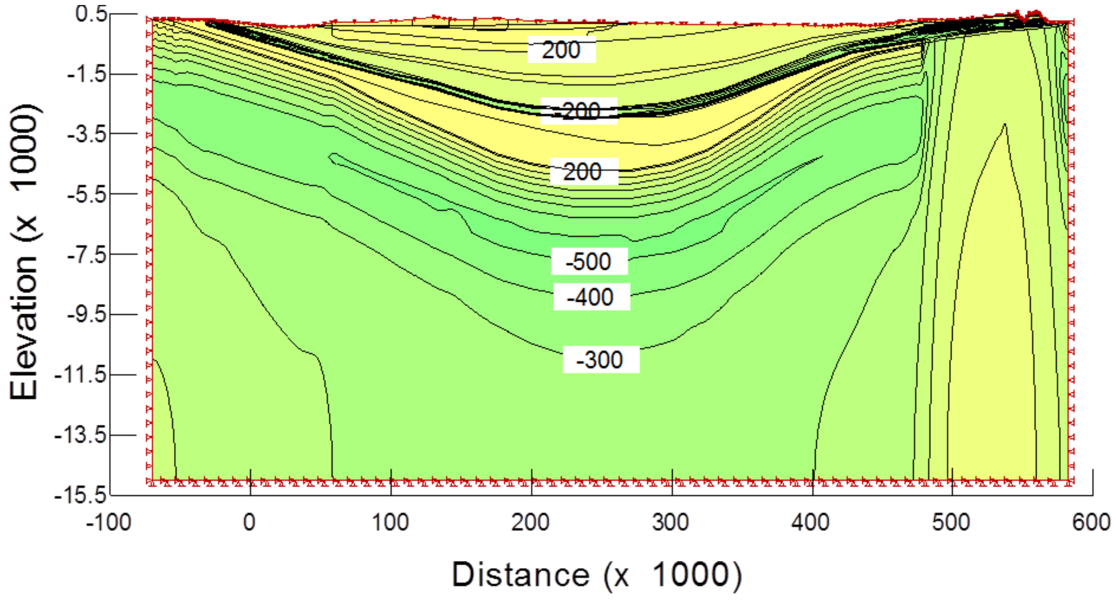

Figure 2.8: Total head at present under loading scenario nn9921 for 10 loading cycles. Total heads are in m, dimensions in m.

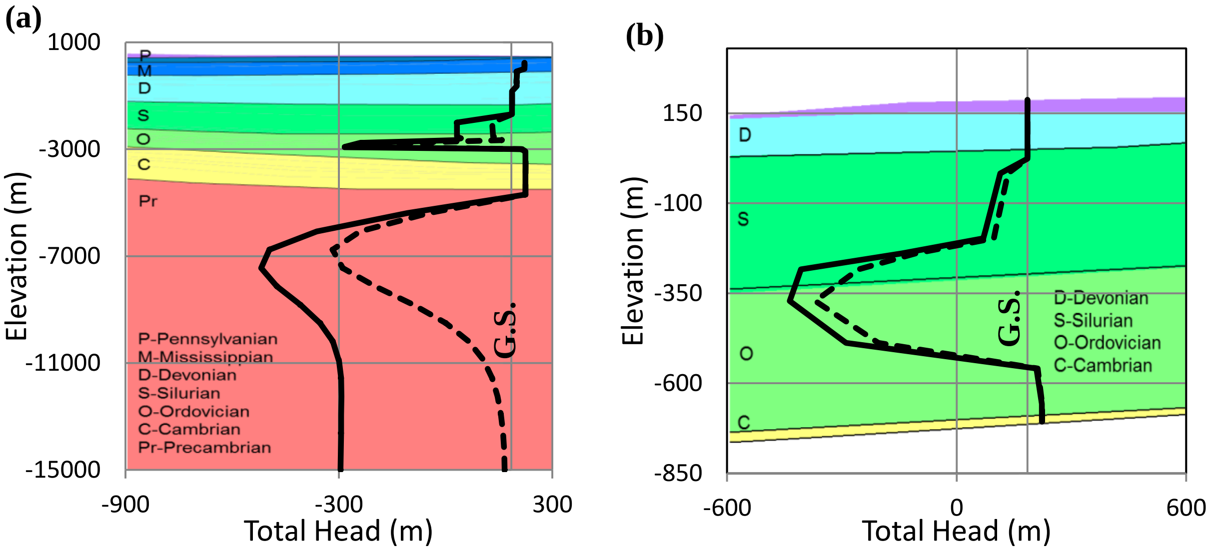

Figure 2.9: Total head (m) vs. elevation (m) for 1 cycle [dotted lines] and 10 cycles [solid lines], for glacial loading using nn9921, (a) at section B-B, (b) at the Bruce site as shown in Figure 2.1.

2.6.3 Extent of the Cambrian Aquifer

The importance of the Cambrian aquifer as a lower seepage boundary for the low permeable formations is tested in this simulation. The Cambrian layer was cut-off in the south west direction (Figure 2.10). Other initial and boundary conditions remain unchanged from the Base case. The model was run for one loading cycle (nn9921). The results show that the underpressures were only formed at the edges of the Michigan basin and disappeared from the middle portion. This clearly shows that the draining route for porewater from the low permeable formations is through the Cambrian aquifer.

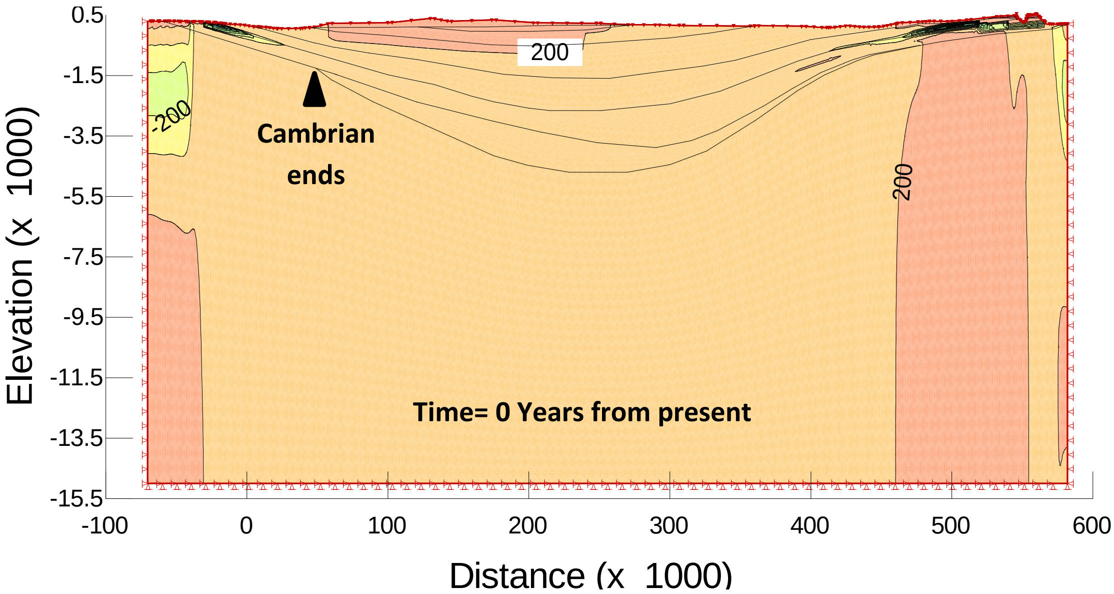

Figure 2.10: Total head at present under loading scenario nn9921 for one loading cycle, Removing Cambrian formations outcrop. Total heads are in m, dimensions in m.

2.6.4 Glacial Advance direction

In this simulation, the glacial advance direction was changed from the North West to the north east. In this case, the glacial loading advances in a parallel direction to the 2-D section. The ice load distribution was interpolated from Peltier (2011). Glacial loading values are as given in Figure 2.4 at the north east side (at the Bruce site) and around 0.75 of these values at the south west side of the given section. Other initial and boundary conditions remain unchanged from the Base case. The results show an increase in underpressures at the NE side under present conditions as shown in Figure 2.11.

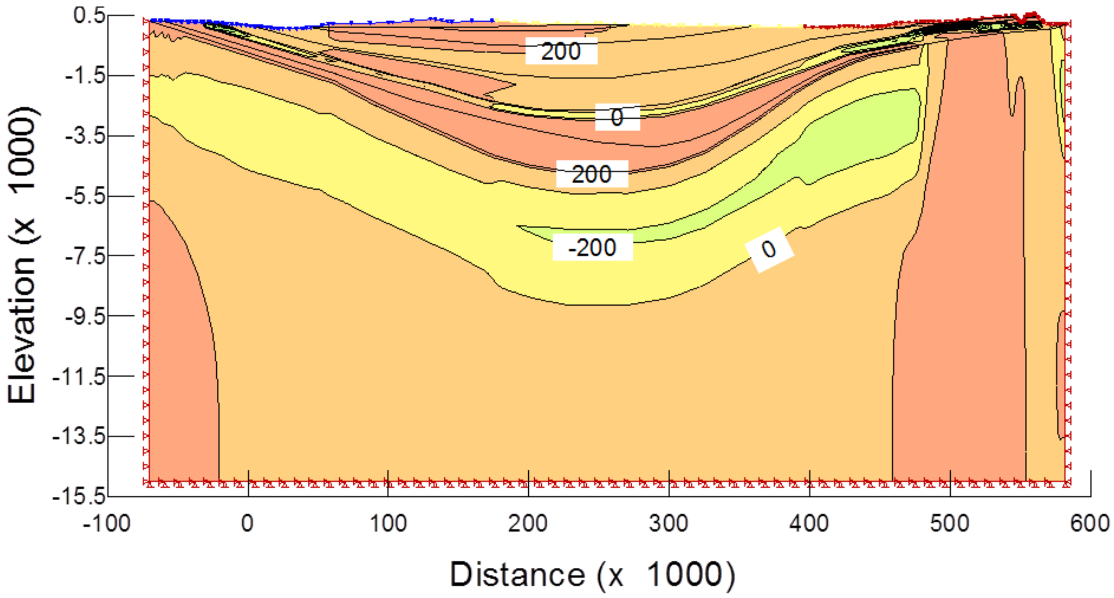

Figure 2.11: Total head at present under loading scenario nn9921 for one loading cycle, Glacial loading advance from north east direction. Total heads are in meters, dimensions in (m).

2.6.5 Mechanical load versus equivalent hydraulic head

The mechanical loads and the hydraulic heads which resulted from these loads were isolated and tested alone. The simulations present a comparison of the response of the formations and the generated heads under both conditions. For the mechanical loads, a dry base case was assumed at the rock-glacier interface. For hydraulic head, the mechanical loads were set to zero and water heads equivalent to the glacial loads were applied on the top boundary. The loading case used was the nn9921 model run. Other initial and boundary conditions remain unchanged from the base case. The results at the present time for the mechanical loads and the hydraulic heads are shown in Figure 2.12 and Figure 2.13, respectively. The response for both simulations shows a significant difference between the two assumptions. The mechanical loads generate an underpressure in the low permeability formations, while the hydraulic head generated an overpressure at the same locations.

The mechanical load exerted at the land surface increases the porewater pressure spontaneously in the domain. With time, pore water starts draining from the formations through escape routes. The pore water pressure in low permeability formations starts to decrease and the effective stress starts to increase. This causes a compaction to the rock formations. When the mechanical loads are removed, the layers rebound and underpressure is generated in low permeable formations.

The hydraulic head exerted at the land surface pushes water into the pores. Total head increases gradually depending on the hydraulic conductivity of the layer. The pore water pressure in low permeability formations starts to increase, while the effective stress starts to decrease. This causes a swelling in the rock formations. When the external hydraulic heads are removed, the layers settle back and overpressure is generated in low permeability formations.

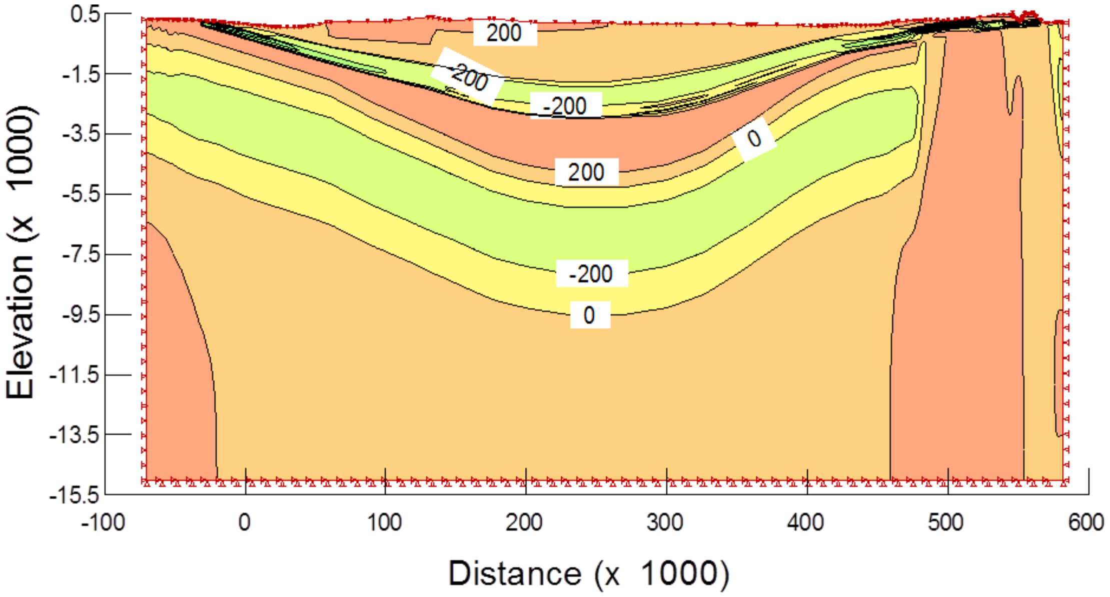

Figure 2.12: Total head at present under loading scenario nn9921 for one loading cycle, assuming dry base. Total heads are in meters, dimensions in (m).

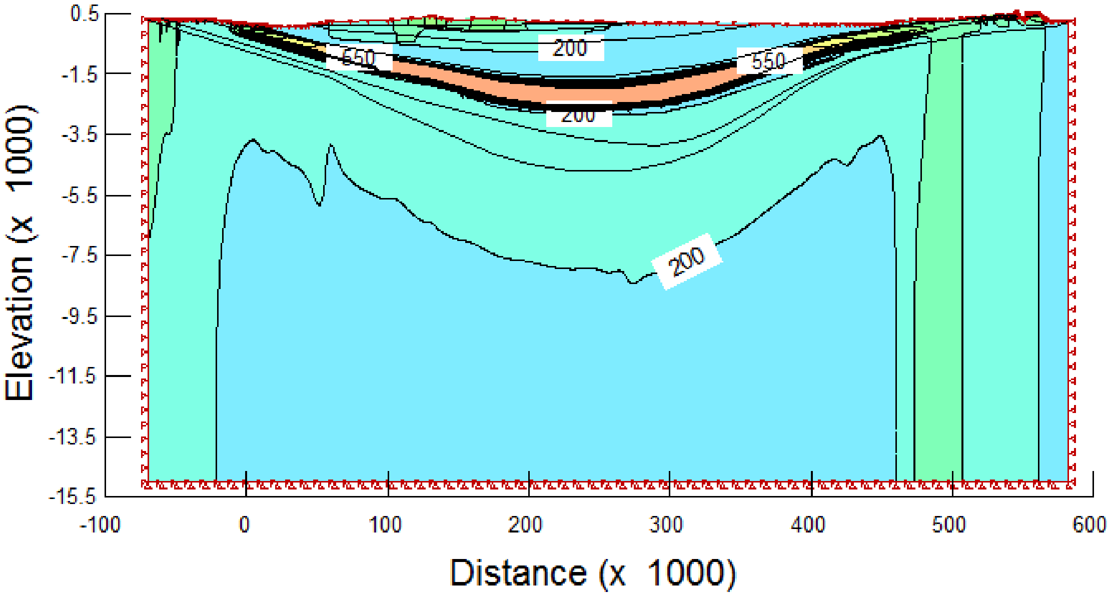

Figure 2.13: Total head at present under loading scenario nn9921 for one loading cycle, Converting glacial loads to hydraulic heads. Total heads are in meters, dimensions in (m).

2.6.6 Topographical effects

The model is used to test the topographic effects on the overpressure measured in the Cambrian formations. The elevation of the Cambrian formations at the SW end was raised to 400 m, and the model was loaded by one glacial cycle. The results show that the overpressure in the Cambrian aquifer was generated from topographic head from raising the elevation of the Cambrian outcrop as shown in Figure 2.14 and Figure 2.15.

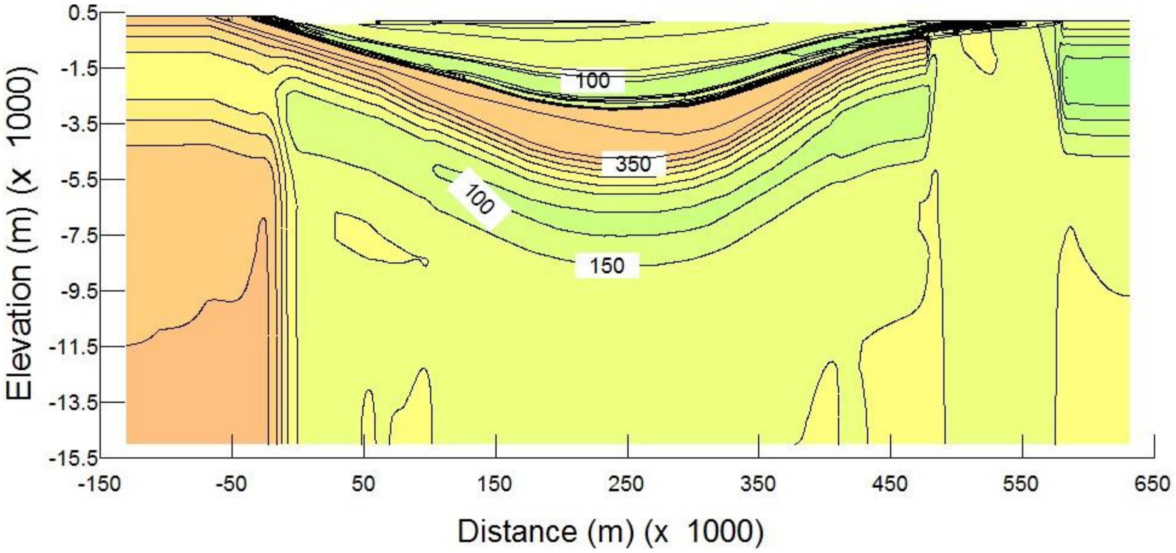

Figure 2.14: Total head at present under loading scenario nn9930 for one loading cycle, The elevation of the Cambrian layers outcrop was assumed to equal 400 m. Total heads are in meters, dimensions in (m).

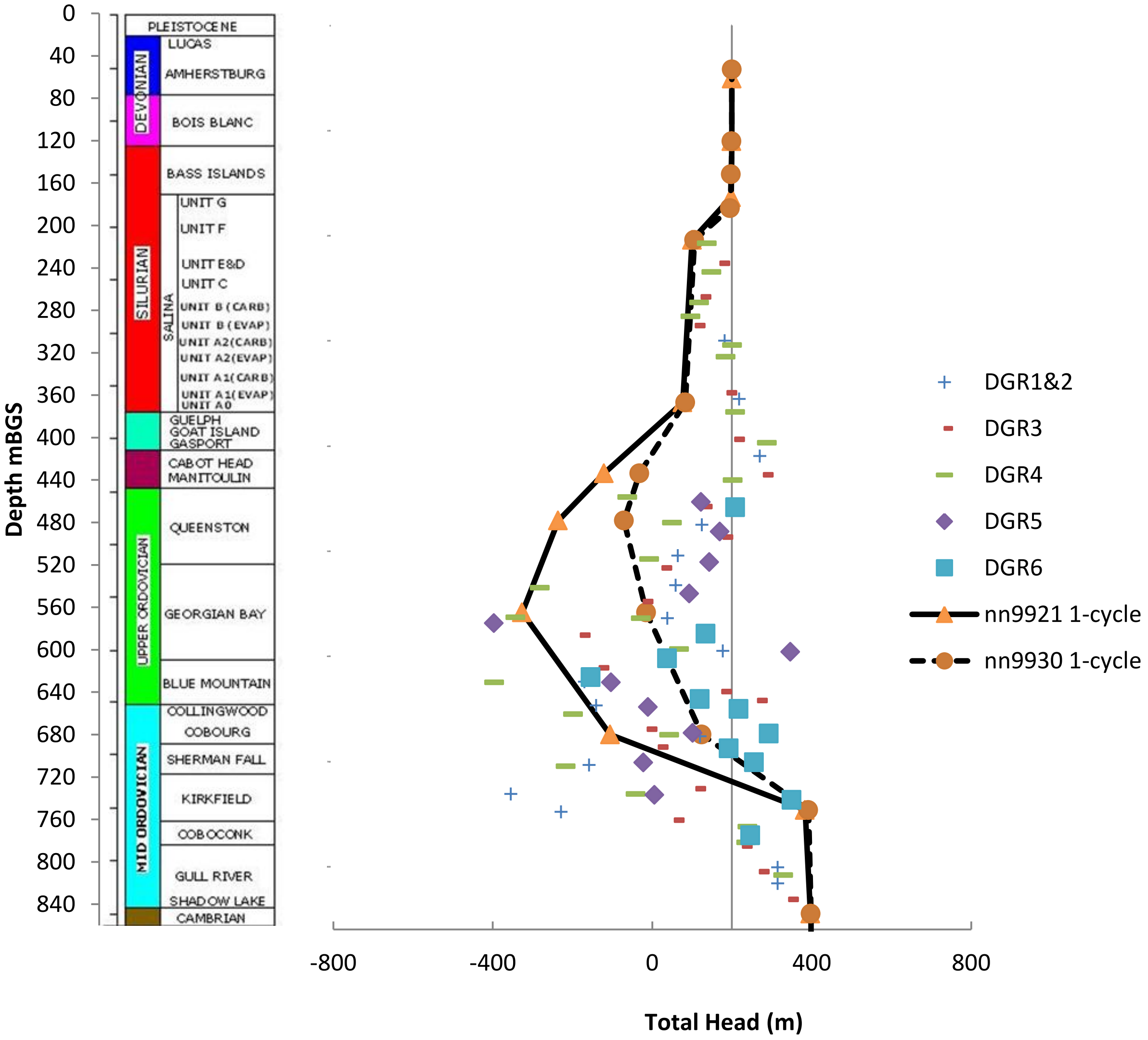

Figure 2.15: Total Head (m) versus Depth (m), the solid line represents simulation results after 1 loading cycle using loading case nn9921, the dotted line represents simulation results after 1 loading cycle using loading case nn9930. The overpressure in the Cambrian aquifer was generated from raising the elevation of the Cambrian outcrop.

2.6.7 Verification of the model results

The results for the hydromechanical models are compared with field estimation of the environmental heads in the rock formations. Figure 2.16 shows the results after 10 glacial cycles with two different loading cases, superimposed over the field data. Both of the model results fall in the envelope of field measurements. The underpressure in the Ordovician formations is well captured by the model while the overpressure in the Cambrian aquifer is lower than the measured values.

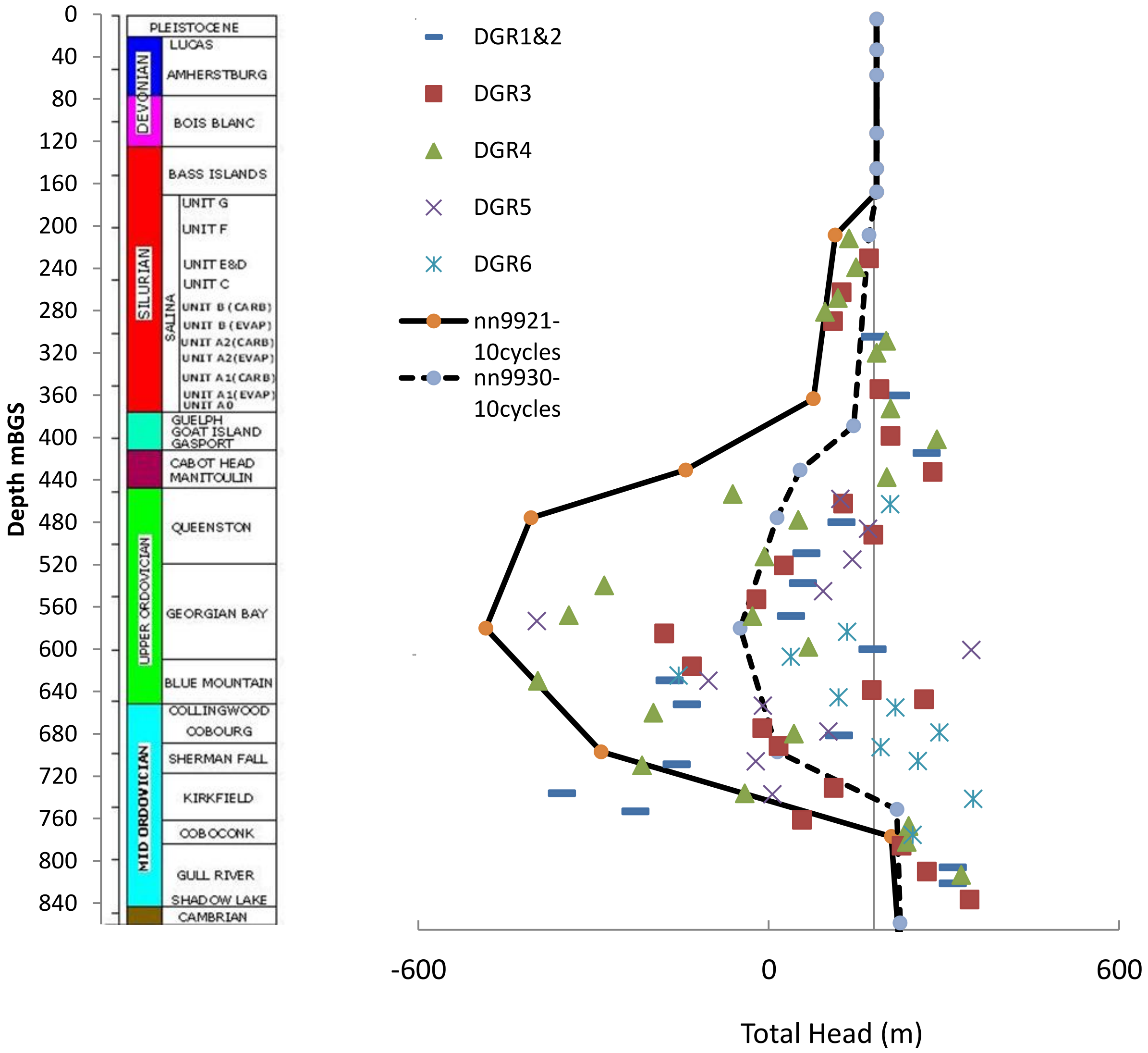

Figure 2.16: Total Head (m) versus Depth (m), the solid line represents simulation results after 10 loading cycles using loading case nn9921, the dotted line represents simulation results after 10 loading cycles using loading case nn9930.

2.7 Future work

The model results present a first view of the effect of mechanical loading and water head applied on ground surface on the abnormal pressure heads developed within Michigan basin formations. Future work needs to investigate the importance of density driven flow, permafrost, the presence of a gas phase and lithosphere flexure on the development of the overpressure in different locations in the domain.

2.8 Conclusions

The hydro-mechanical effects of the Pleistocene glacial loading cycles on the Michigan sedimentary basin is assessed using coupled stress and porewater pressure numerical analysis. Two-dimensional models of the Michigan basis were built extending from the NE to the SW direction. Several factors were considered in the analysis of different glacial loading scenarios including i) the number of loading cycles, ii) the effect of a wet/dry glacial-soil interface, iii) the direction of glacial advance, and iv) the effect of the deep Cambrian aquifer on the development of anomalous pressure heads.

The results for present day define regions of underpressure in the upper Ordovician and lower Silurian formations characterized by very low hydraulic conductivity and adjacent to the Cambrian aquifer. The results were verified against measured environmental heads from the Bruce Deep Geological Disposal Repository site.

Furthermore, the results confirm the hypothesis that under-pressure in the Ordovician and Silurian formations can be related to surface rebound due to glacial unloading. The Cambrian aquifer plays an important role in the development of the underpressures. The Cambrian formations present an escape route for pressurized porewater during loading periods. The overpressure in the Cambrian aquifer was not captured by the hydromechanical model, and was concluded to be generated from topographic head from raising the elevation of the Cambrian outcrop.

Moreover, our results also illustrate the difference between applying mechanical loads on the land surface and applying an equivalent hydraulic head in the generated total heads in the rock formations. The results show that hydraulic heads applied on the model surface in the hydromechanical loading reduce the generated underpressures. The dry based glacial loads are considered a more conservative scenario.

2.9 References

Al, T., Beauheim, R., Crowe, R., Diederichs, M., Frizzell, R., Kennell, L., Lam, T., Parmenter, A. and Semec B. (2011), Geosynthesis. Supporting technical report. NWMO DGR-TR-2011-11-R000.

Armstrong, D.K. and Carter, T.R., 2006. An updated guide to the subsurface Paleozoic stratigraphy of southern Ontario, Ontario Geological Survey, Open File Report 6191.

Bense, V. F., and M. A. Person (2008), Transient hydrodynamics within intercratonic sedimentary basins during glacial cycles, J. Geophys. Res., 113, F04005, doi:10.1029/2007JF000969.

Chilingar, G.V., Serebryakov, V.A., Robertson Jr., J.O. (2002), Origin and Prediction of Abnormal Formation Pressures, ELSEVIER 2002.

Corbet, T.F., and Bethke, C.M. (1992), Disequilibrium Fluid Pressures and Groundwater Flow in the Western Canada Sedimentary Basin; JOURNAL OF GEOPHYSICAL RESEARCH, VOL. 97, NO. B5, PAGES 7203-7217, MAY 10, 1992

Ehlers, J., Gibbard, P.L. (2007). The extent and chronology of Cenozoic global glaciation. Quaternary International, 164–165, 6–20.

Frizzell, R., Cotesta, L. and Usher, S. (2008). Phase I Regional Geology, Southern Ontario. Supporting technical report. OPG 00216-REP-01300-00007-R000.

Hays, J. D., Imbrie, J. and Shackleton, N. J. (1976), Variations in the Earth’s orbit: pacemaker of the ice ages. Science 194, 1121–1132. (doi:10.1126/science.194.4270.1121)

Howell, P.D., van der Pluijm, B.A., (1999). Structural sequences and styles of subsidence in the Michigan basin. Geol. Soc. Am. Bull., 111, 974-991

Imbrie, J., et al. (1993), On the structure and origin of major glaciation cycles 2. The 100,000-year cycle, Paleoceanography, 8(6), 699–735, doi:10.1029/93PA02751.

Jensen, M., Lam, T., Luhowy, D., McLay, J., Semec, B., and Frizzell R. (2009), Ontario Power Generation’s Proposed L&ILW Deep Geologic Repository: An Overview of Geoscientific Studies; GeoHalifax2009

Joyce, J., Tjalsma, L., and Prutzman, J., (1993). North American glacial meltwater history for the past 2.3 m.y.: Oxygen-isotope evidence from the Gulf of Mexico: Geology, v. 21, p. 483–486, doi: 10.1130/0091-7613(1993)021<0483:NAGMHF >2.3.CO;2.

Lemieux, J.-M., E. A. Sudicky, W. R. Peltier, and L. Tarasov (2008), Dynamics of groundwater recharge and seepage over the Canadian landscape during the Wisconsinian glaciation, J. Geophys. Res., 113, F01011, doi:10.1029/2007JF000838.

Matusevich, V. M., Myasnikova, G. P., Maximov, E. M., Volkov, A. M., Chistiakova, N. F., Kanalin V. G. and Pupilli, M., (1997). Abnormal formation pressures in the West Siberian Mega-basin, Russia. Petroleum Geoscience, Vol. 3 1997, pp. 269–283

McIntosh, J. C., GARVEN, G., and Hanor J. S. (2011), Impacts of Pleistocene glaciation on large-scale groundwater flow and salinity in the Michigan Basin; Geofluids (2011) 11, 18–33 doi: 10.1111/j.1468-8123.2010.00303.x

Michael, K., and Bachu, S. (2011), Fluids and pressure distributions in the foreland-basin succession in the west-central part of the Alberta basin, Canada: Evidence for permeability barriers and hydrocarbon generation and migration; AAPG Bulletin, v. 85, no. 7 (July 2001), pp. 1231–1252

Nasir, O., Fall, M., Nguyen, T.S., Evgin E. (2011), Modelling of the hydro-mechanical response of sedimentary rocks of southern Ontario to past glaciations, Engineering Geology 123 (2011) 271–287.

NEUZIL, C. E. (1993); Low Fluid Pressure Within the Pierre Shale' A Transient Response to Erosion; WATER RESOURCESR ESEARCH,V OL. 29, NO. 7, PAGES2 007-2020J, ULY 1993

Neuzil, C. E. (2003), Hydromechanical coupling in geologic processes; Hydrogeology Journal (2003) 11:41–83; DOI 10.1007/s10040-002-0230-8

Peltier, W.R. (2011). Long-Term Climate Change. Supporting technical report. NWMO DGR-TR-2011-14-R000

Peltier, W.R. (2002). On eustatic sea level history: Last Glacial Maximum to Holocene. Quaternary Science Reviews 21, 377–396

Percival, J.A. and Easton, R.M. (2007). Geology of the Canadian Shield in Ontario: an update; Ontario Geological Survey, Open File Report 6196, Geological Survey of Canada, Open File 5511, Ontario Power Generation, Report 06819-REP-01200-10158-R00, 65p.

Piotrowski, J.A., 1987. Genesis of the woodstock drumlin field, Southern Ontario, Canada. Boreas 16 (3), 249–265.

Raven, K., McCreath, D., R. Jackson, Clark, I., Heagle, D., Sterling, S. and Melaney, M., (2011), Descriptive Geosphere Site Model. Supporting technical report. NWMO DGR-TR-2011-24- R000.

Sykes, J.F., Normani, S.D. and Yin, Y. (2011). Hydrogeologic Modelling. Supporting technical report. NWMO DGR-TR-2011-16-R000

Vinard, P., Bobet, A., Einstein, H.H. (2001), Generation and evolution of hydraulic underpressures at Wellenberg, Switzerland; JOURNAL OF GEOPHYSICAL RESEARCH, VOL. 106, NO. B12, PAGES 30,593-30,605, DECEMBER 10, 2001

THIS PAGE HAS BEEN LEFT BLANK INTENTIONALLY

3 The Study of Natural Tracers Profiles in Low Permeable Formations of the Bruce Site Using Numerical Modeling

Abstract

Upscaling flow and solute transport parameters measured at the local field or lab scale to the large spatial and temporal scales related to nuclear waste disposal in deep geological formations is required to model the evolution time of natural isotope profiles. The study site is located at the Eastern edge of the Michigan Basin. The Paleozoic sedimentary rocks have a thickness of 860 m, and are divided into 38 different layers in a sequence of dolostones, limestones and shale. The domain is bounded by a Cambrian aquifer at the bottom, 150 m of conductive layers at the top, and by two conductive horizontal layers at depths of 180 and 320 m depth. The domain is characterized by anomalously low and high pressures as measured in several deep boreholes at a potential nuclear repository site (Bruce County, southern Ontario, Canada). In a previous study, the natural isotopes of water ($\delta^{18}O$ and $\delta^{2}H$) were determined from rock samples extracted from these deep boreholes. Diffusion coefficients and hydraulic properties were also measured.

We performed a series of diffusion and advection & diffusion models. The measured environmental heads were used as the driving force for advection, where the underpressure in the middle of the domain caused an upward and downward flow from the lower and upper boundary respectively.The effects of horizontal features were added to the best fit of these models. The results were compared with the natural isotopes profiles measured in deep boreholes. Initial and boundary conditions evolution time agrees with hydrogeological history. This confirms that parameters measured at small scales are plausible for formation scale. The results also show the important of advection on solute transport from the upper and lower boundaries. The activation time was reduced by an order of magnitude when taking the effect of advection transport.

Key words: Michigan basin, Diffusion, Advection, modeling, Nuclear water disposal.

3.1 Introduction

Sedimentary argillaceous formations are generally characterized by very low permeability rock that can retain hazardous wastes for a long time preventing potential impact on the biosphere. In particular, the natural barrier characteristics of these rocks make them a potential host for nuclear waste repositories. In a recent study (Raven et al., 2011); the diffusion and hydraulic properties of a proposed host formation at the Bruce site in southern Ontario, Canada (Figure 3.1) were measured using information gathered from boreholes and laboratory scale experiments.

Figure 3.1: The location of Bruce Site (Al et al, 2011)

Up-scaling of these measurements to the large temporal and spatial scales of the potential disposal of nuclear wastes required the use of natural isotopes profiles of oxygen and hydrogen (δ^{18}O and δ^{2}H), and the paleo-hydrogeological history of the host rocks (e.g. Desaulniers et al., 1981; Remenda et al., 1996; Hendry and Wassenaar, 1999; Rübel et al., 2002; Patriarche et al., 2004a,b; Gimmi et al., 2007; Savoye et al., 2008). Modeling of natural isotopes profiles provides further insight into fluid flow and solute transport within these formations over the time frame suitable for waste disposal scale.

In previous work by Gimmi et al., (2007), the isotope profiles in aquitards are surmised to be influenced by the change in the chemical or hydraulic condition of the delimiting aquifers. These effects propagate through the aquitard to a degree that depends on the duration of the disturbance, and the physical and chemical properties of the rock. The uncertainties accompanied by choosing the proper initial and boundary conditions when modeling these settings are added to the uncertainties in transport processes and governing parameters. This represents a challenge for the use of natural tracers to unravel long-term solute migration (Gimmi et al., 2007). Thus, additional hydrogeological information such as the change in hydraulic head over extended periods of time, and potential rock-water interactions, are required to assist with the interpretation of the isotopic composition profile.

In the study described by Raven et al. (2011), the limestone formations proposed to host a repository lie below shale layers 200 m in thickness. The limestone is bounded by a Cambrian-aged aquifer below and another aquifer above, 150m below the ground surface. The domain is characterized by underpressures in the Ordovician formations and overpressures in the Cambrian aquifer (Raven et al., 2011). The hydraulic gradient reaches a value of 4 m/m at some depths in the stratigraphy, orders of magnitude larger than other sites proposed for nuclear waste disposal (eg. Benken site , Switzerland (Gimmi et al., 2007 and Mazurek et al., 2011)) or any other site known in sedimentary rock . These observations at the Bruce site provide a good opportunity to test the feasibility of using field measured hydraulic conductivity, laboratory measured porosity, and the distribution of the natural isotopes of water to unravel the paleo-hydrogeological conditions and explore the effects of advection. The isotopes were determined from rock samples extracted from six deep boreholes at the Bruce site by using vacuum distillation at 150°C (Hobbs et al., 2008). Diffusion coefficients were measured using X-ray radiographic technique and diffusion cells and hydraulic testing (pulse, slug, and drill-stem tests) were conducted to determine hydraulic conductivity (Raven et al, 2011).

Previous studies of solute transport in sedimentary formations have largely concluded that diffusion is the dominant solute transport process (Rübel et al., 2002; Gimmi et al., 2007; Savoye et al., 2008; Mazurek et al., 2011). The advection process is either absent or has a small effect on solute transport (Gimmi et al., 2007 and Mazurek et al., 2011), where hydraulic gradient is as little as 0.001 m/m in these sites, and upward or downward flow was assumed for the whole domain.

In this study, numerical modeling of the Bruce site is used to provide insight into the solute transport processes f that gave rise to the profile of δ18O and δ2H in the stratigraphic section. Specifically, we tested the hypotheses that: (i) Diffusion is the dominant solute transport process in this setting; (ii) Advection and dispersion processes play a role in solute transport from the upper and the lower boundaries. (iii) Solute transport parameters measured at local scale may be used to assist in determining the hydrogeological history of the site.

3.2 Site Description

The study area is located in a tectonically quiet region on the eastern margin of the intracratonic Michigan basin (Gartner Lee Limited, 2008). The formations beddings dip gently towards the center of the Michigan Basin, on this basis the layers at the study site are flat lying and continuous. The Paleozoic formations of the Michigan basin were deposited directly over the metamorphic rocks of the Precambrian basement within the depression of the basin. The descriptions of the main stratigraphic of the Paleozoic formations are adapted from Armstrong and Carter (2006) and Sykes et al. (2011) listed as follows.

The basal Cambrian units 860 mBGS (Below Ground Surface) with a thickness of around 20m range from fine to medium crystalline dolostone, sandy dolostone, argillaceous dolostone to to fine and coarse sandstone, and are described as porous and permeable formation. The basal Mt. Simon is considered as a regional aquifer (Vugrinovich, 1986).

The Middle Ordovician Carbonates overlying the Cambrian deposits with a thickness of around 195m are divided into Black River Group and Trenton Group. The Black River Group rocks include the Shadow Lake, Gull River, Coboconk Formations. The Trenton Group include the Kirkfield, Sherman Fall, Cobourg Formations (proposed to host the DGR repository). These carbonate rocks are generally characterized as limestones to argillaceous limestones.

Upper Ordovician shale overlying the Ordovician limestones with a thickness of around 210m is divided into the Blue Mountain, Georgian Bay and Queenston Formations. These units are generally composed of non-calcareous to calcareous shales with minor siltstone and carbonate interbeds.

The Lower and Middle Silurian rocks with a thickness of around 70m includes the Manitoulin Formation dolostones, Cabot Head Formation shales of the Lower Silurian and the dolostones of the Fossil Hill, Lions Head, Gasport, Goat Island and Guelph Formations of the Middle Silurian.

The Upper Silurian Formations with a thickness of around 255m consists of the Salina Group units G to A0 dolostones, evaporates (halite, anhydrite and gypsum) and shale, and the Bass Islands Formations dolostone. The Bass Islands is considered as a regional aquifer (Vugrinovich, 1986).

The Devonian formations with a thickness of around 110m represent the youngest rocks in the study area. The lower Devonian includes Bois Blanc Formation dolostones. The Middle Devonian capping the lower Devonian includes limestones and dolostones of the Detroit River Group (Amherstburg and Lucas Formations). The dolostone Lucas Formation subcrops beneath the overburden at the study site and outcrops along the shoreline of Lake Huron.

A multi-year site investigation program is being conducted at the Bruce site (approximately 190 km west of Toronto), where several vertical and inclined deep boreholes and 2-D seismic survey were conducted (Raven et al., 2011). The results show no evidence of vertical faults presence at the site location.

The hydrogeolocial characteristics of the Bruce site formations are summarized in table 3.1. The data were collected from Raven et al. (2011). The lithostratigraphy encountered in the Bruce deep boreholes are shown in Figure 3.2.

3.3 Environmental Isotopes in groundwater

Porewater was extracted from crushed DGR cores at the University of Ottawa by high-temperature vacuum distillation (150°C) for water isotopes for 6 h duration (Raven et al., 2011). The methods were carefully conducted and the results are believed to be representative. The analytical error associated with the results by measured vacuum distillation (150°C) is ±0.2‰ for $\delta^{18}O$ and ±2‰ for $\delta^{2}H$ (Raven et al., 2011).

δ18O and δ2H are plotted with respect to the Global Meteoric Water Line (GMWL δ2H=8*δ18O+10) to evaluation data trends and sources as shown in Figure 3.3a. Data points were reproduced from INTERA (2011 DGSM). The modern precipitation in southern Ontario varies between -12‰ to -10‰, for $\delta^{18}O$ and -85‰ to -70‰ for $\delta^{2}H$.

Figure 3.3b shows the variation of deuterium excess ($D_{excess} = \delta^{2}H - 8\ \delta^{18}O$) with depth. The permeable Devonian and upper Silurian are showing a constant value of +12‰ to a depth of 175 mBGS. A reduction in deuterium excess to about –30‰ occurs in the Guelph and Lower Silurian formations (400 mBGS) resulting from the depletion in δ18O with depth. D_{excess} enriched from the Guelph Formation to the Gull River limestone (800 mBGS) reaching a value of about +20‰. Values are then reversed down to around 0‰ in the Cambrian formations (860 mBGS).

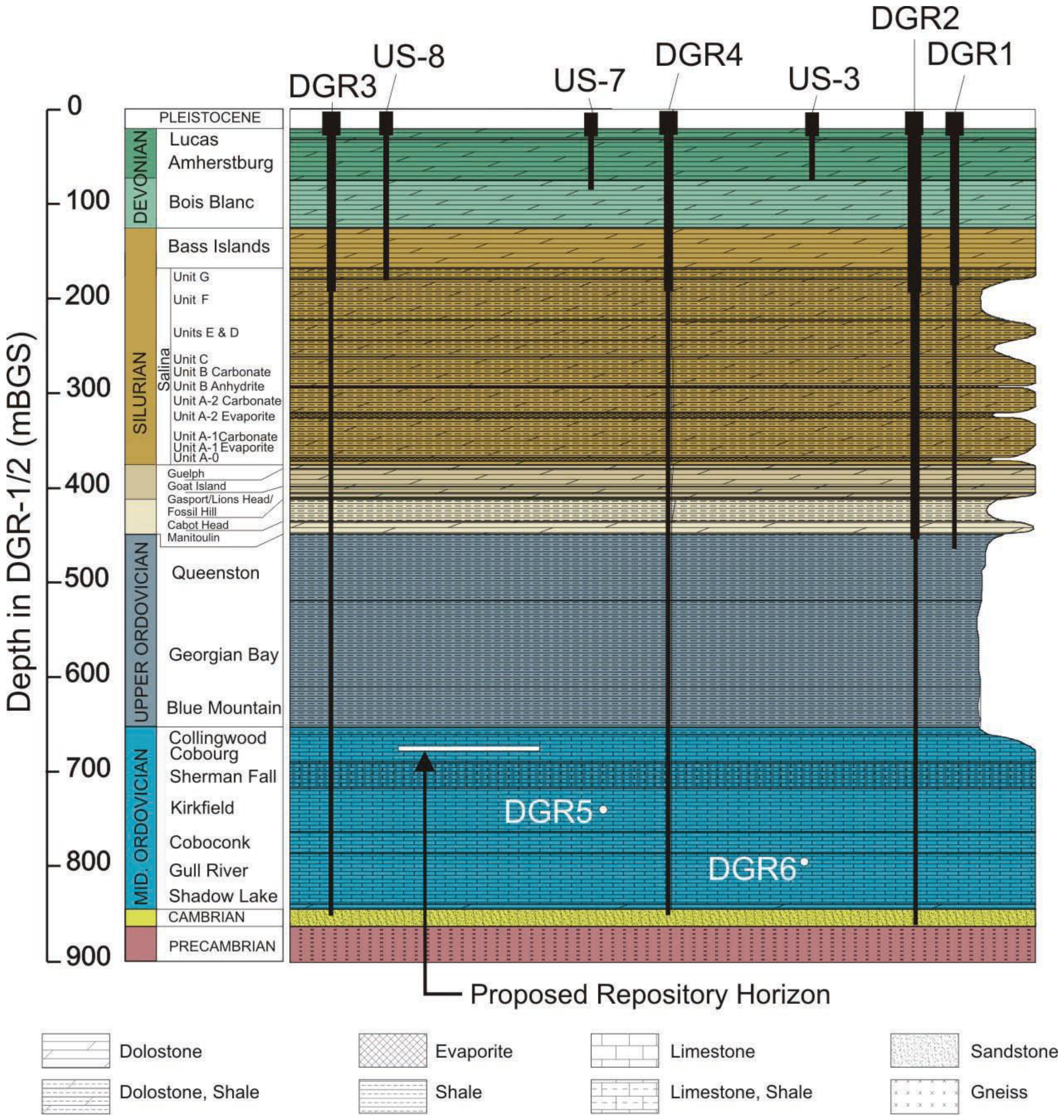

Figure 3.2: The extent and loctions of the deep borehole relative to the proposed repositories at the Bruce site (Al et al., 2011).

Data points from the deep boreholes shown in (Figure 3.3a) were separated by depth into four sections in Figure 3.4. Sedimentary basin brines plot to the right and below of the GMWL as shown in Figure 3.4 at depths from 400 to 650 mBGS. Some samples (at 650 to 800 mBGS) plotted over the GMWL are suspected to reflect isotope contributions from mineralogically bound waters (Raven et al., 2011) as shown in Figure 3.4.

Table 3-1 Summary of formations parameters at the Bruce site

Period	**Formation**	**K_H [m/s]**	**K_V [m/s]**	**K_H:K_V**	**θ**	**ρ [kg/m^3]**	**S_s [m^{-1}]**	**$D_{e\text{-}v}$ [m^2/s]**
Quaternary	Drift	1.0×10^{-8}	5.0×10^{-9}	2:1	0.200	1,000	9.9×10^{-5}	6.0×10^{-10}
Devonian	Lucas	1.0×10^{-6}	1.0×10^{-7}	10:1	0.077	1,000	1.0×10^{-6}	6.0×10^{-12}
	Amherstburg (top 20 m)	1.0×10^{-6}	1.0×10^{-7}	10:1	0.077	1,001	1.0×10^{-6}	6.0×10^{-12}
	Amherstburg (lower 25 m)	1.0×10^{-7}	1.0×10^{-8}	10:1	0.077	1,001	1.0×10^{-6}	6.0×10^{-12}
	Bois Blanc	1.0×10^{-7}	1.0×10^{-8}	10:1	0.077	1,002	1.0×10^{-6}	6.0×10^{-12}
Silurian	Bass Islands (upper 20m)	1.0×10^{-4}	1.0×10^{5}	10:1	0.056	1,004	1.3×10^{6}	1.3×10^{-11}
	Bass Islands (lower 25 m)	1.0×10^{-5}	1.0×10^{-6}	10:1	0.056	1,004	1.3×10^{-6}	1.3×10^{-11}
	Salina G	1.0×10^{-11}	1.0×10^{-12}	10:1	0.172	1,010	8.7×10^{-7}	4.3×10^{-11}
	Salina F	5.0×10^{-14}	5.0×10^{-15}	10:1	0.100	1,040	7.2×10^{-7}	4.1×10^{-12}
	Salina E	2.0×10^{-13}	2.0×10^{-14}	10:1	0.100	1,083	5.1×10^{-7}	4.7×10^{-12}
	Salina D	2.0×10^{-13}	2.0×10^{-14}	10:1	0.089	1,133	4.9×10^{-7}	4.7×10^{-12}
	Salina C	4.0×10^{-13}	4.0×10^{-14}	10:1	0.205	1,166	8.8×10^{-7}	1.1×10^{-11}
	Salina B	4.0×10^{-13}	4.0×10^{-14}	10:1	0.145	1,214	7.2×10^{-7}	1.2×10^{-11}
	Salina B evaporite	3.0×10^{-13}	3.0×10^{-14}	10:1	0.089	1,214	5.3×10^{-7}	7.7×10^{-14}
	Salina A2 carbonate	3.0×10^{-10}	3.0×10^{-11}	10:1	0.120	1,091	5.7×10^{-7}	1.2×10^{-12}
	Salina A2 evaporite	3.0×10^{-13}	3.0×10^{-14}	10:1	0.089	1,030	4.5×10^{-7}	7.7×10^{-14}
	Salina A1 Upper carbonate	2.0×10^{-7}	2.0×10^{-7}	1:1	0.070	1,019	3.9×10^{-7}	4.9×10^{-12}
	Salina A1 carbonate	9.0×10^{-12}	9.0×10^{-13}	10:1	0.019	1,128	2.8×10^{-7}	1.8×10^{-13}
	Salina A1 evaporite	3.0×10^{-13}	3.0×10^{-14}	10:1	0.007	1,217	2.6×10^{-7}	3.0×10^{-14}
	Salina A0	3.0×10^{-13}	3.0×10^{-14}	10:1	0.032	1,240	3.5×10^{-7}	3.0×10^{-13}
	Guelph	3.0×10^{-8}	3.0×10^{-8}	1:1	0.057	1,247	3.1×10^{-7}	3.2×10^{-12}
	Goat Island	2.0×10^{-12}	2.0×10^{-13}	10:1	0.020	1,200	1.8×10^{-7}	1.5×10^{-13}
	Gasport	2.0×10^{-12}	2.0×10^{-13}	10:1	0.020	1,200	1.8×10^{-7}	1.5×10^{-13}
	Lions Head	5.0×10^{-12}	5.0×10^{-13}	10:1	0.031	1,200	2.1×10^{-7}	6.2×10^{-12}
	Fossil Hill	5.0×10^{-12}	5.0×10^{-13}	10:1	0.031	1,200	2.1×10^{-7}	1.6×10^{-11}
	Cabot Head	9.0×10^{-14}	9.0×10^{-15}	10:1	0.116	1,204	7.7×10^{-7}	3.1×10^{-12}
	Manitoulin	9.0×10^{-14}	9.0×10^{-15}	10:1	0.028	1,233	5.1×10^{-7}	1.5×10^{-13}
Ordovician	Queenston	2.0×10^{14}	2.0×10^{15}	10:1	0.073	1,207	6.4×10^{7}	1.0×10^{-12}
	Georgian Bay	3.0×10^{-14}	3.0×10^{-15}	10:1	0.071	1,205	6.3×10^{-7}	4.3×10^{-13}
	Blue Mountain	5.0×10^{-14}	5.0×10^{-15}	10:1	0.078	1,197	1.3×10^{-6}	8.2×10^{-13}
	Collingwood	2.0×10^{-14}	2.0×10^{-15}	10:1	0.012	1,150	2.5×10^{-7}	4.9×10^{-13}
	Cobourg	2.0×10^{-14}	2.0×10^{-15}	10:1	0.015	1,181	1.8×10^{-7}	3.7×10^{-13}
	Sherman Fall	1.0×10^{-14}	1.0×10^{-15}	10:1	0.016	1,180	3.7×10^{-7}	4.2×10^{-13}
	Kirkfield	8.0×10^{-15}	8.0×10^{-16}	10:1	0.021	1,156	3.8×10^{-7}	2.2×10^{-13}
	Coboconk	4.0×10^{-12}	4.0×10^{-15}	1,000:1	0.009	1,170	3.4×10^{-7}	2.7×10^{-13}
	Gull River	7.0×10^{-13}	7.0×10^{-16}	1,000:1	0.022	1,135	3.7×10^{-7}	2.6×10^{-13}
	Shadow Lake	1.0×10^{-9}	1.0×10^{-12}	1,000:1	0.097	1,133	5.9×10^{-7}	6.1×10^{-12}
Cambrian	Cambrian	3.0×10^{-6}	3.0×10^{-6}	1:1	0.071	1,157	3.2×10^{-7}	7.7×10^{-12}

Reproduced from Raven et al. (2011) and Sykes et al. (2011)

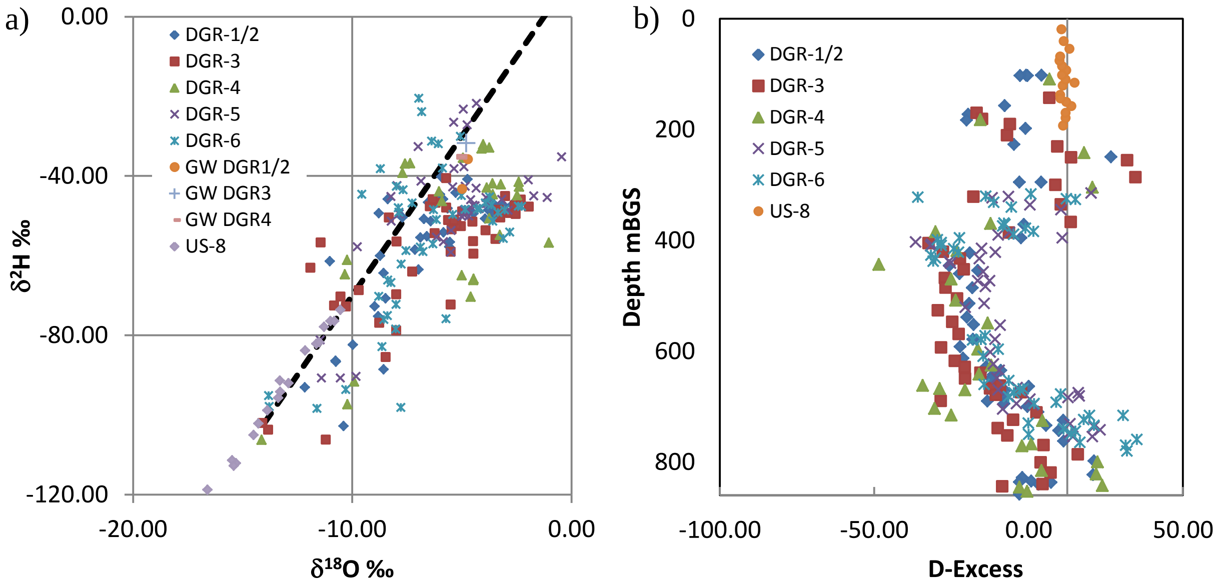

Figure 3.3: a) δD and δ^{18}O from 6 different deep boreholes (DGR-1 to DGR-6) with respect to the Global Meteoric Water Line (GMWL δD = 8 δ^{18}O + 10) [dotted line], where (A) glacial water isotopes composition, (B) Meteoric water isotopes composition, (A) Brine water isotopes composition, b) D-excess (D_{excess} = δD - 8 δ^{18}O) versus depth. Data points are from Raven et al. (2011).

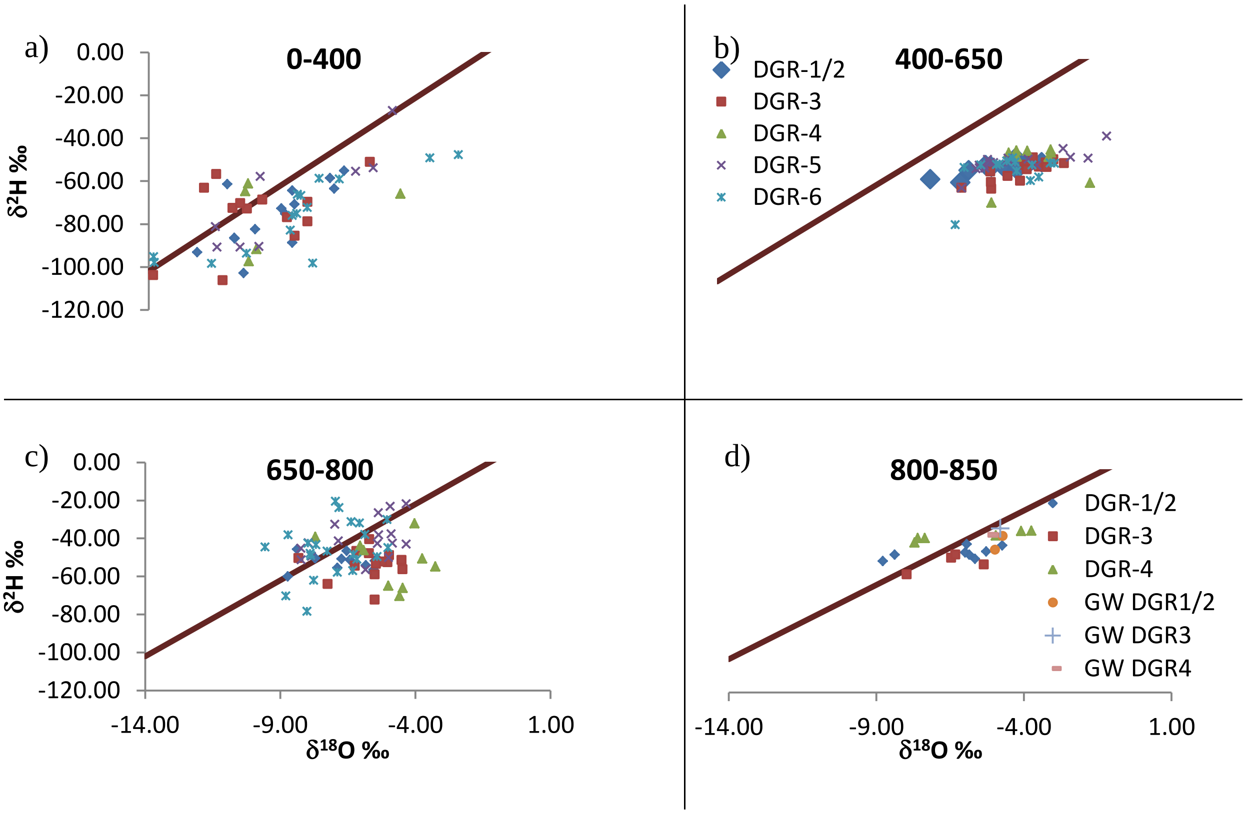

Figure 3.4: a) δD and δ^{18}O of deep boreholes with respect to the Global Meteoric Water Line (GMWL),a) data points from 0 to 400 mBGS, b) data points from 400 to 650 mBGS, c) data points from 650 to 800 mBGS, d) data points from 800 to 850 mBGS.

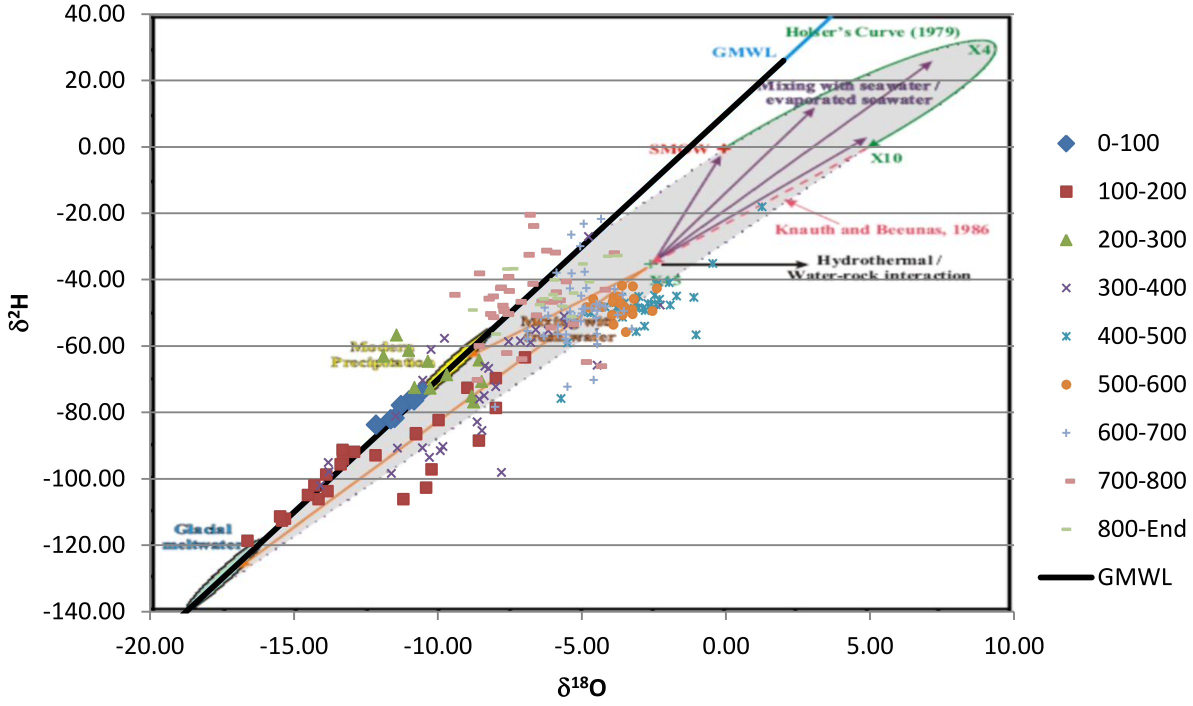

Figure 3.5: δD and δ^{18}O from 6 different deep boreholes (DGR-1 to DGR-6) with respect to the Global Meteoric Water Line. The data are divided to 9 series of a 100 m of depth each. The data points are superimposed on a graph from Shouakar-Stash (2008).

Figure 3.6a and Figure 3.6b shows the isotopic composition of the δ^{18}O and δ^{2}H collected from DGR1-6 and US-8 with depth. Porewater isotopes show an enrichment with depth in the Devonian and upper Silurian formations to the depth of the Guelph formation. Bios Blanc and Salina A2 formations show depleted values (mixture of Glacial and Meteoric water). The Guelph formation has enriched values with water composition of -3.5‰ & -48‰ for δ^{18}O and δ^{2}H respectively (similar to the basin fluids). Values are then depleted in the Ordovician formations towards the Gull River. An average slope of isotopes depletion within the Ordovician formations is (0.0041*D from 400 to 600 m, where D is the depth in m & 0.025*D from 600 to 750 m) for δ^{18}O and (0.0068*D from 400 to 700m) for δ^{2}H. Values are then enriched to a value of -4‰ & -30‰ for δ^{18}O and δ^{2}H respectively at the Cambrian aquifer.

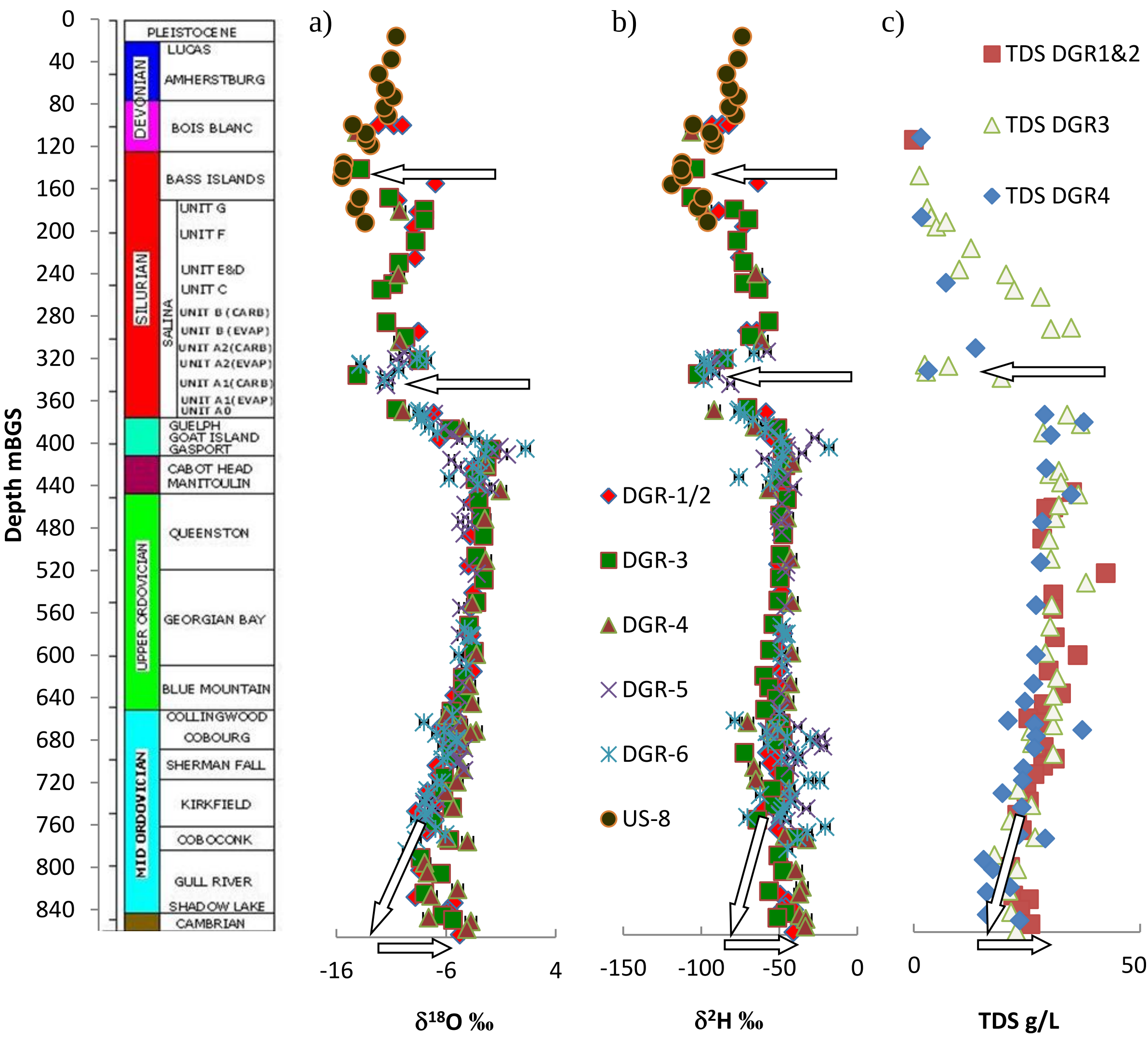

Figure 3.6: The isotopic composition of the a) $\delta^{18}O$, b) δ^2H and c) Total dissolved solids TDS collected from DGR1-6 and US-8 with depth in m. The arrows will be discussed in the conceptual model.

Groundwater samples in addition to porewater were collected from four depths at which the permeability of the rock was high enough to obtain water by abstraction. Samples were obtained from the Cambrian aquifer at a depth of 860 mBGS, the Guelph formation at a depth of 370 mBGS, the Salina A2 formation at a depth of 320 mBGS and from the Devonian and upper Silurian formations from ground surface up to a depth of 180 mBGS. The isotopic composition from these samples show an agreement with porewater measured form rock samples for the first two locations and appears more depleted for the second two samples as shown in Figure 3.7 (Raven et al., 2011).

The potential end-members for the isotope content of the porewater are seawater (SMOW), evaporated seawater, modern precipitation, and glacial melt-water. The evolution of porewater is influenced by numerous processes which include mixing between various end members, seawater evaporation, hydrothermal activity, and water-rock interactions (Hobbs et al., 2008). . Sources of porewater in sedimentary formations include original seawater trapped during sedimentation, evaporated water trapped in precipitated salt, amodern meteoric water and ancient Pleistocene glacial water (Kharaka and Hanor, 2005).

The shaded area in Figure 3.5 represents mixing between the main end members. The data points show several water end-members, modern meteoric water, glacial water and brine water (water-rock interactions). The data also show mixing between the end members, mixing between modern meteoric water and glacial water, and mixing between modern meteoric water, glacial water and brine.

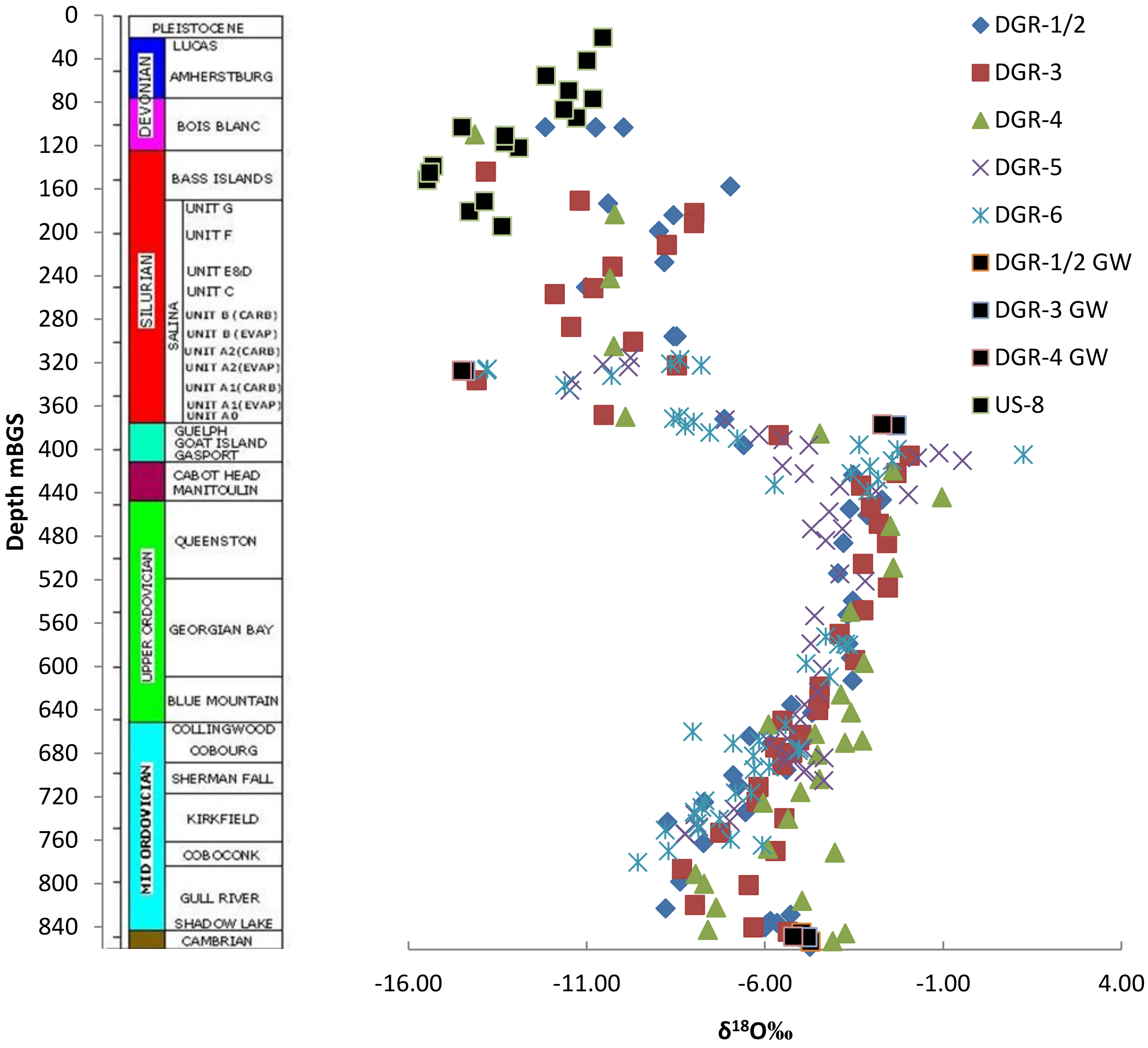

Figure 3.7: The isotopic composition of the δ^{18}O with depth collected from DGR1-6 and US-8 with depth in (m). Groundwater samples are shown as black squares.

3.4 Method

To investigate the impact of various changes in paleo-hydrogeological conditions, numerical study was undertaken. The study was conducted using the model HydroGeoSphere (HGS). This code was selected for this study as it has wide capability for accommodating advection and diffusion in complex fractured and porous media settings. The model also has a robust formulation which well-simulates free convective flows which occur as a result density gradients in saline systems. Remnant overpressures from glacial advances can also be captured using this model (Therrien et al., 2008).

The solute transport equation for HGS is given by (Therrien et al., 2008):

$$-\nabla W_m(qC - \theta_s S_w D\nabla C) + [W_m\theta_s S_w R\lambda C]par + \sum\Omega_{ex} \pm Q_c = W_m[\frac{\partial\theta_s S_w RC}{\partial t} + \theta_s S_w R\lambda C] \tag{3.1}$$

Where $W_m$is the volumetric fraction of the total porosity occupied by the porous medium, λ is the first order decay constant [L^{-1}], Q_c is the solute exchange with outside of the domain [$ML^{-3}T^{-1}$], C solute concentration [ML^{-3}], *par* is for the parental species, the hydrodynamic dispersion tensor D [L^2 T^{-1}] for HGS is given by Bear, (1972), and where the effective diffusion coefficient is obtained by multiplying D_o by porosity and tortuosity:

$$\theta_s S_w D = (\alpha_l - \alpha_t)\frac{qq}{|q|} + \alpha_t|q|I + \theta_s S_w D_{free}\tau I \tag{3.2}$$

Where D_{free} is the free solution diffusion coefficient [L^2 T^{-1}] , and I is the identity tensor. τ is the matrix tortuosity [dimensionless], $\alpha_l$and α_t are the longitudinal and transverse dispersivities [L] respectively and $|q|$ is the magnitude of the Darcy flux.

The flow equation is given by:

$$-\nabla.(W_m q) + \sum\Gamma_{ex} \pm Q = W_m\frac{\partial(\theta_s S_w)}{\partial t} \tag{3.3}$$

The Darcy equation in the unsaturated case is given by:

$$q = -Kk_r\nabla(\Psi + Z) \tag{3.4}$$

Where K is the hydraulic conductivity tensor [LT^{-1}] k_r is the permeability with respect to saturation, Ψ is the pressure head [L] and Z is the elevation head [L].

3.5 Conceptual Model

A conceptual model was built for the Bruce site based on the understanding of the data available from site characterization, geochemistry and paleo-hydrogeological information for the study area. Conservative solute transport was assumed for stable isotopes and for the comparison between diffusion-dominant solute transport and advective solute transport.

The profiles of $\delta^{18}O$, $\delta^{2}H$ and TDS, as shown in Figure 3.6, define specific trends that will be discussed as follows. The top of the domain (Quaternary deposits) shows isotopic values typical of modern precipitation and shows fresh water TDS concentration. Ground surface was set as the upper boundary of the model domain. The ground-surface overlies aquifer layers of around 150 m in thickness. The upper boundary was also covered by glacial loading during Pleistocene glacial cycles as shown in (Figure 3.8). The ice thickness during Pleistocene glacial cycles was developed by University of Toronto Glacial Systems Model (UofT GSM) (Peltier, 2011).

Two depths within the Salina units (320 mBGS), and Bois Blanc and Bass Islands (150-180 mBGS) have more depleted $\delta^{18}O$ and $\delta^{2}H$ than surrounding layers. The isotope compositions range between glacial water and a mixture of glacial and modern water. The discharge from glacial water during Pleistocene glacial cycles with a wet base is hypothesized as the cause. These layers are characterized by relatively higher horizontal hydraulic conductivity, and the site lies on the edge of the Michigan basin. Invasion of glacial water from the layer outcrop at the Basin edge is the most likely hypothesis.

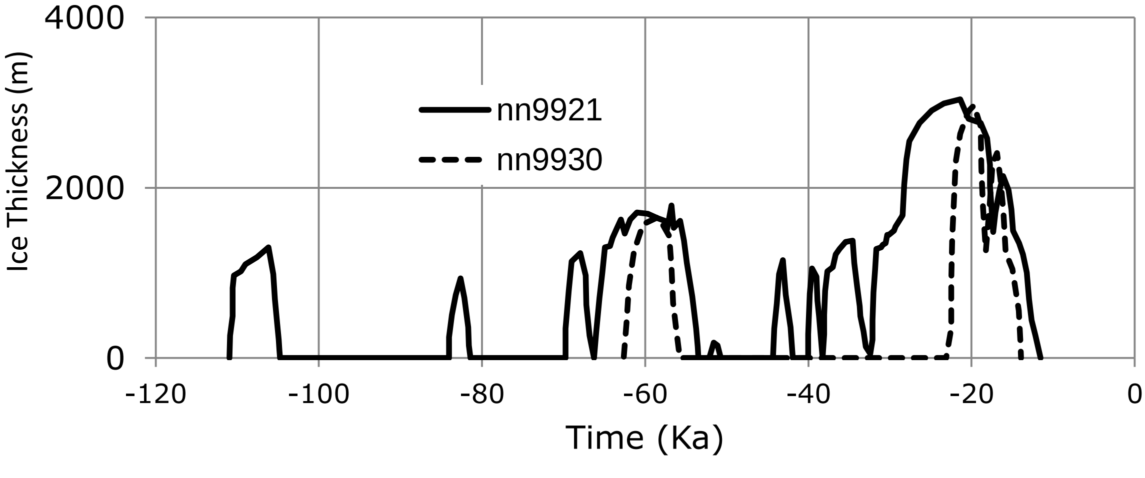

Figure 3.8: Ice loading scenarios at the Bruce site interpolated by the University of Toronto Glacial Systems Model (UofT GSM), Peltier (2011). Model runs nn9921 and nn9930 are shown.

The lower part of the domain (Cambrian aquifer) shows a change in isotopic composition and TDS concentration that occurred sometime in the past. This started with a depleted isotope concentration and lower TDS water and turns to more enriched isotopes and higher TDS. The Cambrian aquifer is considered the lower boundary for flow and transport in the domain.

The glacial loading and unloading on the top of the domain will generate changes in pore water pressure, and impact the hydraulic conductivity and porosity of individual formations with time. The anomalous pressures resulted from the glacial loading applied on land surface are discussed in (Chapter 2.0). The measured anomalous heads at the Bruce site are shown in Figure 3.9. The effect of over and under pressures on solute transport processes must also be addressed in the simulation of solute transport.

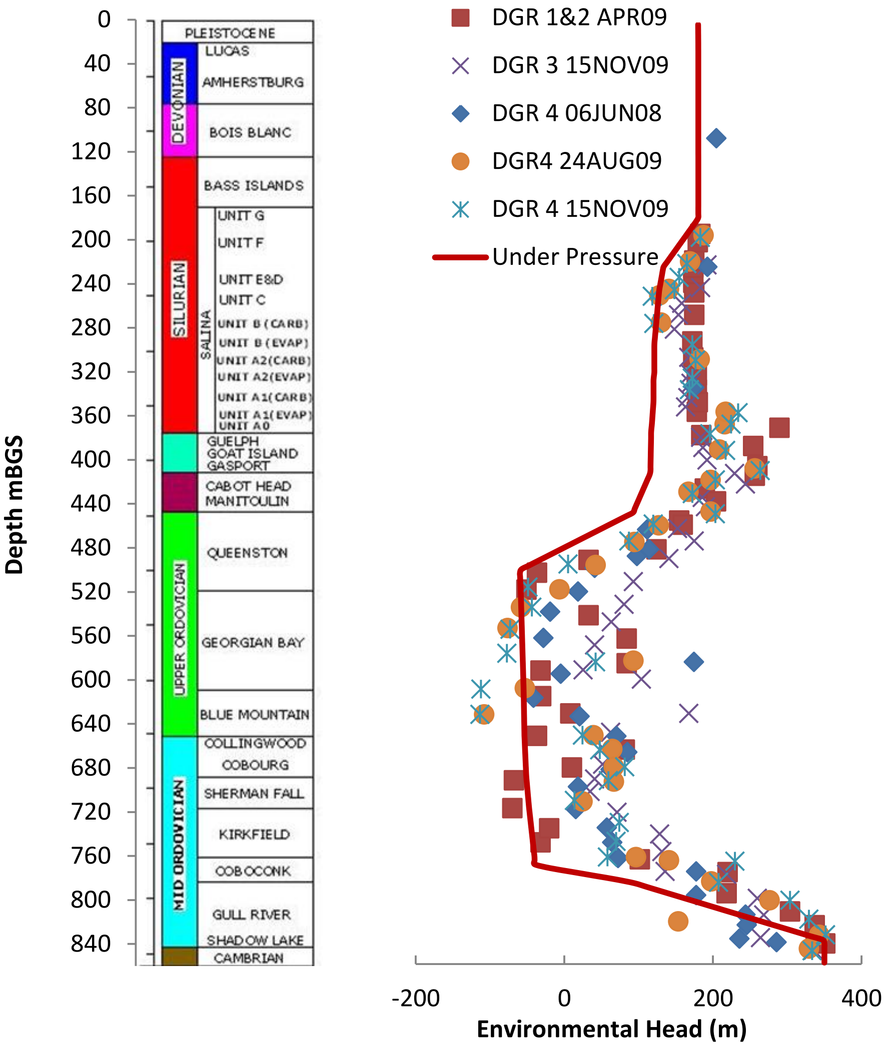

Figure 3.9: Environmental Head (m) with depth in (mBGS) at the Bruce site. The data represent five different measurements. The solid line indicates the head used in the model.

3.5.1 Model geometry

The one dimension solute transport model in the z-direction is built as shown in Figure 3.10. The domain is divided into 38 sub-layers. The characteristics of these rocks are presented in Table 3.1. The domain is 10x10x860 m in the x, y and z directions respectively. The element size is equal to 1x1x1 m in all layers. The domain is sandwiched between two aquifers, one at thetop that extends to 150 mBGS and the 2nd at the bottom (the Cambrian aquifer) from 840-860 m. Water isotopes, TDS and horizontal hydraulic conductivity data show two horizontal features with glacial water supply at 320 and 150 mBGS, and a third that appears on δ^{18}O data at 280 mBGS. Some layers are not fully saturated with water such as the Collingwood and Cobourg formations (Raven et al., 2011).

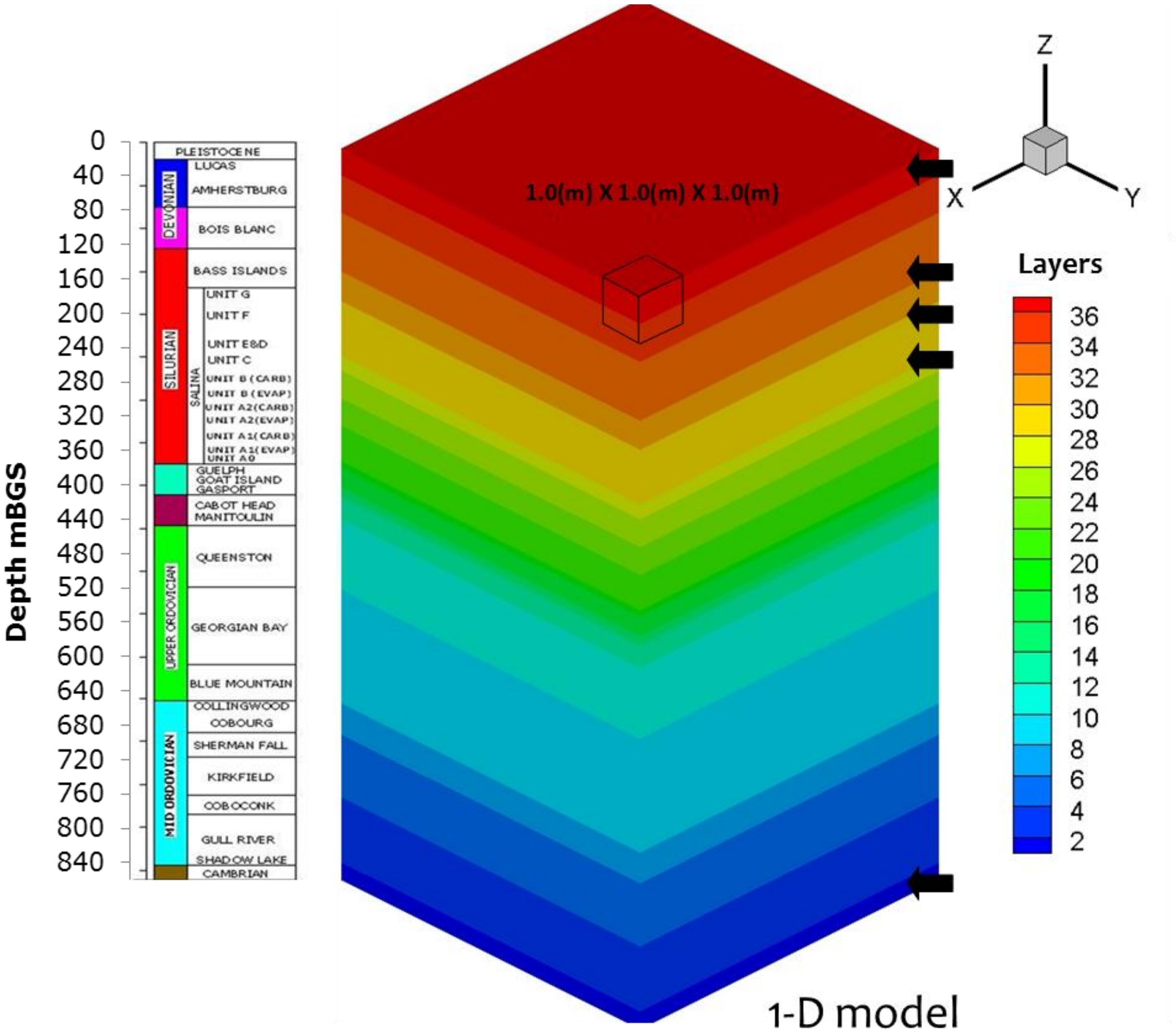

Figure 3.10: The 1-D solute transport model in Z direction with a grid size of 1x1x1 m.

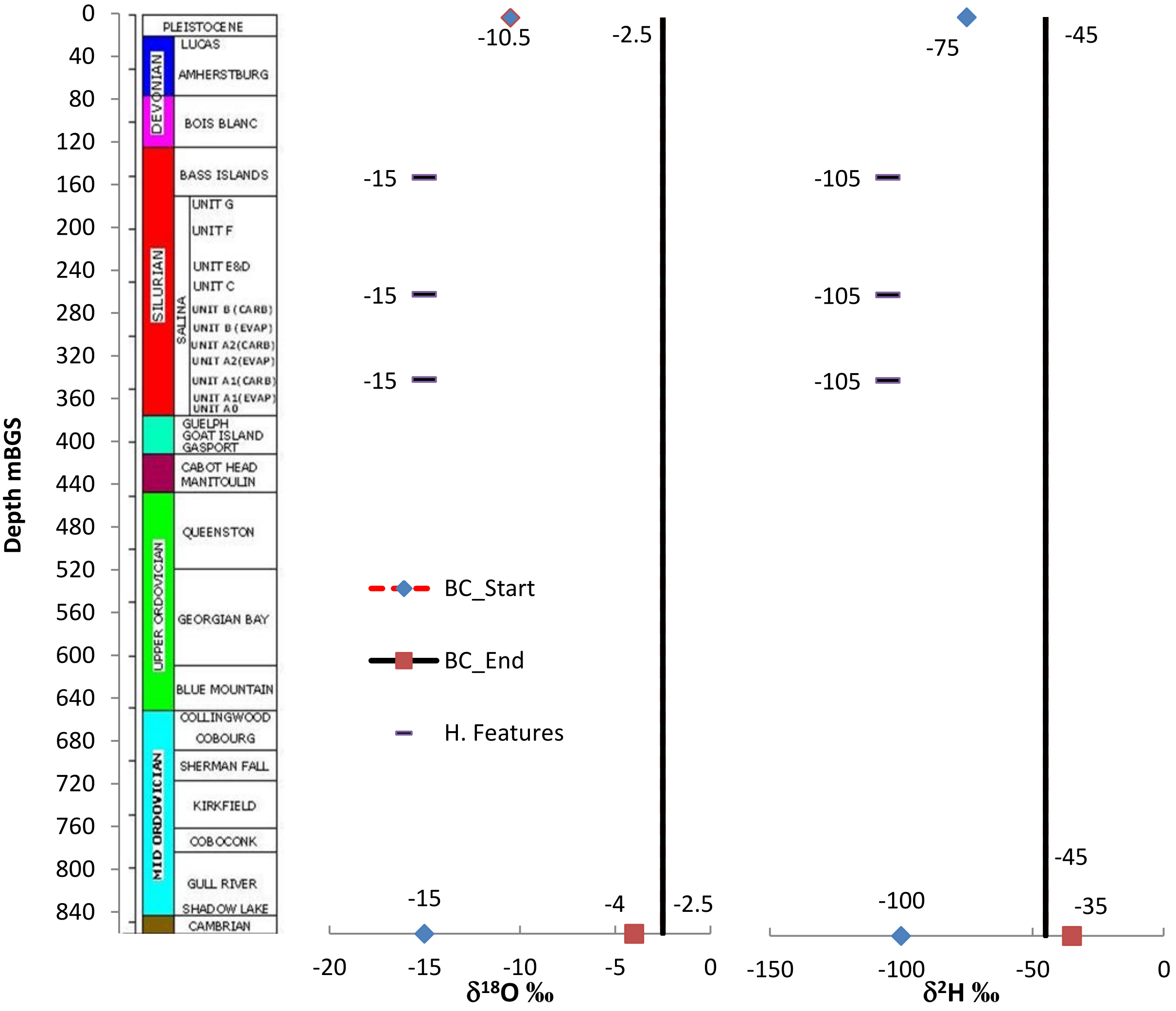

Figure 3.11: Initial and boundary conditions of the 1-D model. The solid line represents the initial conditions. Blue dots represent the first boundary conditions. Red dots represent the final boundary conditions. The black dots represent the boundary conditions for the horizontal features.

3.5.2 Initial and boundary conditions

Porewater in the middle of the domain is characterized by high salinity of about 300 g/L. The source of this brine is evapo-concentrated sea water (Wilson and Long, 1992). The isotopic composition in this kind of water will be enriched. The initial isotopic composition of the domain is set to the values of -2.5‰ for δ^{18}O and -45‰ for δ^{2}H. These initial conditions for δ^{18}O and δ^{2}H represent the highest values measured in the domain that represent more conservative option than using seawater isotope composition.

The upper boundary shows values of isotope composition typical of modern meteoric precipitation. The concentrations of δ^{2}H and δ^{18}O are about -75‰ and -10.5‰ respectively.

Changes in the groundwater characteristics with time, including δ^2H and δ^{18}O composition and TDS must have occurred in the Cambrian aquifer. The concentrations of δ^2H and δ^{18}O are about -100‰ and -15‰ respectively, when extrapolating data points from 400 to 700 mBGS towards the Cambrian aquifer. The trend of the data points then change from 700 to 860 mBGS to about -35‰ and -4‰ at the present time for δ^2H and δ^{18}O, respectively. The latter can be interpreted as enriched old water migrating from deep Michigan basin, while the former can be interpreted as a mixture of depleted water entering through the Cambrian outcrop and mixing out with old resident water. The prevailing condition will depend on the injection pressure of the glacial water against topographic drive from Michigan basin (depending on periods of glaciation). A study by Siegel and Mandle (1984) suggests that glacial meltwater invaded the Cambrian aquifers in North-Central United States during Pleistocene glaciations.

The water pressure in the model domain is characterized by under pressure in the Ordovician shale and limestone formations, and overpressure in the Cambrian aquifer. Assuming constant hydraulic head for the total run time instead of using time serious of head change might result in underestimate or overestimate of the resulting advection flux. To avoid modeling solute transport with transient flow conditions, several modeling scenarios were assumed with different environmental head and concentration boundary conditions. The simulations range at both limits between constant heads taken from site measurements (Figure 3.9) and diffusion dominant solute transport. The evolution time for isotope profiles should fall between the two assumed limits. The assigned heads for the advection-diffusion model were taken from present head measurements at the Bruce site, the heads are equal to 350 m for the Cambrian aquifer (lower boundary), -75 m for the Ordovician formations and 180 m for the upper boundary.

Using the configurations described above, three different modeling scenarios were explored: a) Diffusion dominant solute transport for the whole domain, b) The effect of anomalous pressures (advection term) on the diffusion model, c) The effects of the permeable horizontal features on the previous models as shown in table 3.2.

Table 3-2 Summary of model scenarios at the Bruce site

		$\delta^{18}O$ ‰			**$\delta^{2}H$ ‰**			**Total Hydraulic Head (m)**		
		Initial	**Lower**	**Upper**	**Initial**	**Lower**	**Upper**	**Lower boundary**	**Middle of the domain**	**Upper boundary**
Diffusion dominant	Starting Condition	-2.5	-15	-10.5	-45	-100	-75	-	-	-
	Ending Condition @ 500Ka before present	-	-4	-	-	-35	-			
	Horizontal features	-15 @ 100Ka before present			-105 @ 100Ka before present					
Diffusion + advection	Starting Condition	-2.5	-15	-10.5	-45	-100	-75	350 @ 860 mBGS	-40 @ 760 mBGS	180 @ 0 mBGS
	Ending Condition @ 50Ka before present	-	-4	-	-	-35	-			
	Horizontal features	15 @ 15Ka before present			-105 @ 15Ka before present					

3.6 Results and Discussion

In the first set of simulations, the upper and lower boundaries were fixed at values for $\delta^{18}O$ of -10.5‰ and -15‰ respectively. The initial condition for $\delta^{18}O$ was set at a value of -2.5‰, which represents the maximum value in the domain. For diffusion dominant solute transport simulations, the total head was set to a value of 0 m for the whole domain. For advection & diffusion simulations, the total head was set to the values measured at the site as shown in Figure 3.9. The results of these simulations are shown in Figure 3.12. The best fit for purely diffusion transport occurs at time equal to 50 Ma, while for advection & diffusion transport, best fit occurs at time equal to 2.5 Ma.

In general, both simulations for the first scenario with purely diffusive and advection & diffusion solute transport match the data quite well. This indicates that the chosen configuration with constant parameters for the 38 layers, homogeneous initial conditions for the domain, and constant boundary concentrations at the top and lower boundary is a possible scenario.

For the diffusion case, the model fits the middle part at 30 Ma (Upper Ordovician) and the best fit for the upper layers (Silurian and Devonian) and lower boundary (Mid Ordovician) fits at 50 Ma (Figure 3.12). The advection & diffusion model results matched the measured data for the whole domain at 2.5 Ma. These results show that solute transport at the upper and lower part of the domain cannot be described by pure diffusion model.

Figure 3.13 shows the effects of adding horizontal features to the advection & diffusion model. The activation time for the horizontal features in the Silurian formations is 15 Ka before present. This time falls about the end of the last glacial maximum (LGM) (Peltier, 2011). During this period, isostatic rebound from matrix expansion leads to fracturing and enhanced formation permeability Devonian and Pleistocene formations (Weaver et al., 1995).

Figure 3.14 is showing a comparison between results from advection & diffusion model and pure diffusion model, while adding the effects of horizontal features. The results from the first model match the data quite well especially in the upper and lower part of the domain. These results confirm the hypothesis of advection transport in the lower and upper part of the domain. The activation time of the horizontal features in the Silurian formations is 100 Ka before present in the pure diffusion model.

The results from advection & diffusion model with the horizontal features for $\delta^{2}H$ and $\delta^{18}O$ are shown in Figure 3.15. The model results for both $\delta^{2}H$ and $\delta^{18}O$ is showing a relatively good match with the measured data except for $\delta^{2}H$ at the Mid Ordovician formations. This might be a reason of a more enriched $\delta^{2}H$ as a starting concentration for the lower boundary than the values assumed in the model.

The lower boundary activation time is 50 & 500 Ka for the advection & diffusion model and diffusion model respectively. The pale-hydrogeological history of Cambrian aquifer cannot confirm which scenario is more plausible of the change in concentration in the lower boundary. Although, the advection & diffusion model results match the measured data better than the diffusion model. The overpressured Cambrian aquifer suggests that brine was forced to flow from the depth of the Michigan basin. The brine isotopic composition from the Lower Ordovician in central Michigan is ($\delta^{18}O$ = -1.95‰ and $\delta^{2}H$ = -60‰ VSMOW) and ($\delta^{18}O$ = -1.6‰ and $\delta^{2}H$ = -50‰) from (Graf et al., 1965) and (Dollar, 1988) respectively.

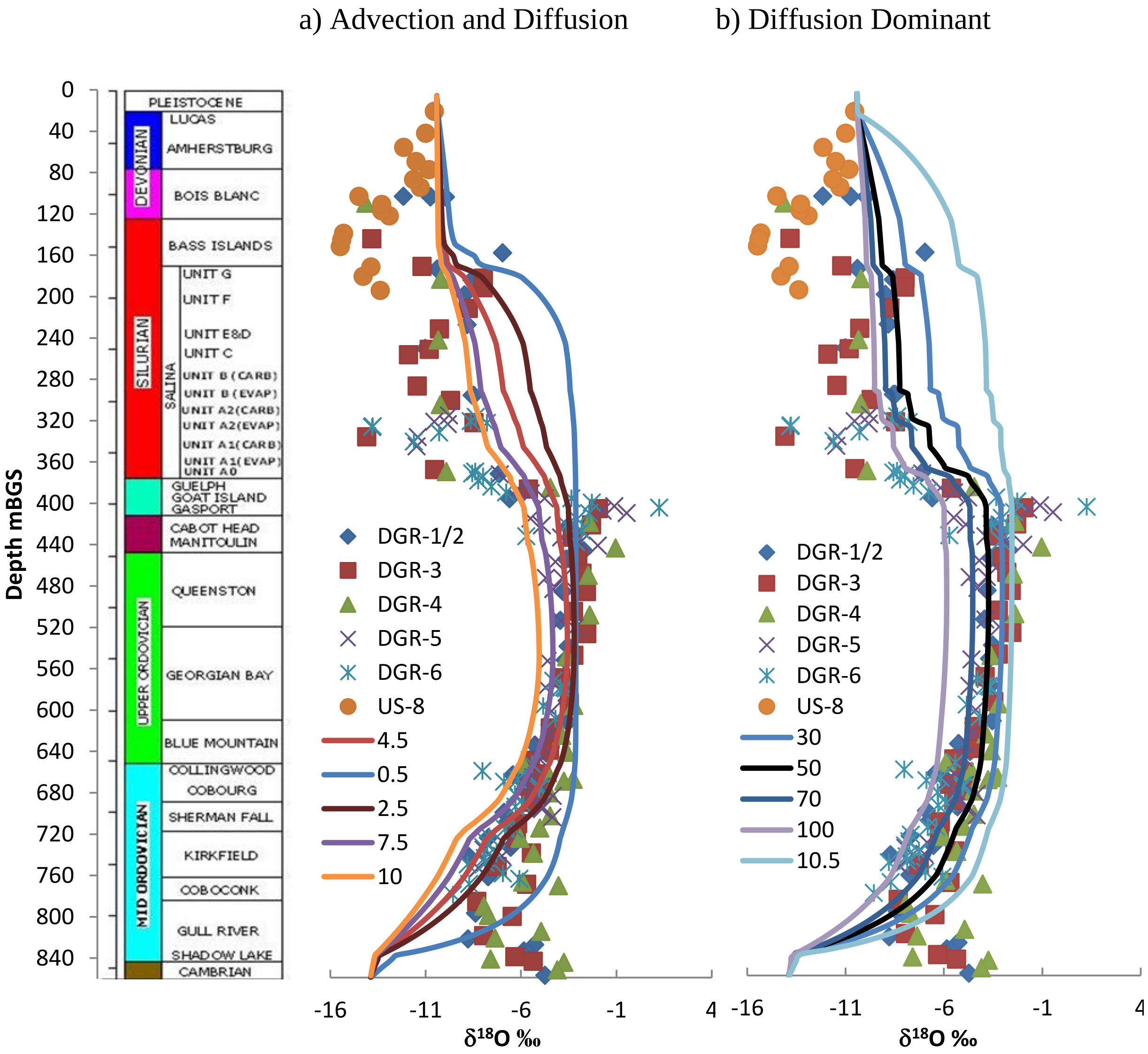

Figure 3.12: Model results superimposed on measured data ($\delta^{18}O$) at DGR1-6 at the Bruce site. a) The results for advection & diffusion model for different simulation run times from 0.5 to 10 Ma. . a) The results for diffusion model for different simulation run times from 10.5 to 100 Ma.

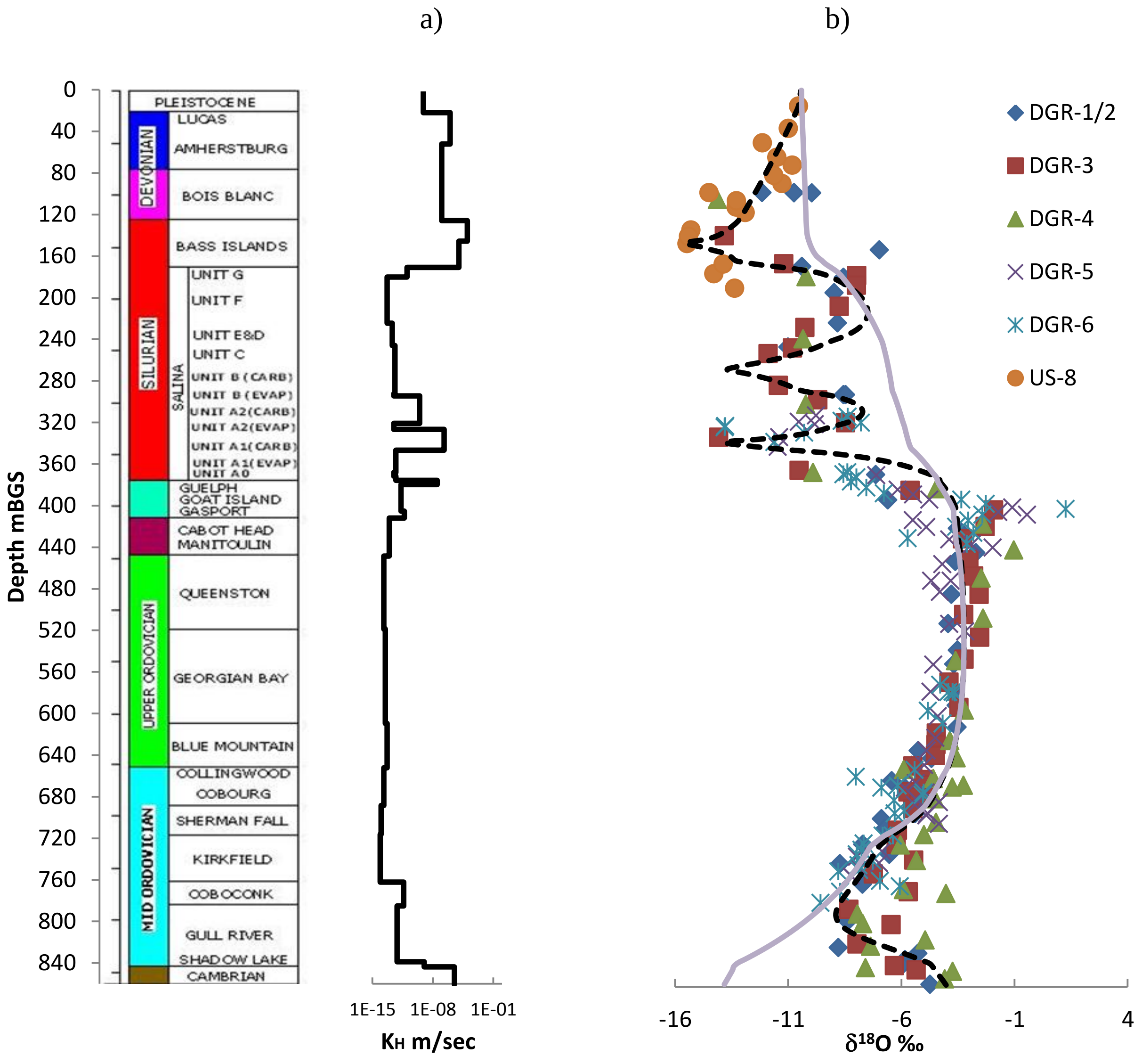

Figure 3.13: a) Horizontal Hyd. Conductivity (m/sec) versus depth (mBGS). b) Diffusion & advection [solid line], diffusion & advection with the effect of horizontal features [dotted line] superimposed over isotopes data. The model evolution time is 2.5 Ma, the horizontal features were activated 15 Ka before present, the concentration at the lower boundary was reversed at 50 ka before present.

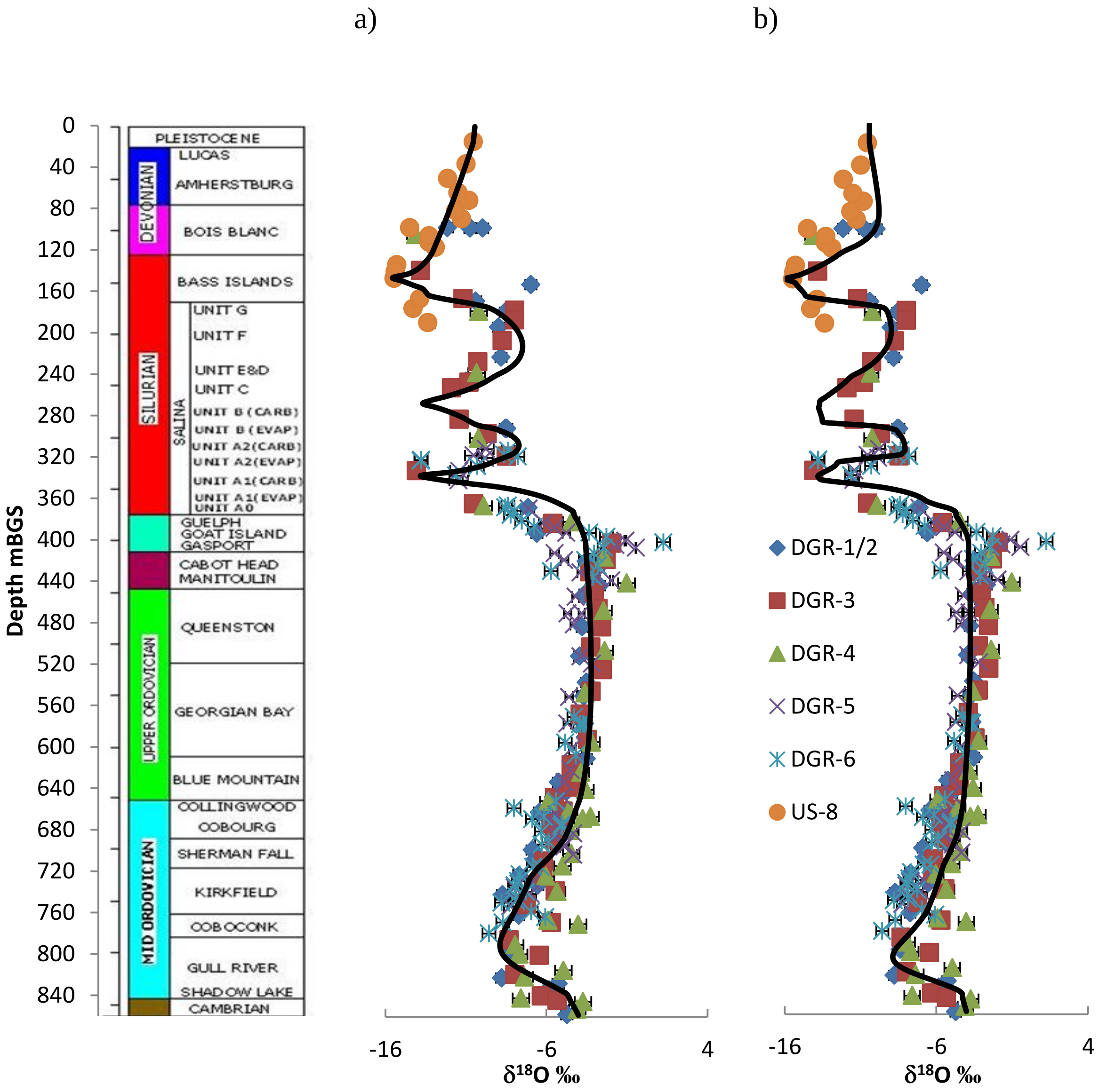

Figure 3.14: Model results superimposed over δ^{18}O data from DGR1-6 and US-8 . Figure a) is the advection-diffusion model, where the model evolution time is 2.5 Ma, the horizontal features were activated 15 Ka before present, the concentration at the lower boundary was reversed at 50 ka before present. a) Diffusion dominant model, the model evolution time is 50 Ma, the horizontal features were activated 100 Ka before present, the concentration at the lower boundary was reversed at 500 ka before present.

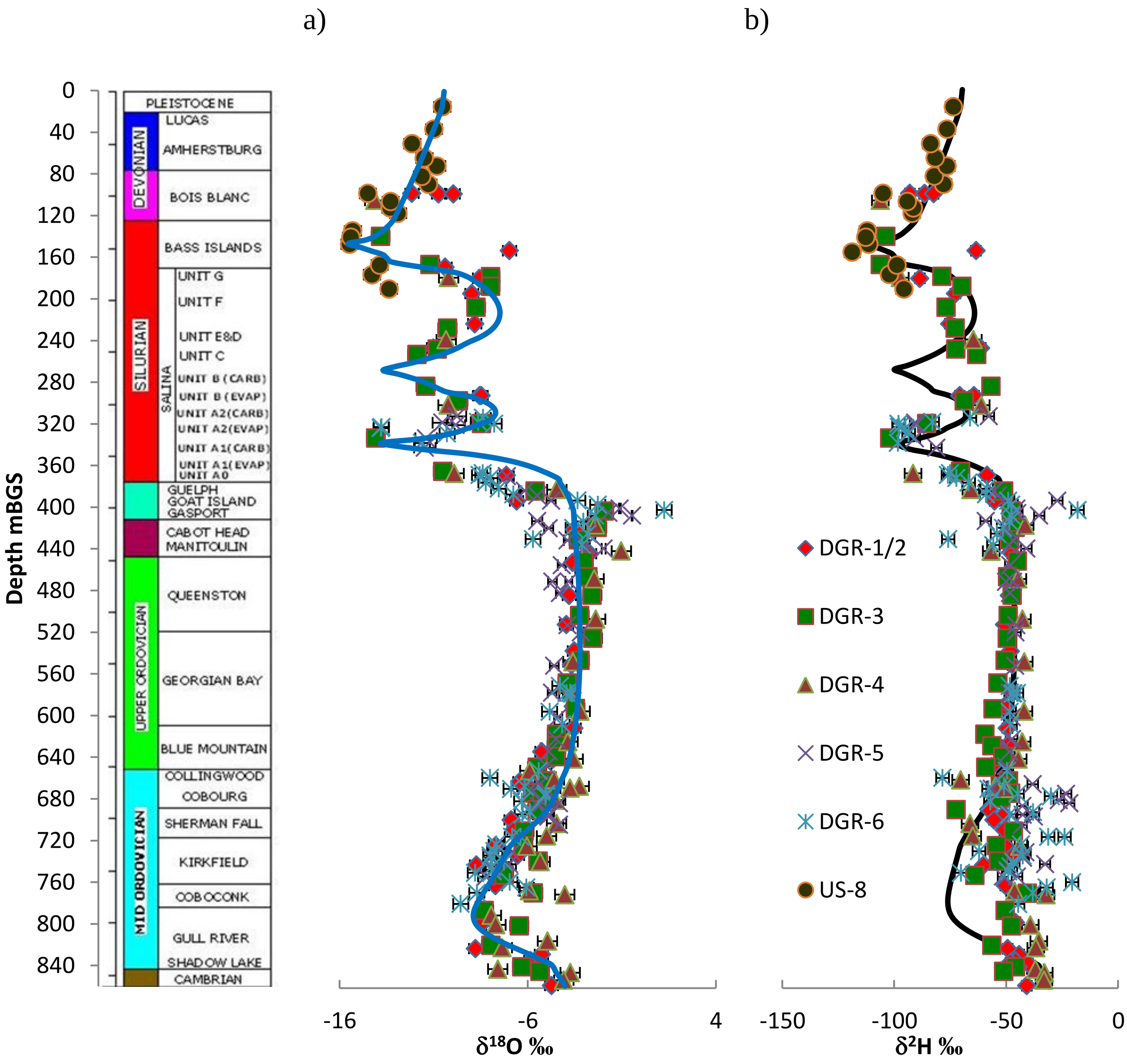

Figure 3.15: Model results of [a) δ^{18}O and b) δ^{2}H] superimposed over data form DGR1-6 and US-8 . The model evolution time is 2.5 Ma, the horizontal features were activated 15 Ka before present, the concentration at the lower boundary was reversed at 50 ka before present.

3.7 Conclusion

The advection term improve the fit of the model results to the measured data of natural isotopes compositions from the Bruce site. The advection term from the upper boundary improve the model fit to a considerable geologically scenarios for glacial water invasion.

The vertical advection term was studied in sedimentary formations introduced for nuclear waste disposal (Gimmi et a., 2007 and Mazurek et al., 2011). They both concluded that advection has a small effect on solute transport at different sites, and can reduce the evolution time by some magnitude. Although, they assumed upward or downward advection for the whole domain, that is not the case at the Bruce site. The underpressure in the middle of the domain will cause both upward and downward advection from the domain. The advection from the upper and lower boundaries in the Bruce case will be added to the effect of diffusion, in the other cases advection effect will be added to diffusion in one boundary and subtracted from the other. Furthermore, the hydraulic gradient measured at the present time reaches 4 m/m in some areas in the domain which is orders of magnitude more than other sites (<0.01 m/m).

The diffusion coefficients and hydraulic conductivities measured on laboratory-scale or field experiments can support long period and formation scale transport modelling. The measured parameters provide evolution times for natural isotopes profiles that is plausible in a pale-geologically sense.

3.8 References

Al, T., Beauheim, R., Crowe, R., Diederichs, M., Frizzell, R., Kennell, L., Lam, T., Parmenter, A. and Semec B. (2011), Geosynthesis. Supporting technical report. NWMO DGR-TR-2011-11-R000.

Altinier, M.V., Savoye, S., Michelot, J.-L., Beaucaire, C., Massault, M., Tessier, D., Waber, H.N., (2007). The isotopic composition of argillaceous-rocks pore water: an intercomparison study on the Tournemire argillite (France). Phys. Chem. Earth 32, 209–218.

Armstrong, D.K. and Carter, T.R., (2006). An updated guide to the subsurface Paleozoic stratigraphy of southern Ontario, Ontario Geological Survey, Open File Report 6191.

Desaulniers, D., J. Cherry, and P. Fritz (1981), Origin, age and movement of pore water in argillaceous quaternary deposits at four sites in southwestern Ontario, J. Hydrol., 50(1– 3), 231–257.

Dollar, P.S. (1988). Geochemistry of Formation Waters, Southwestern Ontario, Canada and Southern Michigan, U.S.A.: Implications for origin and evolution. M.Sc. Thesis. University of Waterloo. Waterloo, Canada.

Gartner Lee Limited, (2008). Phase 1 Regional Geomechanics, Southern Ontario, OPG's Deep Geologic Repository for Low and Intermediate Level Waste, OPG Report # 00216-REP-01300-00008-R00.

Gimmi, T., Waber, H.N., Gautschi A., and A. Rubel (2007), Stable water isotopes in pore water of Jurassic argillaceous rocks as tracers for solute transport over large spatial and temporal scales, Water Resour. Res., 43, W04410, doi:10.1029/2005WR004774.

Graf, D.L., Friedman, I. and Meents, W. (1965). The origin of saline formation waters, II: isotopic fractionation by shale micropore systems. Illinois State Geological Survey. Circular 393.

Hendry, M. J., and L. I. Wassenaar (1999), Implications of the distribution of δD in pore waters for groundwater flow and the timing of geologic events in a thick aquitard system, Water Resour. Res., 35, 1751– 1760.

Hobbs, M.Y., Frape, S.K., Shouakar-Stash, O., Kennel L.R. (2008), Phase I Regional Hydrogeochemistry, Southern Ontario. Supporting technical report. OPG 00216-REP-01300-00006-R00.

Kharaka Y. K. and Hanor, J. S. (2005). Deep fluids in the Continents: 1. Sedimentary Basins. In: Treatise on Geochemistry, Vol. 5, Surface and groundwater, weathering, and soils. J. I. Drever, (ed.), 499-540.

Mazurek, M., Alt-Epping, P., Bath, A., Gimmi, T., H., Waber, N., Buschaert, S., De Cannière, P., De Craen, M., Gautschi, A. and Savoye, S. (2011), Natural tracer profiles across argillaceous formations, Appl Geoch, 26(7), 1035.

Patriarche, D., E. Ledoux, J.-L. Michelot, R. Simon-Coinc¸on, and S. Savoye (2004a), Diffusion as the main process for mass transport in very low water content argillites: 2. Fluid flow and mass transport modeling,Water Resour. Res., 40,W01517, doi:10.1029/2003WR002700.

Patriarche, D., J.-L. Michelot, E. Ledoux, and S. Savoye (2004b), Diffusion as the main process for mass transport in very low water content argillites: 1. Chloride as a natural tracer for mass transport—Diffusion coefficient and concentration measurements in interstitial water, Water Resour. Res., 40, W01516, doi:10.1029/2003WR002600.

Peltier, W.R. (2011). Long-Term Climate Change. Supporting technical report. NWMO DGR-TR-2011-14-R000

Raven, K., McCreath, D., R. Jackson, Clark, I., Heagle, D., Sterling, S. and Melaney, M., (2011), Descriptive Geosphere Site Model. Supporting technical report. NWMO DGR-TR-2011-24- R000.

Remenda, V. H., G. van der Kamp, and J. A. Cherry (1996), Use of vertical profiles of d18O to constrain estimates of hydraulic conductivity in a thick, unfractured aquitard, Water Resour. Res., 32(10), 2979– 2987.

Rübel, A., C. Sonntag, J. Lippmann, A. Gautschi, and F. J. Pearson (2002), Solute transport in formations of very low permeability: Profiles of stable isotope and dissolved gas contents of the pore water in the Opalinus Clay, Mont Terri, Switzerland, Geochim. Cosmochim. Acta, 66, 1311– 1321.

Savoye, S., Michelot, J.L., Bensenouci, F., Matray, J.M., and Cabrera, J. (2008), Transfers through argillaceous rocks over large space and time scales: Insights given by water stable isotopes, Physics and Chemistry of the Earth 33, S67–S74.

Shouakar-Stash, O. (2008). Evaluation of stable chlorine and bromine isotopes in sedimentary formation fluids. Unpublished Ph.D. thesis, University of Waterloo, Waterloo, Ontario, Canada, 332p.

Siegel, D.I., Mandle, R.J. (1984). Isotopic evidence for glacial meltwater recharge to the Cambrian-Ordovician aquifer, north-central United States, Quaternary Research, Volume 22, Issue 3, Pages 328-335, ISSN 0033-5894, 10.1016/0033-5894(84)90026-7.

Sykes, J.F., Normani, S.D. and Yin, Y. (2011). Hydrogeologic Modelling. Supporting technical report. NWMO DGR-TR-2011-16-R000

Therrien, R., McLaren, R.G., Sudicky, E.A., and Panday, S.M. (2008), HydroGeoSphere A Three-dimensional Numerical Model Describing Fully-integrated Subsurface and Surface Flow and Solute Transport. Software Manual.

Vugrinovich R. (1986) Patterns of Regional Subsurface Fluid Movement in the Michigan Basin. Michigan Geological Survey Division, Open File Report, OFR 86-6. Lansing, Michigan.

Weaver, T. R., Frape, S. K. and Cherry J. A. (1995). Recent cross-formational fluid flow and mixing in the shallow Michigan Basin Geological Society of America Bulletin, v. 107, p. 697-707, doi:10.1130/0016-7606(1995)107<0697:RCFFFA>2.3.CO;2 .

WILSON, T. P. and LONG, D.T. (1993). Geochemistry and isotope chemistry of Michigan Basin brines: Devonian formations. Applied Geochemistry, Vol. 8, pp. 81-100.

THIS PAGE HAS BEEN LEFT BLANK INTENTIONALLY

4 3-D Analytical Model for Diffusion Dominant Solute Transport:

Goltz and Roberts (1987) incorporated solute diffusion within immobile regions into the three dimensional advection/dispersion solute transport equation, for an instantaneous point source in an infinite medium. A modified form of Aris's method of moments is developed. The method permitted the calculation of the spatial and temporal moments of solute distributions simulated using the 3D diffusion models, without having to invert the Laplace or Fourier transformed solutions.

Leij et al. (1993) presented analytical solutions for three-dimensional solute transport in a semi-infinite domain. The general equation was solved by Laplace transform in semi-infinite parameters and double Fourier transform in infinite parameters.

Park and Baik (2008) solved the advection-diffusion equation analytically in air for a finite area source using the superposition method. The solution started with a point source described by Dirac Delta function releasing a passive scalar of pollutants. The general equation includes advection along-wind and diffusion terms in crosswind, and vertical directions. The analytical solution was obtained by integrating the solution for the point source in the along-wind and crosswind directions. In this study the solution will be extended into 3-D with no advection term.

The purposes of the developed analytical models are to be used for screening calculations, and modeling grid development for numerical models.

4.1 3-D analytical solution for solute transport diffusion-limited in an infinite solid rock

This section presents several analytical solutions for three dimensional diffusion limited solute transports in an infinite solid rock domain. The domain is considered to be of low permeability where advection term can be neglected. Several solutions are presented in Appendix (I) for different sources shapes. The source is modified from an instantaneous point source into a 3-D box shape with defined X, Y and Z dimensions and a defined time of application. The solutions are used to calculate solute concentrations in homogenous isotropic media at any spatial location in the domain. The concentration species are considered conservative, in case of non-conservative species D_{xi}=D/R, where R is the retardation factor.

More analytical models will be derived in the future work to simulate natural tracers in a finite domain.

4.2 The governing equation

The partial differential equation for solute transport in a homogeneous isotropic medium with 3-D diffusion in (X, Y, Z) directions, with an instantaneous point source, is given by (e.g., Bear 1979):

$$\theta\frac{\partial C}{\partial t} - \theta D_X\frac{\partial^2 C}{\partial X^2} - \theta D_Y\frac{\partial^2 C}{\partial Y^2} - \theta D_Z\frac{\partial^2 C}{\partial Z^2} = M\delta(t-t')\delta(X-X')\delta(Y-Y')\delta(Z-Z') \tag{4.1}$$

$$t > 0, \qquad -\infty < X < +\infty, \qquad -\infty < Y < +\infty, \qquad -\infty < Z < +\infty$$

Where C (M/L^3) is the pore water concentration, θ is the Porosity, D_X, D_Y and D_Z (L^2/T) are pore water diffusion coefficients in the X, Y and Z direction respectively, M (Kg) is the mass of solute injected, $\delta()$ is the Dirac delta function, X, Y and Z (L) are the spatial coordinates of the target point and X', Y' and Z' (L) are the spatial coordinates of the source point. As a result of the infinite medium and the nature of the solute application, this is not an easy solution to derive.

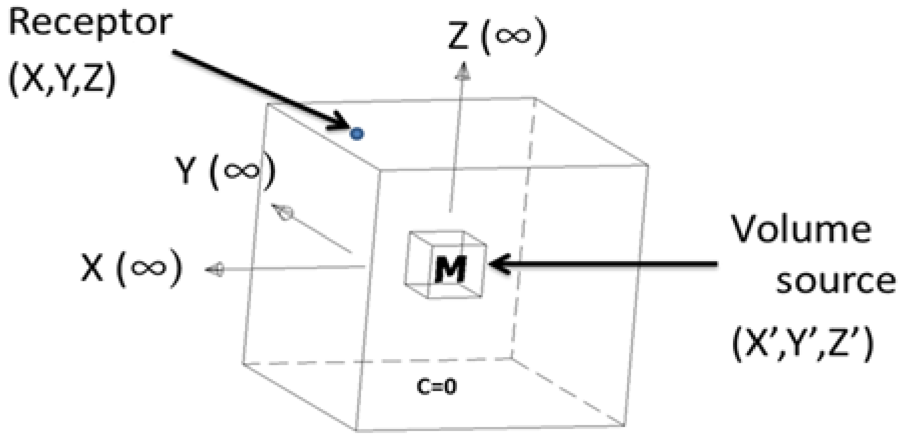

Figure 4.1: The conceptual model of a repository in a 3-D infinite domain

4.3 Problem description

The domain is an infinite three dimensional homogenous and isotropic medium as shown in figure 4.1, with a very low hydraulic conductivity. An instantaneous point source is located at a point within the domain with spatial coordinates X', Y', Z', and time = t'.

The initial condition is given as

$$\mathrm{C}(\mathrm{X},\mathrm{Y},\mathrm{Z},0)=0 \tag{4.2}$$

First type (Dirichlet) Boundary conditions are taken as

$$\mathrm{C}(\pm\infty,\mathrm{Y},\mathrm{Z},\mathrm{t})=0 \tag{4.3}$$

$$\mathrm{C}(\mathrm{X},\pm\infty,\mathrm{Z},\mathrm{t})=0 \tag{4.4}$$

$$\mathrm{C}(\mathrm{X},\mathrm{Y},\pm\infty,\mathrm{t})=0 \tag{4.5}$$

The solutin of the governing equation (3.1), subjected to the initial and boundary conditions, was obtained by applying exponential Fourier transforms with respect to X, Y and Z and the Laplace transform with respect to t (see Appendix I for details). The final result is shown below.

$$\mathrm{C}(\mathrm{X},\mathrm{Y},\mathrm{Z},\mathrm{t})=\frac{\mathrm{M}}{8\theta\pi^{3/2}\sqrt{\mathrm{D_X D_Y D_Z}}(\mathrm{t}-\mathrm{t}')^{3/2}}\exp[\frac{-(\mathrm{X}-\mathrm{X}')^2}{4\mathrm{D_X}(\mathrm{t}-\mathrm{t}')}]\exp[\frac{-(\mathrm{Y}-\mathrm{Y}')^2}{4\mathrm{D_Y}(\mathrm{t}-\mathrm{t}')}]\exp[\frac{-(\mathrm{Z}-\mathrm{Z}')^2}{4\mathrm{D_Z}(\mathrm{t}-\mathrm{t}')}] \tag{4.6}$$

The solution calculates concentrations at a spatial point with coordinates of X, Y and Z with a point source located at X', Y' and Z'.

In order to extend the point source into a volume source, the source is extended in X from X_1' to X_2' and in Y from Y_1' to Y_2' and in Z from Z_1' to Z_2'. Equation (3.6) was integrated with respect to X', Y' and Z', and integrated with respect to t' to extend the solution in time from an instantaneous source to a time step starting from 0 to t_1. The integration is shown in details in Appendix I.

$$\int_{\mathrm{Z}_1'}^{\mathrm{Z}_2'}\int_{\mathrm{Y}_1'}^{\mathrm{Y}_2'}\int_{\mathrm{X}_1'}^{\mathrm{X}_2'}\int_0^{\mathrm{t}_1}\mathbf{C}\,\mathbf{dt}'\,\mathbf{dX}'\,\mathbf{dY}'\,\mathbf{dZ}'= \tag{4.7}$$

$$\int_{\mathrm{Z}_1'}^{\mathrm{Z}_2'}\int_{\mathrm{Y}_1'}^{\mathrm{Y}_2'}\int_{\mathrm{X}_1'}^{\mathrm{X}_2'}\int_0^{\mathrm{t}_1}\frac{\mathbf{M}}{\mathbf{8\theta\pi^{3/2}\sqrt{D_XD_YD_Z}(t-t')^{3/2}}}\exp\left[\frac{-(\mathbf{X}-\mathbf{X}')^2}{\mathbf{4D_X(t-t')}}\right]\exp\left[\frac{-(\mathbf{Y}-\mathbf{Y}')^2}{\mathbf{4D_Y(t-t')}}\right]\exp\left[\frac{-(\mathbf{Z}-\mathbf{Z}')^2}{\mathbf{4D_Z(t-t')}}\right]\mathbf{dt}'\,\mathbf{dX}'\,\mathbf{dY}'\,\mathbf{dZ}'$$

Table 4-1 Various solutions of the integration [equation 4.7]

Source Type	**Equation**
a- Point Source	$\mathrm{C} = \frac{\mathrm{a}}{\sqrt{\mathrm{b}}}[\mathrm{erf}\left(\frac{\sqrt{\mathrm{b}}}{\sqrt{(\mathrm{t}-\mathrm{t}_1)}}\right) - \mathrm{erf}\left(\frac{\sqrt{\mathrm{b}}}{\sqrt{\mathrm{t}}}\right)]$
b- Line Source in the X-direction	$\mathrm{C} = \frac{2\mathrm{a}}{(\gamma_2-\gamma_1)}[\sqrt{\mathrm{b_x}}\,\mathrm{erf}\left(\frac{\sqrt{\mathrm{b_x}}}{\sqrt{\mathrm{T}}}\right) + \sqrt{\frac{\mathrm{T}}{\pi}}\exp\left(\frac{-\mathrm{b_x}}{\mathrm{T}}\right)]$
c- Area Source in the X-Y Plane	$\mathrm{C} = \frac{\mathrm{a}}{(\beta_2-\beta_1)(\gamma_2-\gamma_1)}[\mathrm{b_{xy}}^{1.5}\,\mathrm{erf}\left(\frac{\sqrt{\mathrm{b_{xy}}}}{\sqrt{\mathrm{T}}}\right) + \frac{4}{3}\sqrt{\frac{\mathrm{T}}{\pi}}\exp\left(\frac{-\mathrm{b_{xy}}}{\mathrm{T}}\right)(\mathrm{b_{xy}}+\mathrm{T}) - \frac{2}{\sqrt{\pi}}\mathrm{T}^{1.5}\exp\left(\frac{-\mathrm{b_{xy}}}{\mathrm{T}}\right)]$
d- Finite Volume Source	$\mathrm{C} = \frac{\mathrm{a}}{(\tau_2-\tau_1)(\beta_2-\beta_1)(\gamma_2-\gamma_1)}[\frac{8}{15\sqrt{\pi}}\exp\left(\frac{-\mathrm{b_{xyz}}}{\mathrm{T}}\right)\{\sqrt{\pi}\,(\mathrm{b_{xyz}})^{2.5}\exp\left(\frac{\mathrm{b_{xyz}}}{\mathrm{T}}\right)\mathrm{erf}\left(\frac{\sqrt{\mathrm{b_{xyz}}}}{\sqrt{\mathrm{T}}}\right) + (\mathrm{b_{xyz}})^2\sqrt{\mathrm{T}} + 2\mathrm{b_{xyz}}\mathrm{T}^{1.5} + 2\mathrm{T}^{2.5}\} + \frac{4}{3\sqrt{\pi}}\mathrm{T}^{1.5}\exp\left(\frac{-\mathrm{b_{xyz}}}{\mathrm{T}}\right)(\mathrm{b_{xyz}}+2\mathrm{T}) - \frac{2}{\sqrt{\pi}}\mathrm{T}^{2.5}\exp\left(\frac{-\mathrm{b_{xyz}}}{\mathrm{T}}\right)]$

Where $(\tau_2-\tau_1)(\beta_2-\beta_1)(\gamma_2-\gamma_1) \neq 0 \;\; \forall\, \mathrm{X,Y,Z}$

$$a = \frac{M}{8\theta\pi\sqrt{D_X D_Y D_Z}t_1}$$

$$\gamma_1 = \frac{(X-X_1')^2}{4D_X}, \gamma_2 = \frac{(X-X_2')^2}{4D_X}$$

$$\beta_1 = \frac{(Y-Y_1')^2}{4D_Y}, \beta_2 = \frac{(Y-Y_2')^2}{4D_Y}$$

$$\tau_1 = \frac{(Z-Z_1')^2}{4D_Z}, \tau_2 = \frac{(Z-Z_2')^2}{4D_Z}$$

$$\mathrm{b} = \frac{(X - X')^2}{4D_X} + \frac{(Y - Y')^2}{4D_Y} + \frac{(Z - Z')^2}{4D_Z}$$

$$\mathrm{b_x} = \mathrm{\gamma_i} + \frac{(Y - Y')^2}{4D_Y} + \frac{(Z - Z')^2}{4D_Z}$$

$$\mathrm{b_{xy}} = \mathrm{\gamma_i} + \beta_j + \frac{(Z - Z')^2}{4D_Z}$$

$$\mathrm{b_{xyz}} = \mathrm{\gamma_i} + \beta_j + \tau_l$$

$T = t-t_i$

To verify the analytical solutions, they were compared with a numerical approach using HydroGeoSphere (HGS). The parameters, e.g., diffusion coefficient, porosity, pollutant mass and run time, were identical in both the solutions and the numerical model. A variety of grid discretizations were investigated in the numerical model HGS to reduce errors. A small domain was used with an average distance of 2 m between the source and receptor, in order to refine the mesh in HGS and reduce numerical errors. The two solutions give a good match in results with small differences, i.e., the mean error is less than 3% that are likely related to numerical approximations (see Figure 4.2 for examples of the fits between the analytical and numerical solutions). Also the response of the analytical solution to small changes in source dimension is more visible than with the numerical model. Examples of the comparisons are shown in table 4.2.

Table 4-2 The input data for the cases in table 4.1

Parameters	**Units**	**Inst.Point Source Values**	**1-Point Source Values**	**2-Line Source Values**	**3-Area Source Values**	**4-Volume Source Values**
X	m	2.0	2.0	2.0	2.0	2.0
Y	m	2.0	2.0	2.0	2.0	2.0
Z	m	2.0	2.0	2.0	2.0	2.0
M	Kg	10.0	10.0	10.0	10.0	10.0
Porosity		0.13	0.13	0.13	0.13	0.13
$\mathbf{D_x}$	m^2/sec	$1.0x10^{-10}$	$1.0x10^{-10}$	$1.0x10^{-10}$	$1.0x10^{-10}$	$1.0x10^{-10}$
$\mathbf{D_y}$	m^2/sec	$1.0x10^{-10}$	$1.0x10^{-10}$	$1.0x10^{-10}$	$1.0x10^{-10}$	$1.0x10^{-10}$
$\mathbf{D_z}$	m^2/sec	$1.0x10^{-10}$	$1.0x10^{-10}$	$1.0x10^{-10}$	$1.0x10^{-10}$	$1.0x10^{-10}$
X'	m	0.0	0.0	N/A	N/A	N/A
Y'	m	0.0	0.0	0.0	N/A	N/A
Z'	m	0.0	0.0	0.0	0.0	N/A
$\mathbf{X_1}$	m	N/A	N/A	-0.5	-0.5	-0.5
$\mathbf{X_2}$	m	N/A	N/A	0.5	0.5	0.5
$\mathbf{Y_1}$	m	N/A	N/A	N/A	-0.5	-0.5
$\mathbf{Y_2}$	m	N/A	N/A	N/A	0.5	0.5
$\mathbf{Z_1}$	m	N/A	N/A	N/A	N/A	-0.5
$\mathbf{Z_2}$	m	N/A	N/A	N/A	N/A	0.5
t'	Yrs	0.0	N/A	N/A	N/A	N/A
$\mathbf{t_1}$	Yrs	N/A	10.0	10.0	10.0	10.0

4.4 Output for analytical and numerical solutions

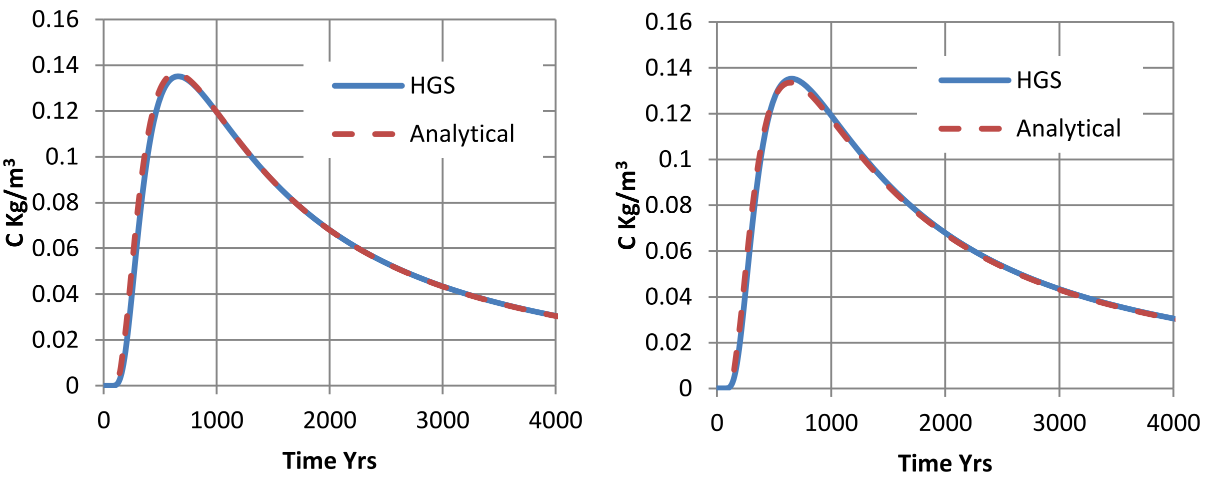

(a) Point Source

(b) Line Source

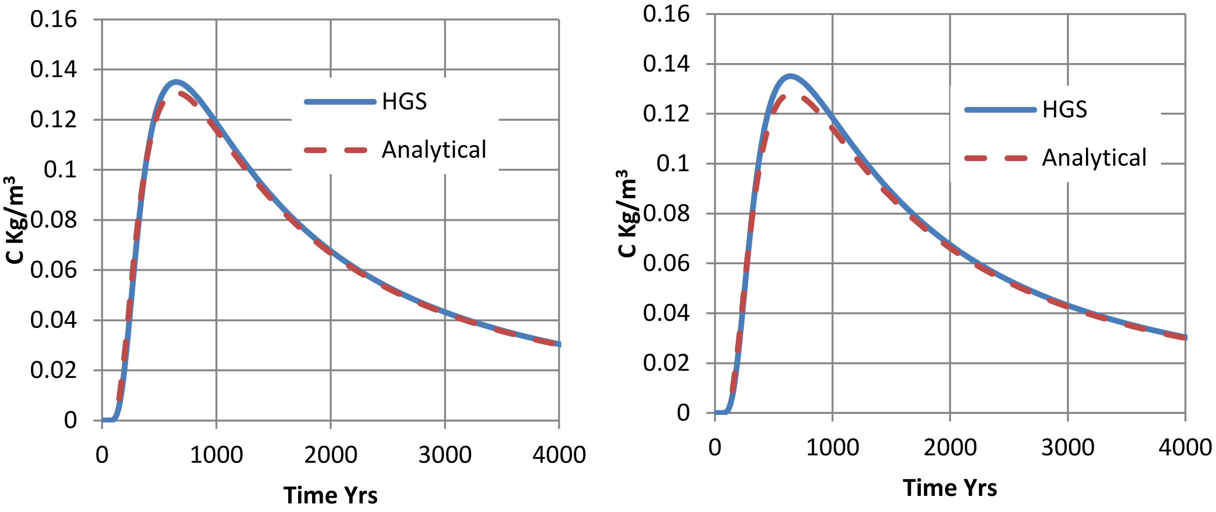

(c) Area Source

(d) Volume Source

Figure 4.2: HGS results VS Analytical solutions for the four source cases

As an example of the application of the analytical model, grid discretization, time step, time weighting and boundary effects for the HydroGeoSphere (HGS) model will be investigated in a sensitivity analysis. The objective is to reduce the numerical modeling error generated by these variables on the transport solution.

The analytical solution developed in above is coded in FORTRAN as shown in Appendix II. The results from the analytical solution are compared with HGS results under a variety of conditions. The mean errors between the two solutions are calculated using equation given below. The parameters in the numerical model were optimized to reduce computational errors.

$$\mathrm{Error} = \frac{1}{N}\sum_{1}^{N} \frac{\mathrm{abs}|C_{\mathrm{Anal}} - C_{\mathrm{model}}|}{C_{\mathrm{Anal}}} \tag{4.8}$$

The numerical model was built for a solid rock domain having low permeability and low porosity. The transport is considered diffusion-limited where the advection/dispersion term is neglected. Fixed values of the pore diffusion coefficient (1.0 X 10^{-10} m^2/s) and Porosity (13%) were used in simulations. These values were chosen to approximate Benken site, north of Switzerland, conditions.

The numerical model domain 300 X 300 X 300 m was divided into 3 sections as shown in figure (4.3a). The middle part is refined with different grid spacing while the outer part includes a coarse grid to remove boundary effects and reduce computational time as shown in table 3.3. Figure 3.3b shows the concentration distribution by the end of simulation for run number 4 of 4 X 4 X 4 m grid spacing for the middle section.

Table 4-3 The grid spacing in X, Y and Z for the domain three sections

Run's Number	First 100m	Middle 100 m	Last 100 m
1	10 m	0.5 m	10 m
2	10 m	1.0m	10 m
3	10 m	2.0 m	10 m
4	10 m	4.0 m	10 m
5	10 m	8.0 m	10 m
6	12 m	12 m	12 m

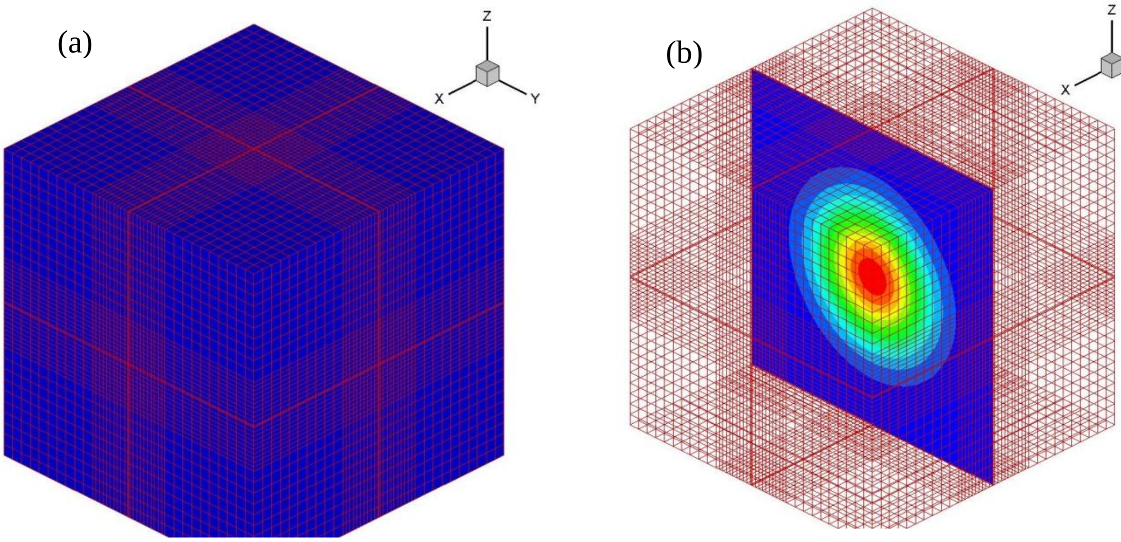

Figure 4.3: An illustration of the discretization and concentration distribution in cross section for one of the test cases.

The results of the initial grid discretization for the uniform grid case are shown in figure (4.4). The results show a fixed percentage of mean error with the increase in grid spacing until a specific point. Beyond this point the error increases dramatically. This point is considered the optimum grid spacing where the error is minimized, and the number of nodes is low which helps reduce simulation run time.

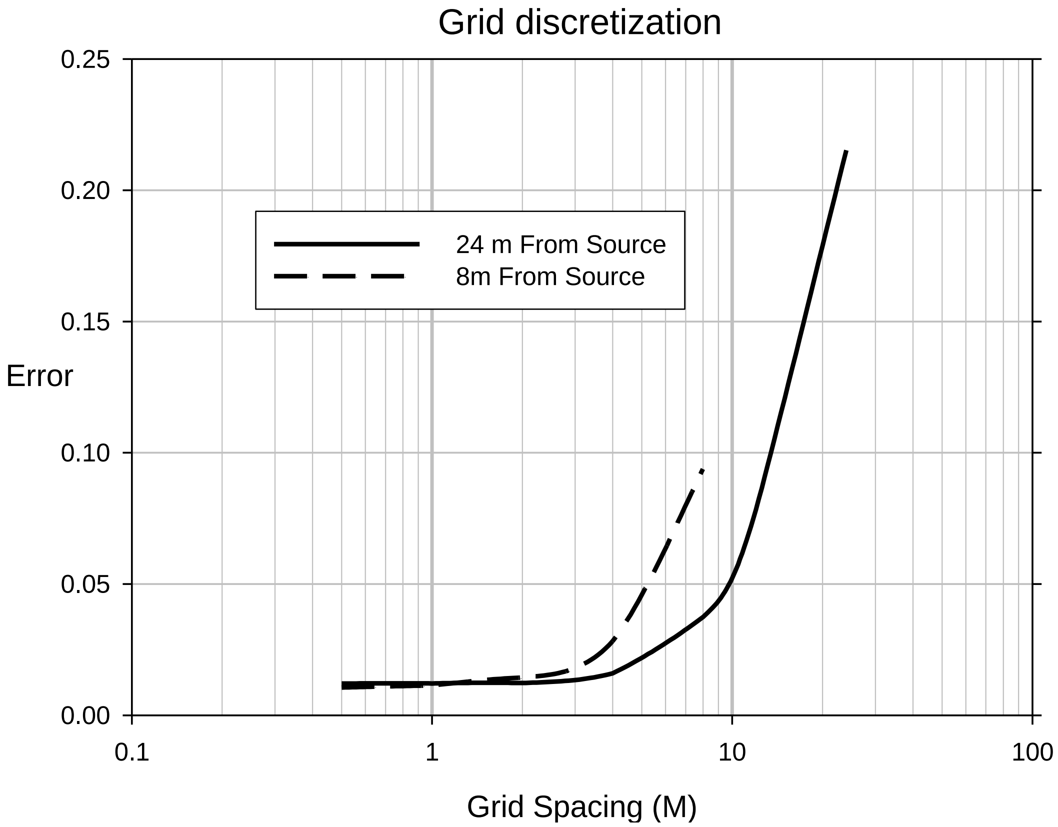

Figure 4.4: Errors corresponding to different grid spacing

4.5 **References**

Goltz, M.N., and Roberts, P.V. (1987), Using the Method of Moments to Analyze Three-Dimensional Diffusion-Limited Solute Transport From Temporal and Spatial Perspectives, Water Resources Research, VOL. 23, NO. 8, PAGES 1575-1585.

Leij, F.J., Toride, N., and Genuchten M.T. (1993), Analytical solutions for non-equilibrium solute transport in three-dimensional porous media, Journal of Hydrology, 151 (1993) 193-228.

Park, Y.S., and Baik, J.J. (2008), Analytical solution of the advection-diffusion equation for a ground-level finite area source, Atmospheric Environment 42 (2008) 9063–9069.

THIS PAGE HAS BEEN LEFT BLANK INTENTIONALLY

5 General Conclusions and Recommendations

The developed results from the 2-D hydro-mechanical model of the Michigan basin present a preliminary view of the effects of glacial events on the development of abnormal pressure heads within the basin formations. The time serious of heads developed from cycles of loading and unloading is used to study solute transport history within the basin. Also gives a better understanding of the regional groundwater systems. This is considered a crucial matter to understand the future respond of the deep geological repository (DGR) under similar future circumstances. A 1-D solute transport model that was built to simulate the history of water isotopes (^{18}O and ^{2}H) at the Bruce site confirms the previous statement. The model was built on the current measured heads, and the results show the importance of including the effects of advection term resulting from anomalous heads to the diffusion term.

The hydromechanical model was built first in 1-D. The output of the 1-D model gave a clear view of the importance of the Cambrian layer as a lower boundary in the development of the significant underpressure in the rock formations. The model was then upgraded to a 2-D model that cuts the Michigan basin from the NE to the SW direction. The developed results of the 2-D model were verified with the measured heads at the Bruce site. The results deliver a reasonable understanding of the history of flow system, and incorporate the importance of the formations outcrops and orientations. The main underpressure in the rock formation was captured by the 2-D model, but some other anomalous pressures in the domain need further study to detect the reasons for its formation.

Upgrading the hydromechanical model from 2-D to 3-D and testing the importance of incorporating several other factors to the model is needed in the future work. The factors needed to be investigated are the importance of density driven flow, permafrost, presence of a gas phase, lithosphere flexure, faults, fractures and the side boundaries of the Michigan basin. The integration of the hydromechanical model with the solute transport model will give a clear view of future solute transport and groundwater flow systems at the Michigan basin and especially at the Bruce site.

THIS PAGE HAS BEEN LEFT BLANK INTENTIONALLY

6 Appendix I

The SIGMA/W model was compared with HydroGeoSphere (HGS), the governing equation developed by [13]

$$\frac{\partial}{\partial X_i}\left(K_{ij}\frac{\partial h}{\partial X_j}\right) = S_S\frac{\partial h}{\partial t} + \xi S_S\frac{1}{\rho g}\frac{\partial \sigma_{ZZ}}{\partial t} \pm Q$$

Where σ_{ZZ} is the vertical total stress [M T-2 L-1], Ss is the modified one-dimensional specific storage [L-1], K_{ij} is the hydraulic conductivity tensor [L T-1], g is the gravitational acceleration [L T-2], ρ is the density of water [M L-3], Q fluid exchange with the outside of the simulation domain[L3 L-3 T-1], and ξ is the one-dimensional loading efficiency [dimensionless].

1-D models of single material of 500m length and 50m of width were built with the same characteristics in both HGS and SIGMA/W. Material properties are shown in table (7.1). The mesh was divided to 5mX5m rectangular elements as shown in figure (7.1.a). The domain was assumed to be fully saturated in the first two simulations. While in the third simulation unsaturated zones were allowed in SIGMA/W, where the model will consider consolidation in those soils where there are negative pore-water pressures.

The initial hydraulic conditions were set to be in hydrostatic. The hydraulic boundary conditions were set to constant specific head at the top and lower boundary. For stress, both the left and the right side of the domain were prevented from movement in horizontal direction and free to move in vertical direction. The lower boundary were prevented from movement in both horizontal and vertical directions. The upper boundary was set to be free in both directions, and different mechanical loading scenarios were applied as shown in figure (7.1.a).

Three different loading scenarios were applied on the domain. In the first scenario, the load was increased gradually with time to a certain value and then remains constant until the end of the simulation figure (7.1.b). The load was decreased in the second loading scenario from a value of 25000 Kpa back to zero in order to generate negative pressure in the domain figure (7.1.c). In the third scenario one half of the top boundary was loaded with the second loading scenario figure (7.1.d).

The results of the first two scenarios show a good match between the output of both HGS and SIGMA/W. For the third scenario, the result starts to deviate especially in the negative heads part.

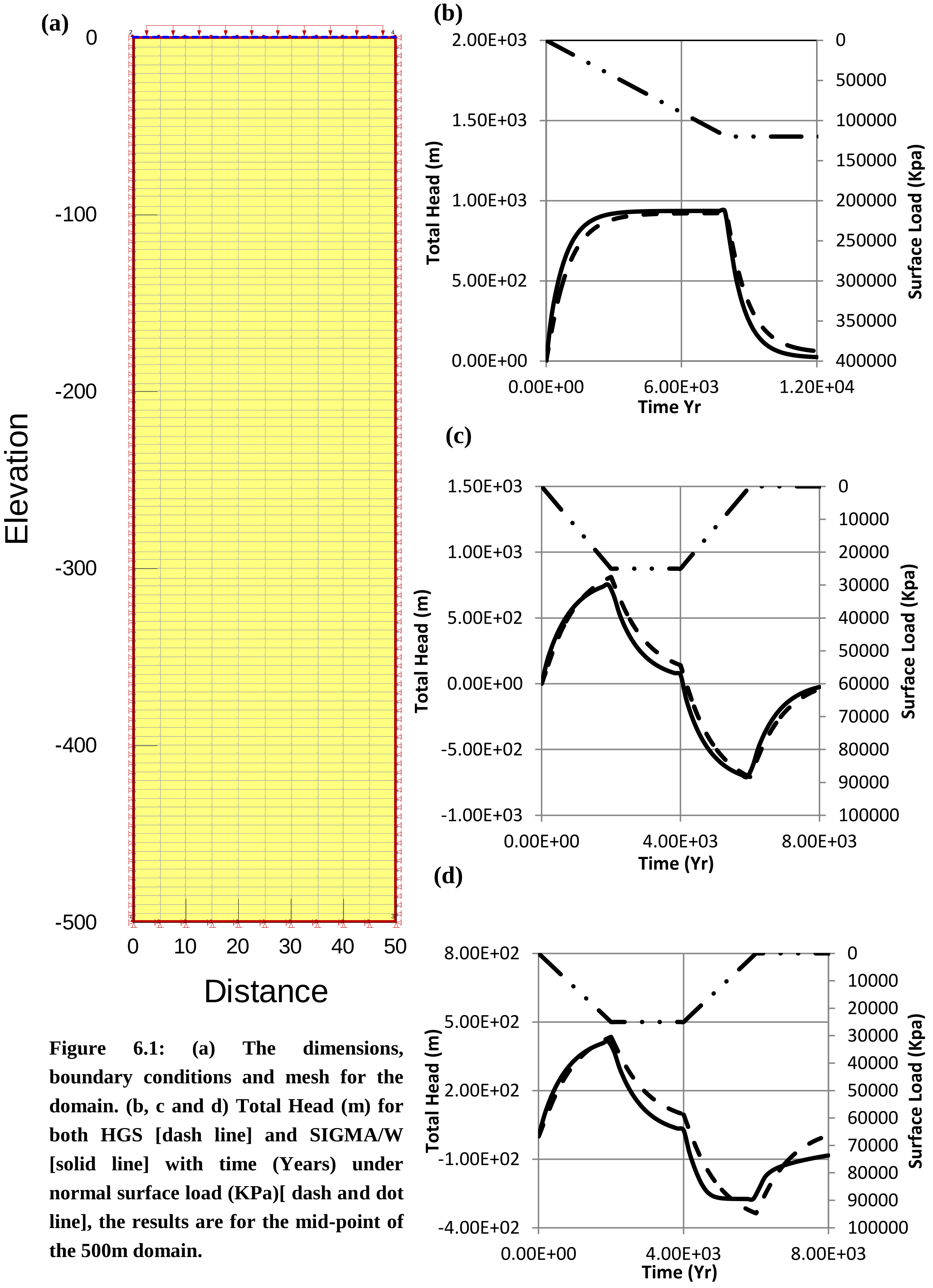

Figure 6.1: (a) The dimensions, boundary conditions and mesh for the domain. (b, c and d) Total Head (m) for both HGS [dash line] and SIGMA/W [solid line] with time (Years) under normal surface load (KPa)[dash and dot line], the results are for the mid-point of the 500m domain.

Table 6-1: Hydrogeological properties of the layer used in the numerical model.

Characteristics	Value
Ss	4.0E-7 m-1
KH	1.2E-6 m/yr
KZ/KH	1
E	24.0 GPa
Poisson’s ratio	0.21
Porosity	1.0%
Unit weight	24.5 KN/m3

7 Appendix II

7.1.1 The re-evaluation of the natural isotopic data from Benken area, Switzerland

A one-dimensional model was used to simulate field data from the Benken area in northeastern Switzerland. A HydoGeoSphere (HGS) model was built for the 312 m thick domain. The domain is in the Dogger low-permeability formations that are sandwiched between two aquifers, the Malm and the Keuper formations (Gimmi et al., 2007). These aquifers define the upper and the lower boundaries of the modeled domain. The lower boundary, the Keuper aquifer, had a significant flushing with meteoric water which may have started less than 2 Ma ago following the creation of new discharge areas. The upper boundary, the Malm aquifer, is characterized by a complex paleohydrogeologic evolution of its groundwater. It is difficult to define unique boundary conditions. The evolution time based on laboratory diffusion coefficients is determined from the Dogger formation of the order of 0.5–1 Ma with a possible range of about 0.2–2 Ma, which is geologically plausible.

The Base Case presented in the Gimmi et al. (2007) paper was simulated. The initial values in the Dogger formation were derived from maximum values in the upper part of the domain. Solute transport is limited to diffusion with constant concentrations at the boundaries.

The simulation was redone with the same parameters, e.g., diffusion coefficient, porosity and tortuosity. The simulation time given in the original simulation is 0.55Ma. To get the best fit using the HGS model the simulation time was modified for both the upper and lower boundaries. The upper boundary needed a time around 0.2Ma with a time around 0.8Ma for the lower boundary figure (7.1). Those times still fall in the geologically acceptable range. More geological investigations will be done for a better understanding of the solution.

7.1.2 The re-evaluation of the natural isotopic data from Tournemire (south France)

The domain of the Tournemire area is a 250 m-thick argillaceous formation of Toarcian and Domerian ages, surrounded by two carbonate aquifers, divided into seven sub-layers (Savoye et al., 2008). The assumptions that the initial argillite pore water was seawater trapped during the sedimentation of the clay-rich muds and the two bounding aquifers are karsts with an active circulation of groundwater of meteoric origin. Diffusion is assumed to have started right after the beginning of the karstification of the two surrounding carbonated aquifers.

Only diffusion was taken into account in the simulations, the advection term was negligible with respect to diffusion as showed by a previous study by (Patriarche et al., 2004a). The best simulations by (Savoye et al., 2008) considered an activation of the embedding aquifers 11–13 Ma ago, corresponding to the beginning of the diffusive process through the argillaceous formations. This is consistent with palaeo-hydrogeological evidence that aquifers embedding the Toarcian– Domerian shales were activated at 10 Ma (uncertainty range: 6–15 Ma) (Savoye et al., 2008).

A one dimensional numerical model was built to simulate this case using HGS. Seven different sub-layers were built with different pore diffusion coefficients and porosities. Several runs were done with different grid and time discritization and different run times. Figure (7.2) shows the best fit of between HGS simulation results and field data. The simulation time that gave the best fit was 11 Ma and that matches the Savoye et al., (2008) results.

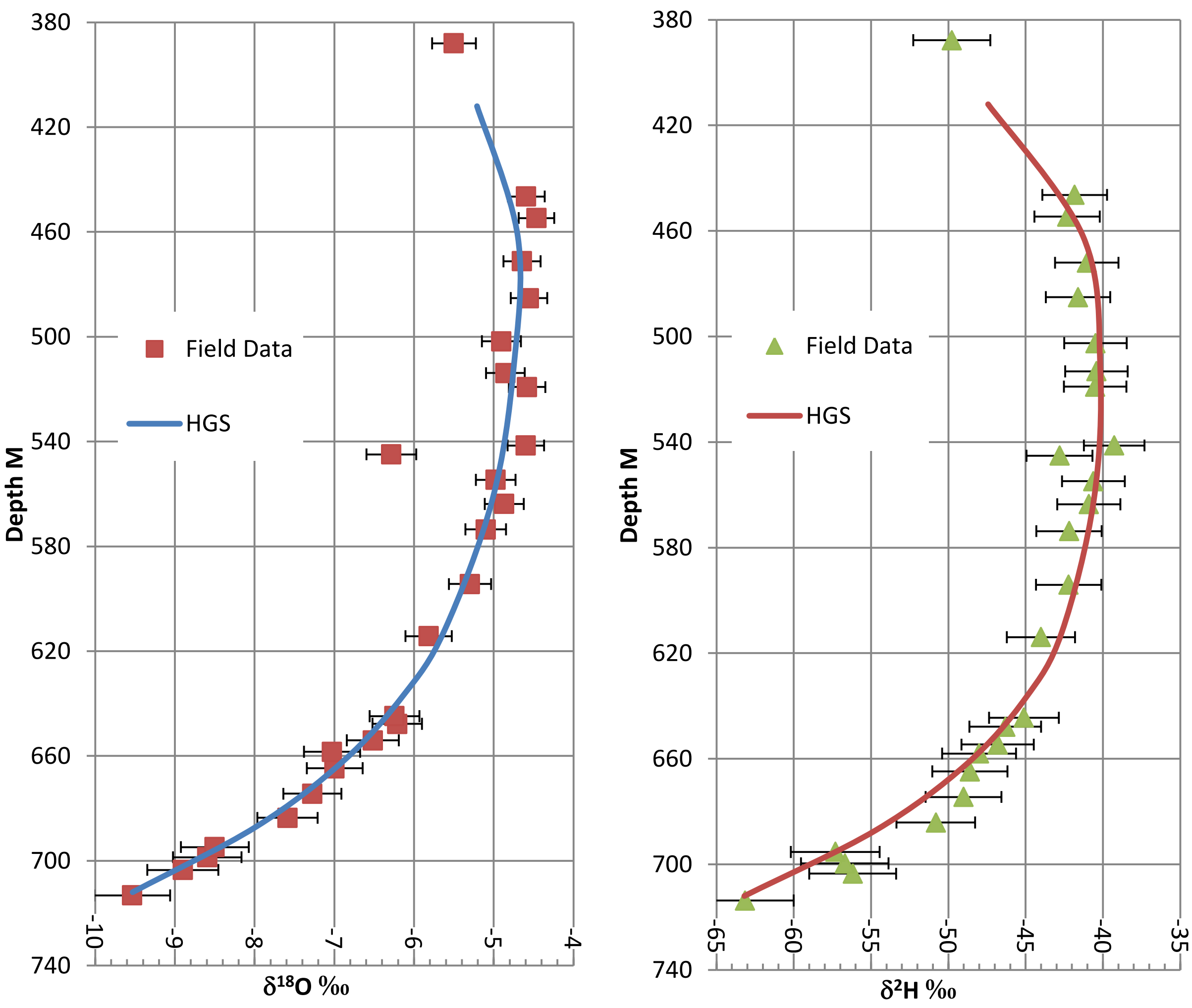

Figure 7.1: Best fit of the numerical model results of the Benken site.

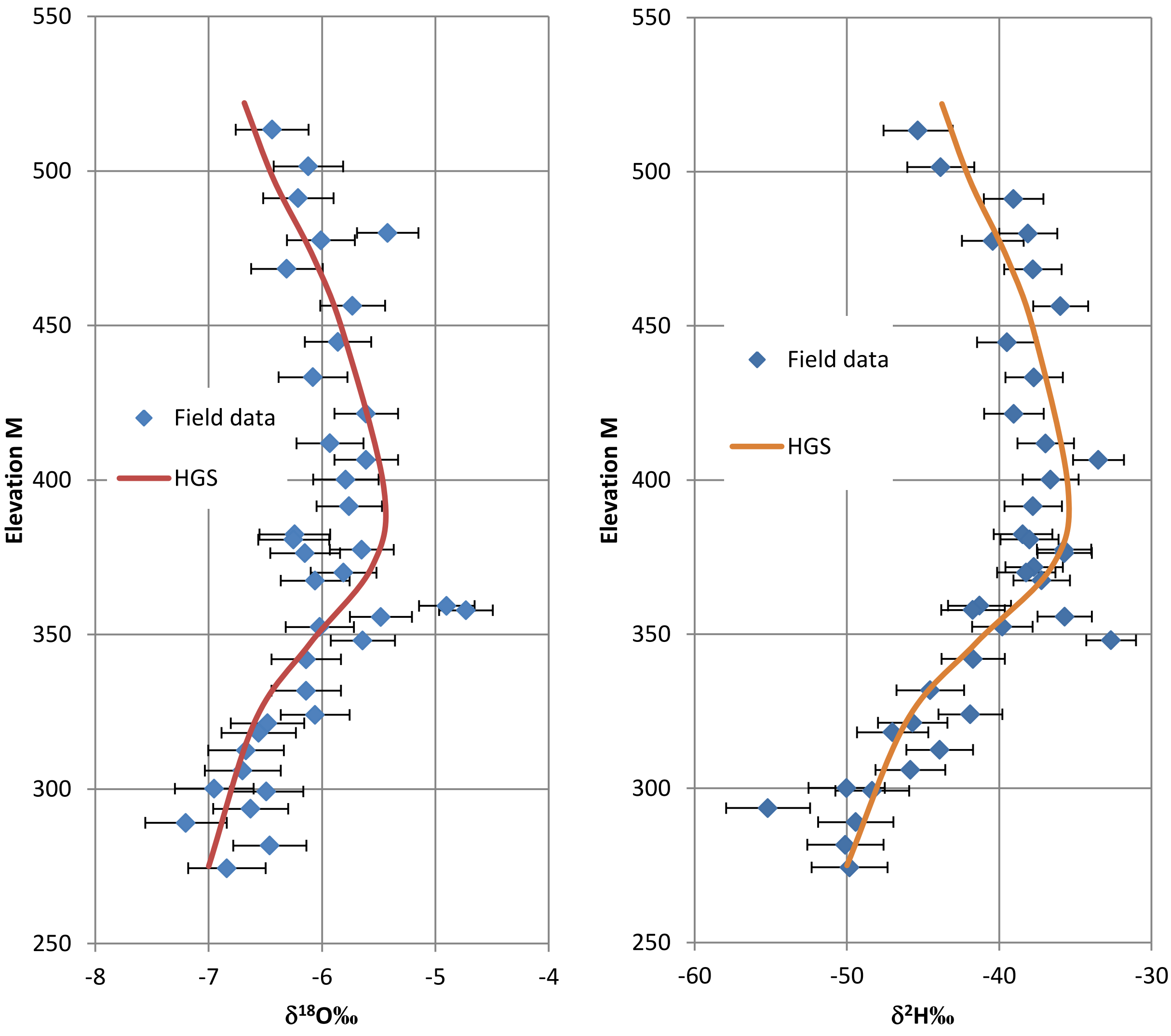

Figure 7.2: Best fit of the numerical model results of the Tournemire site.

8 Appendix III

8.1 Governing Equation

$$\theta\frac{\partial C}{\partial t}-\theta D_X\frac{\partial^2 C}{\partial X^2}-\theta D_Y\frac{\partial^2 C}{\partial Y^2}-\theta D_Z\frac{\partial^2 C}{\partial Z^2} = M\delta(t-t')\delta(X-X')\delta(Y-Y')\delta(Z-Z')$$

$$t>0,\qquad -\infty<X<+\infty,\qquad -\infty<Y<+\infty,\qquad -\infty<Z<+\infty \tag{I.A}$$

Initial condition is taken as

$$C(X,Y,Z,t=0)=0 \tag{I.B}$$

First type (Dirichlet) Boundary conditions are taken as

$$C(\pm\infty,Y,Z,t)=0 \tag{I.C}$$

$$C(X,\pm\infty,Z,t)=0 \tag{I.D}$$

$$C(X,Y,\pm\infty,t)=0 \tag{I.E}$$

8.1.1 Apply Exponential Fourier Transform in X

Apply Exponential Fourier Transform in X to equation (I.A):

$$\bar{C}(\propto_1,Y,Z,t)=\int_{-\infty}^{\infty}C(X,Y,Z,t)e^{-j\alpha_1 X}dX \tag{I.F}$$

Where
$$\mathcal{F}\left(\frac{\partial^2\theta C}{\partial X^2}\right)=-\propto_1^2\,\theta\bar{C} \tag{I.G}$$

This gives

$$\frac{\partial \bar{C}}{\partial t} + \propto_1^2 D_X \bar{C} - D_Y \frac{\partial^2 \bar{C}}{\partial Y^2} - D_Z \frac{\partial^2 \bar{C}}{\partial Z^2} - {}^{M}\!/_{\theta}\, \delta(t - t')\delta(Y - Y')\delta(Z - Z') \int_{-\infty}^{\infty} \delta(X - X') e^{-j\alpha_1 X} dX = 0 \tag{I.H}$$

$$\frac{\partial \bar{C}}{\partial t} + \propto_1^2 D_X \bar{C} - D_Y \frac{\partial^2 \bar{C}}{\partial Y^2} - D_Z \frac{\partial^2 \bar{C}}{\partial Z^2} - {}^{M}\!/_{\theta}\, \delta(t - t')\delta(Y - Y')\delta(Z - Z') e^{-j\alpha_1 X'} = 0 \tag{I.I}$$

Apply $\mathcal{F}_e$ to boundary conditions (I.D)

$$\mathcal{F}_e[C(X, \pm\infty, Z, t)] = \bar{C}(\propto_1, \pm\infty, Z, t) = 0 \tag{I.J}$$

Apply $\mathcal{F}_e$ to initial condition (I.B)

$$\mathcal{F}_e[C(X, Y, Z, 0)] = \bar{C}(\propto_1, Y, Z, 0) = 0 \tag{I.K}$$

8.1.2 Apply Exponential Fourier Transform in Y

Apply Exponential Fourier Transform in Y to equation (I.I):

$$\bar{\bar{C}}(\propto_1, \propto_2, Z, t) = \int_{-\infty}^{\infty} \bar{C}(\propto_1, Y, Z, t) e^{-j\alpha_2 Y} dY \tag{I.L}$$

This leads to

$$\frac{\partial \bar{\bar{C}}}{\partial t} + \propto_1^2 D_X \bar{\bar{C}} + \propto_2^2 D_Y \bar{\bar{C}} - D_Z \frac{\partial^2 \bar{\bar{C}}}{\partial Z^2} - {}^{M}\!/_{\theta}\, \delta(t - t')\delta(Z - Z') e^{-j\alpha_1 X'} e^{-j\alpha_2 Y'} = 0 \tag{I.M}$$

Apply $\mathcal{F}_e$ to boundary conditions

$$\mathcal{F}_e[\bar{C}(\propto_1, Y, \pm\infty, t)] = \bar{\bar{C}}(\propto_1, \propto_2, \pm\infty, t) = 0 \tag{I.N}$$

Apply $\mathcal{F}_e$ to initial condition (I.K)

$$\mathcal{F}_\mathrm{e}[\bar{\mathrm{C}}(\propto_1, \mathrm{Y}, \mathrm{Z}, 0)] = \bar{\bar{\mathrm{C}}}(\propto_1, \propto_2, \mathrm{Z}, 0) = 0 \tag{I.O}$$

8.1.3 Apply Exponential Fourier Transform in Z

Apply Exponential Fourier Transform in Z to equation (I.M):

$$\bar{\bar{\bar{\mathrm{C}}}}(\propto_1, \propto_2, \propto_3, \mathrm{t}) = \int_{-\infty}^{\infty} \bar{\bar{\mathrm{C}}}(\propto_1, \propto_2, \mathrm{Z}, \mathrm{t}) \mathrm{e}^{-\mathrm{j}\alpha_3 \mathrm{Z}} \mathrm{dZ} \tag{I.P}$$

This leads to

$$\frac{\partial \bar{\bar{\bar{\mathrm{C}}}}}{\partial \mathrm{t}} + \propto_1^2 \mathrm{D_X} \bar{\bar{\bar{\mathrm{C}}}} + \propto_2^2 \mathrm{D_Y} \bar{\bar{\bar{\mathrm{C}}}} - \propto_3^2 \mathrm{D_Z} \bar{\bar{\bar{\mathrm{C}}}} - {}^{\mathrm{M}}\!/_{\theta}\, \delta(\mathrm{t} - \mathrm{t}') \mathrm{e}^{-\mathrm{j}\alpha_1 \mathrm{X}'} \mathrm{e}^{-\mathrm{j}\alpha_2 \mathrm{Y}'} \mathrm{e}^{-\mathrm{j}\alpha_3 \mathrm{Z}'} = 0 \tag{I.Q}$$

Apply $\mathcal{F}_e$ to initial condition (I.O)

$$\mathcal{F}_\mathrm{e}[\bar{\bar{\mathrm{C}}}(\propto_1, \propto_2, \mathrm{Z}, 0)] = \bar{\bar{\bar{\mathrm{C}}}}(\propto_1, \propto_2, \propto_3, 0) = 0 \tag{I.R}$$

8.1.4 Apply Laplace Transform in t

Apply Laplace Transform in t to equation (I.Q):

$$\frac{\partial \bar{\bar{\bar{\mathrm{C}}}}}{\partial \mathrm{t}} + \propto_1^2 \mathrm{D_X} \bar{\bar{\bar{\mathrm{C}}}} + \propto_2^2 \mathrm{D_Y} \bar{\bar{\bar{\mathrm{C}}}} + \propto_3^2 \mathrm{D_Z} \bar{\bar{\bar{\mathrm{C}}}} - {}^{\mathrm{M}}\!/_{\theta}\, \delta(\mathrm{t} - \mathrm{t}') \mathrm{e}^{-\mathrm{j}\alpha_1 \mathrm{X}'} \mathrm{e}^{-\mathrm{j}\alpha_2 \mathrm{Y}'} \mathrm{e}^{-\mathrm{j}\alpha_3 \mathrm{Z}'} = 0 \tag{I.S}$$

Take

$$\mathrm{K}_1 = \propto_1^2 \mathrm{D_X} + \propto_2^2 \mathrm{D_Y} + \propto_3^2 \mathrm{D_Z} \tag{I.T}$$

$$\mathrm{K}_2 = \mathrm{e}^{-\mathrm{j}\alpha_1 \mathrm{X}'} \mathrm{e}^{-\mathrm{j}\alpha_2 \mathrm{Y}'} \mathrm{e}^{-\mathrm{j}\alpha_3 \mathrm{Z}'}\, {}^{\mathrm{M}}\!/_{\theta} \tag{I.U}$$

$$f = \overline{\overline{\overline{C}}} \tag{I.V}$$

This leads to

$$\frac{df}{dt} + K_1 f = K_2\, \delta(t - t') \tag{I.W}$$

The Laplace transform of

$$\mathcal{L}(f) = F(s) \tag{I.X}$$

$$\mathcal{L}\left(\frac{df}{dt}\right) = sF(s) - f(0) \tag{I.Y}$$

Where s is the Laplace transform variable.

Laplace transform of equation (I.W)

$$sF(s) - f(0) + K_1 F(s) = K_2 e^{-st'} \tag{I.Z}$$

Where the initial condition is

$$f(0) = f(\propto_1, \propto_2, \propto_3, 0) = 0 \tag{I.AA}$$

Rearrange the equation

$$F(s)(K_1 + s) = K_2 e^{-st'} \tag{I.BB}$$

$$F(s) = \frac{K_2 e^{-st'}}{(K_1 + s)} \tag{I.CC}$$

8.1.5 Inverse Laplace:

$$f = K_2 e^{-K_1 (t - t')} \tag{I.DD}$$

Substitute (I.T) & (I.U) in (I.DD)

$$f = {}^{M}/_{\theta}\, e^{-j\alpha_1 X'} e^{-j\alpha_2 Y'} e^{-j\alpha_3 Z'} e^{-(\propto_1^2 D_X + \propto_2^2 D_Y + \propto_3^2 D_Z)(t-t')} \qquad \text{(I.EE)}$$

$$\bar{\bar{\bar{C}}} = {}^{M}/_{\theta}\, e^{-j\alpha_1 X'} e^{-(\propto_1^2 D_X)(t-t')} e^{-j\alpha_2 Y'} e^{-(\propto_2^2 D_Y)(t-t')} e^{-j\alpha_3 Z'} e^{-(\propto_3^2 D_Z)(t-t')} \qquad \text{(I.FF)}$$

To invert in either $\propto_1, \propto_2$ *or* $\propto_3$, the following inverse is required:

(Churchill, Appendix C, pg 472 # 20)

$$\mathcal{F}_e^{-1}\left(e^{-C\alpha^2}\right) = \frac{1}{2(\pi C)^{1/2}} e^{-X^2/4C} \qquad \text{(I.GG)}$$

(Churchill, Appendix C, pg 471 # 5)

$$\mathcal{F}_e^{-1}\left(e^{-i\alpha k}\bar{f}(\alpha)\right) = f(X-k) \qquad \text{(I.HH)}$$

8.1.6 Inverse Fourier in $\propto_1$:

First, invert equation (I.FF) in $\propto_1$:

$$\bar{\bar{C}} = {}^{M}/_{\theta} \frac{1}{2\sqrt{\pi D_X (t-t')}} \exp\left[\frac{-(X-X')^2}{4D_X(t-t')}\right] e^{-j\alpha_2 Y'} * e^{-(\propto_2^2 D_Y)(t-t')} e^{-j\alpha_3 Z'} e^{-(\propto_3^2 D_Z)(t-t')} \qquad \text{(I.II)}$$

8.1.7 Inverse Fourier in $\propto_2$ and $\propto_3$:

The same was done to $\propto_2$ and $\propto_3$, and the final result is presented in equation (I.JJ)

$$C = \frac{M}{8\theta\pi^{1.5}\sqrt{D_X D_Y D_Z}(t-t')^{1.5}} \exp\left[\frac{-(X-X')^2}{4D_X(t-t')}\right] \exp\left[\frac{-(Y-Y')^2}{4D_Y(t-t')}\right] \exp\left[\frac{-(Z-Z')^2}{4D_Z(t-t')}\right] \qquad \text{(I.JJ)}$$

8.2 Integrate in Time:

To extend the solution from an instantaneous source to a time step source equation (I.JJ) was integrate with respect to t'(the time in which source is applied)from t'=0 to t'=t_1.

$$\int_0^{t_1} C\,dt' =$$

$$\int_0^{t_1} \frac{M}{8\theta\pi^{1.5}\sqrt{D_X D_Y D_Z}(t-t')^{1.5}} \exp[\frac{-(X-X')^2}{4D_X(t-t')}]\exp[\frac{-(Y-Y')^2}{4D_Y(t-t')}]\exp[\frac{-(Z-Z')^2}{4D_Z(t-t')}]\ dt' \tag{I.KK}$$

The result is equation (1.LL)

$$C = \frac{a}{\sqrt{b}}[\mathrm{erf}\left(\frac{\sqrt{b}}{\sqrt{(t-t_1)}}\right) - \mathrm{erf}\left(\frac{\sqrt{b}}{\sqrt{t}}\right)] \tag{I.LL}$$

Where

$$a = \frac{M}{8\theta\pi\sqrt{D_X D_Y D_Z} t_1} \tag{I.MM}$$

$$b = \frac{(X-X')^2}{4D_X} + \frac{(Y-Y')^2}{4D_Y} + \frac{(Z-Z')^2}{4D_Z} \tag{I.NN}$$

And erf is the error function and defined by

$$\mathrm{erf}(\alpha) = \frac{2}{\pi}\int_0^{\alpha} e^{-t^2}\,dt \tag{I.OO}$$

8.3 Integrate in X:

The result is extended from a spatial point source to a line in X direction. Equation (I.LL) is integrated with respect to X’ from X_1' to X_2'

$$\int_{X_1'}^{X_2'} C\,dX' = \int_{X_1'}^{X_2'} \frac{a}{\sqrt{b}}[\mathrm{erf}\left(\frac{\sqrt{b}}{\sqrt{(t-t_1)}}\right) - \mathrm{erf}\left(\frac{\sqrt{b}}{\sqrt{t}}\right)]\ dX' \tag{I.PP}$$

A new assumption was used where a new term $t_{X'}$ equation (I.QQ) is introduced.

$$t_{X'} = \frac{(X - X')^2}{4D_X} \tag{I.QQ}$$

The new integration limits are

$$\gamma_1 = \frac{(x - x_1')^2}{4D_X}, \gamma_2 = \frac{(x - x_2')^2}{4D_X} \tag{I.RR}$$

The new integration is shown in equation (I.SS)

$$\int_{\gamma_1}^{\gamma_2} C\, dt_{X'} = \int_{\gamma_1}^{\gamma_2} \frac{a}{\sqrt{t_{X'} + \frac{(Y - Y')^2}{4D_Y} + \frac{(Z - Z')^2}{4D_Z}}} [\operatorname{erf}\left(\frac{\sqrt{t_{X'} + \frac{(Y - Y')^2}{4D_Y} + \frac{(Z - Z')^2}{4D_Z}}}{\sqrt{(t - t_1)}}\right) - \operatorname{erf}\left(\frac{\sqrt{t_{X'} + \frac{(Y - Y')^2}{4D_Y} + \frac{(Z - Z')^2}{4D_Z}}}{\sqrt{t}}\right)]\, dt_{X'} \tag{I.SS}$$

The solution of integration is equation (I.TT)

$$C = \frac{2a}{(\gamma_2 - \gamma_1)} [\sqrt{b_x}\operatorname{erf}\left(\frac{\sqrt{b_x}}{\sqrt{T}}\right) + \sqrt{\frac{T}{\pi}}\exp\left(\frac{-b_x}{T}\right)] \tag{I.TT}$$

Where

$$b_x = \gamma_i + \frac{(Y - Y')^2}{4D_Y} + \frac{(Z - Z')^2}{4D_Z} \tag{I.UU}$$

Substitute in γ_i from γ_1 to γ_2 and in T from t to (t-t$_1$).

8.4 Integrate in Y:

The same procedure was done in Y direction where equation (I.TT) is integrated with respect to Y' form Y_1' to Y_2', in order to turn source line in to an area in X & Y plane.

The solution is presented in equation (I.VV).

$$\mathrm{C} = \frac{\mathrm{a}}{(\upbeta_2 - \upbeta_1)(\upgamma_2 - \upgamma_1)} [\mathrm{b_{xy}}^{1.5}\,\mathrm{erf}\left(\frac{\sqrt{\mathrm{b_{xy}}}}{\sqrt{\mathrm{T}}}\right) + \frac{4}{3}\sqrt{\frac{\mathrm{T}}{\uppi}}\exp\left(\frac{-\mathrm{b_{xy}}}{\mathrm{T}}\right)(\mathrm{b_{xy}} + \mathrm{T}) - \frac{2}{\sqrt{\uppi}}\mathrm{T}^{1.5}\exp\left(\frac{-\mathrm{b_{xy}}}{\mathrm{T}}\right)] \tag{I.VV}$$

Where

$$\upbeta_1 = \frac{(\mathrm{Y}-\mathrm{Y}_1')^2}{4\mathrm{D_Y}}, \upbeta_2 = \frac{(\mathrm{Y}-\mathrm{Y}_2')^2}{4\mathrm{D_Y}} \tag{I.WW}$$

$$\mathrm{b_{xy}} = \upgamma_\mathrm{i} + \upbeta_\mathrm{j} + \frac{(\mathrm{Z}-\mathrm{Z}')^2}{4\mathrm{D_Z}} \tag{I.XX}$$

Substitute in $\upgamma_\mathrm{i}$ from $\upgamma_1$ to $\upgamma_2$, and in β_j from β_1 to β_2, and T from t to (t-t_1).

8.5 Integrate in Z:

The same procedure was done in Z direction where equation (I.VV) is integrated with respect to Z’ form Z_1' to Z_2' , in order to turn area source in to a volume source.

The solution is presented in equation (I.YY).

$$\mathrm{C} = \frac{\mathrm{a}}{(\uptau_2 - \uptau_1)(\upbeta_2 - \upbeta_1)(\upgamma_2 - \upgamma_1)} [\frac{8}{15\sqrt{\uppi}}\exp\left(\frac{-\mathrm{b_{xyz}}}{\mathrm{T}}\right)\{\sqrt{\uppi}\,(\mathrm{b_{xyz}})^{2.5}\exp\left(\frac{\mathrm{b_{xyz}}}{\mathrm{T}}\right)\mathrm{erf}\left(\frac{\sqrt{\mathrm{b_{xyz}}}}{\sqrt{\mathrm{T}}}\right) + (\mathrm{b_{xyz}})^2\sqrt{\mathrm{T}} + 2\mathrm{b_{xyz}}\mathrm{T}^{1.5} + 2\mathrm{T}^{2.5}\} + \frac{4}{3\sqrt{\uppi}}\mathrm{T}^{1.5}\exp\left(\frac{-\mathrm{b_{xyz}}}{\mathrm{T}}\right)(\mathrm{b_{xyz}} + 2\mathrm{T}) - \frac{2}{\sqrt{\uppi}}\mathrm{T}^{2.5}\exp\left(\frac{-\mathrm{b_{xyz}}}{\mathrm{T}}\right)] \tag{I.YY}$$

Where $(\tau_2 - \tau_1)(\beta_2 - \beta_1)(\upgamma_2 - \upgamma_1) \neq 0 \;\; \forall\, X, Y, Z$

$$\uptau_1 = \frac{(\mathrm{Z}-\mathrm{Z}_1')^2}{4\mathrm{D_Z}}, \uptau_2 = \frac{(\mathrm{Z}-\mathrm{Z}_2')^2}{4\mathrm{D_Z}} \tag{I.ZZ}$$

$$\mathrm{b_{xyz}} = \upgamma_\mathrm{i} + \upbeta_\mathrm{j} + \uptau_\mathrm{l} \tag{I.AAA}$$

Substitute in γ_i from γ_1 to γ_2, and in β_j from β_1 to β_2, and in τ_l from τ_1 to τ_2 and T from t to (t-t_1).

9 APPENDIX IV

9.1 FORTRAN CODE

For equation (I.YY)

```
    program DIFF3D
!   COPYRIGHT OMAR KHADER 2010
!   Diffusion  Limited Transport, infinite domain
!   DEFINE VARIABLES
    IMPLICIT REAL*8 (A-H,O-Z)
    REAL*8 TS(5),XS(5),YS(5),ZS(5),C(5000),TYR(5000)
!   INPUT & OUTPUT FILES
    open(unit=6,file=’INPDF3D.inp’,status=’unknown’)
      open(unit=7,file='OUTDF3D.out',status='unknown')
!   READ THE VARIABLES
    Read(6,*) AMASS
    Read(6,*) DX
    Read(6,*) DY
    Read(6,*) DZ
    Read(6,*) RUNT
    Read(6,*) N
    Read(6,*) TSTEP
    Read(6,*) XSTART
    Read(6,*) XEND
    Read(6,*) YSTART
    Read(6,*) YEND
    Read(6,*) ZSTART
    Read(6,*) ZEND
    Read(6,*) POR
    Read(6,*) X
    Read(6,*) Y
    Read(6,*) Z
    PI=3.141592654
    TS(1)=0.0
    TS(2)=RUNT*31536000.0
    XS(1)=XSTART
    XS(2)=XEND
    YS(1)=YSTART
    YS(2)=YEND
    ZS(1)=ZSTART
    ZS(2)=ZEND
    ZERO=0.0
   ! XS(j)
   ! YS(k)
   ! ZS(m)
   ! TS(l)
    TX1=((X-XS(1))**2)/(4.0*DX)
    TX2=((X-XS(2))**2)/(4.0*DX)
    TY1=((Y-YS(1))**2)/(4.0*DY)
    TY2=((Y-YS(2))**2)/(4.0*DY)
    TZ1=((Z-ZS(1))**2)/(4.0*DZ)
    TZ2=((Z-ZS(2))**2)/(4.0*DZ)
    a=AMASS/(8.0*POR*PI*TS(2)*sqrt(DX*DY*DZ))
    TEMP11=(TX2-TX1)*(TY2-TY1)*(TZ2-TZ1)
    IF (TEMP11 .EQ. ZERO) THEN
    TEMP1=0.000000000000000001
    ELSE
```

```
    TEMP1=TEMP11
    ENDIF
    do 200 i=1,n
    TYR(i)=TSTEP*i
    TSEC=TYR(i)*31536000.0
    C(i)=0
    do 500 m=1,2
    do 400 k=1,2
    do 300 j=1,2
    do 600 l=1,2
    T=TSEC-TS(l)
    bXYZ=((X-XS(j))**2)/(4.0*DX)+((Y-YS(k))**2)/(4.0*DY)+((Z-
ZS(m))**2)/(4.0*DZ)
    TEMP1=(TX2-TX1)*(TY2-TY1)*(TZ2-TZ1)
    b=EXP(-bXYZ/T)
    TEMP2=a/TEMP1
    TEMP3=8.0/(15.0*SQRT(PI))*EXP(-bXYZ/T)
    CALL EXPERF(ZERO,SQRT(bXYZ)/SQRT(T),RES)
    RR=1.0-RES
    TEMP9=8.0/15.0*RR
    TEMP8=bXYZ*bXYZ*SQRT(bXYZ)
    TEMP4=TEMP9*TEMP8
    TEMP5=(bXYZ**2)*SQRT(T)+2.0*bXYZ*(T**1.5)+2*(T**2.5)
    TEMP6=4.0/(3.0*SQRT(PI))*(T**1.5)*(bXYZ+2.0*T)*EXP(-bXYZ/T)
    TEMP7=(2.0/SQRT(PI))*(T**2.5)*EXP(-bXYZ/T)
    TEMPC=(TEMP2*(TEMP4+(TEMP3*TEMP5)-TEMP6+TEMP7))
    CSIGN=((-1)**l)*((-1)**j)*((-1)**k)*((-1)**m)*TEMPC
    C(i)=C(i)+CSIGN
600 continue
300 continue
400 continue
500 continue
    write(7,*) TYR(i),C(i)
200 continue
    end program DIFF3D
!     ****************************************************************
!
      SUBROUTINE EXPERF(XX,YY,ZZ)
      implicit real*8(a-h,o-z)
      REAL*8 NN,N,XX,YY,ZZ
!
!     THIS SUBROUTINE TAKES EXP(X)*ERFC(Y)  = Z
!
!     THIS SUBROUTINE IS INTENDED FOR HANDLING LARGE VALUES OF X AND Y
!     THEN USING A ASYMPTOTIC EXPANSION FOR ERFC.
      ZZ=0.
      YD=ABS(YY)
      PI = 3.14159265358
!     FOR LARGE POSITIVE VALUES OF Y, ERFC(Y) -> 0.
      EXY2 = XX-YY*YY
      IF(EXY2.LE.-30.0) RETURN
!     FOR LARGE NEGATIVE VALUES OF Y, ERFC(Y) -> 2.
      IF(YY.LT.-7.5)GOTO 500
!     THE ASYMPTOTIC  ERFC(Y)  EXPANSION IS VALID TOO  12 PLACES IF
!     Y > 7.5
      IF((YY.LE.7.5).AND.(XX.LE.30.0)) ZZ= DEXP(XX)*DERFC(YY)
      IF((YY.LE.7.5).AND.(XX.LE.30.0)) RETURN
!
      SUM = 1.0
      DENOM = 2.0*YD*YD
      TERM0=1.
```

```
      I=1
30    CONTINUE
      I=I+1
      IF(I.GE.12) GO TO 100
      N = I
      IF(ABS(TERM0/SUM).LE.1.E-15) GO TO 100
      TERM = TERM0*(-1.0)*(2.0*N-3.0)/DENOM
!     AS SOON AS THE NEWLY COMPUTED TERM BECOMES LARGER THEN THE
!     PREVIOUS ONE, STOP THE SUMMATION.
      IF(ABS(TERM).GE.ABS(TERM0)) GO TO 100
      SUM = SUM + TERM
      TERM0 = TERM
      GO TO 30
100   CONTINUE
      SUMY=SUM/YD
      IF(YY.LT.0.0)SUMY=2.-SUMY
      IF(EXY2.LT.30.0) ZZ=DEXP(EXY2)*SUMY/DSQRT(PI)
      IF(EXY2.LT.30.0) RETURN
!     FOR  X-Y*Y > 30.0   , BREAK UP THE EXPONENT INTO N TERMS
      NNUM = EXY2/50.0
      NN=NNUM
      EXY2N = EXY2/NN
      SUMN=(SUMY/SQRT(PI))**(1.0/NN)
      TERM=1.0
      DO 300 I=1,NNUM
      TERM=TERM*DEXP(EXY2N)*SUMN
300   CONTINUE
      ZZ= TERM
      RETURN
500   CONTINUE
!     FOR LARGE NEGATIVE VALUES OF Y, ERFC(Y) -> 2.
      IF(XX.LT.-30.0) ZZ=0.
      IF(XX.LT.-30.0)  RETURN
      ZZ=DEXP(XX)*2.0
      RETURN
      END
!
!     ROUTINE FOR ERFC(ARG) BY SERIES EXPANSION
!     DOUBLE PRECISION VERSION
!     PROGRAMMED BY E.A. SUDICKY
!
      FUNCTION DERFC(ARG)
      IMPLICIT REAL*8 (A-H,O-Z)
      INTEGER*2 IL,LJL,JLJ
      PI = 3.14159265358D0
      SUMXOX=1.D0
      XOX=DABS(ARG)
      IF(XOX.GT.3.4D0)GOTO 5160
!
!     THIS SERIES EXPANSION IS FOR ARG < = 3.4
!
      FACT=1.D0
      IL=1
      UOX=XOX*XOX
      US=UOX
5085  FACT=FACT*IL
      ZOZ=-1.D0
      IF((IL/2)*2.EQ.IL)ZOZ=1.D0
      TXOX=UOX/((2.D0*IL+1.D0)*FACT)
      SUMXOX=SUMXOX+ZOZ*TXOX
      UOX=UOX*US
```

```
      IL=IL+1
!
!     STOP THE SUMMATION WHEN THE CURRENT TERM
!     IS LESS THAN 1E-20
!
      IF(TXOX.GT.1.D-20)GOTO 5085
      DERFC=1.D0-2.D0*XOX/DSQRT(PI)*SUMXOX
      IF(ARG.LT.0.0D0)DERFC=2.D0-DERFC
      GOTO 5430
5160  IF(XOX.GT.14.D0)GOTO 5410
!
!     THIS SERIES EXPANSION IS FOR ARG > 3.4
!
      UOX=2.D0*XOX*XOX
      LJL=1
      JLJ=1
      FACT=1.D0
5300  OLDFAC=FACT
      FACT=FACT/UOX*JLJ
!
!     STOP THE SUMMATION WHEN THE CURRENT TERM BECOMES LARGER
!     THAN THE PREVIOUS TERM
!
      IF(FACT.GT.OLDFAC) GOTO 5333
      ZOZ=-1.D0
      IF((LJL/2)*2.EQ.LJL)ZOZ=1.D0
      TXOX=ZOZ*FACT
      SUMXOX=SUMXOX+TXOX
      LJL=LJL+1
      JLJ=JLJ+2
5333  DERFC=DEXP(-XOX*XOX)/DSQRT(PI)/XOX*SUMXOX
      GOTO 5420
5410  DERFC=0.D0
5420  IF(ARG.LT.0.D0)DERFC=2.D0-DERFC
5430  RETURN
      END
```

9.2 INPUT FILE SAMPLE

Table 9-1 A sample of input data of FORTRAN code

1000	!MASS KG
0.0000000001	!DX M^2/S
0.0000000001	!DY M^2/S
0.0000000001	!DZ M^2/S
50	!t YR
5000	!#TIME INTERVALS
20	!TIME STEP YR
-1	!XSTART M
1	!XEND M
-1	!YSTART M
1	!YEND M
-1	!ZSTART M

```
1                    !ZEND     M
0.13                 !POROSITY
25                   !X        M
25                   !Y        M
25                   !Z        M
```

9.3 OUTPUT SAMPLE FOR FORTRAN CODE

The output concentration in Figure 8.1 is for the above input data.

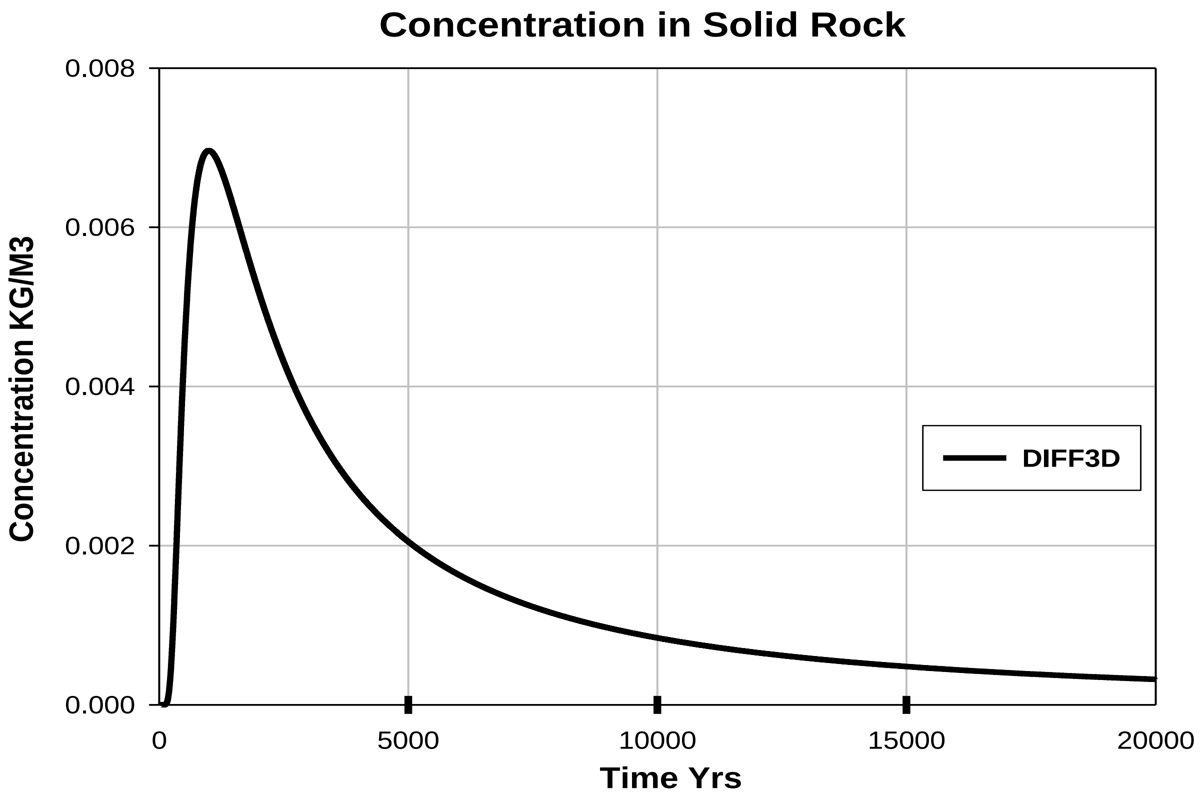

Figure 9.1: The Fortran Code Output, Solute concentration at a Target 25m from source VS Time

10 Appendix V

	US-8				DGR-1/2				DGR-3					DGR-4					DGR-5				DGR-6			
	Depth	**18O**	**2H**	**d**	**Depth**	**18O**	**2H**	**d**	**Depth**	**Normalized Depth**	**18O**	**2H**	**d**	**Depth**	**Normalized Depth**	**18O**	**2H**	**d**	**Normalized Depth**	**18O**	**2H**	**d**	**Normalized Depth**	**18O**	**2H**	**d**
Porewater	**40.6**	-10.99	-76.40	11.52	**101.89**	-12.16	-93.03	4.22	161.67	**142.91**	-13.82	-103.77	6.80	110.32	**108.57**	-14.13	-106.20	6.80	**314.527**	-9.765	-57.78	20.34	**315.918**	-8.37	-66.14	0.82
	19.3	-10.54	-73.60	10.72	**101.99**	-10.74	-86.65	-0.72	187.72	**169.72**	-11.19	-106.27	-16.70	180.99	**182.26**	-10.21	-97.30	-15.60	**320.621**	-10.5337	-90.6996	-6.4301	**319.949**	-8.635	-82.8825	-13.8025
	93.1	-11.28	-77.90	12.34	**102.26**	-10.75	-86.36	-0.36	198.96	**181.13**	-7.98	-78.79	-15.00	243.44	**241.36**	-10.34	-64.70	18.00	**322.971**	-9.8235	-90.3443	-11.7563	**321.674**	-7.7825	-98.1075	-35.8475
	85.5	-11.63	-82.10	10.94	**102.26**	-9.96	-82.37	-2.67	207.94	**190.39**	-7.98	-69.76	-5.90	304.05	**303.92**	-10.23	-61.10	20.70	**325.035**				**323.21**			
	75.7	-10.82	-76.40	10.16	**156.56**	-6.97	-63.47	-7.73	227.45	**210.48**	-8.75	-76.90	-6.90	369.7	**369.03**	-9.91	-91.60	-12.30	**326.063**				**323.84**			
	68.1	-11.50	-81.70	10.30	**172.32**	-10.40	-102.75	-19.57	248.47	**230.45**	-10.27	-72.79	9.40						**326.961**				**324.85**	-13.7775	-97.8833	12.33667
	54.4	-12.14	-83.80	13.32	**182.89**	-8.56	-88.57	-20.07	270.29	**250.26**	-10.81	-72.55	13.90						**329.394**				**325.8**	-13.8025	-95.16	15.26
	137.6	-15.30	-112.10	10.30	**197.45**	-8.97	-72.69	-0.93	274.38	**255.66**	-11.89	-63.11	32.00	386.31	**384.47**	-4.46	-65.80	-30.10	**335.419**	-11.4013	-90.7604	0.449791	**331.015**	-10.2933	-93.5867	-11.24
	120.8	-12.90	-92.00	11.20	**226.27**	-8.82	-75.21	-4.65	298.73	**285.94**	-11.43	-56.74	34.70	418.95	**418.33**	-2.40	-41.50	-23.20	**344.589**	-11.4642	-81.1595	10.55382	**339.907**	-11.61	-98.385	-5.505
	115.7	-13.30	-91.40	15.00	**249.33**	-11.02	-61.36	26.76	311.79	**299.72**	-9.69	-68.73	8.80	442.58	**443.17**	-1.03	-56.70	-48.46	**371.624**	-7.10494			**368.837**	-8.3875	-75.0375	-7.9375
	109.6	-13.29	-94.20	12.12	**294.84**	-8.56	-64.33	4.15	335	**321.41**	-8.46	-85.50	-17.80	469.13	**469.69**	-2.47	-44.80	-25.00	**374.499**				**370.642**	-8.5575	-76.03	-7.57
	101.9	-14.50	-105.00	11.00	**294.84**	-8.47	-70.73	-2.95	348.31	**335.28**	-14.08	-102.07	10.60	508.95	**508.03**	-2.39	-42.70	-23.60	**377.237**				**373.528**	-7.99	-72.2575	-8.3375
	179.4	-14.28	-102.10	12.14	**370.93**	-7.13	-58.52	-1.45	379.89	**367.07**	-10.52	-70.35	13.80	549.21	**548.65**	-3.60	-41.90	-13.20	**377.564**				**377.801**	-8.2325	-66.7775	-0.9175
	170.2	-13.87	-98.80	12.16	**395.29**	-6.60	-55.15	-2.39						595.38	**595.97**	-3.22	-42.10	-16.40	**385.593**	-6.16057	-55.4006	-6.11603	**383.544**	-7.5425	-58.7075	1.6325
	158	-16.60	-118.80	14.00	**422.4**	-3.52	-47.12	-18.96						625.37	**625**	-3.86	-42.90	-12.10	**390.114**	-5.48667	-53.6913	-9.79798	**389.028**	-6.7725	-58.95	-4.77
	150.4	-15.47	-111.40	12.36	**445.6**	-2.71	-47.28	-25.60	399.31	**385.90**	-5.61	-51.08	-6.20	643.15	**641.48**	-3.58	-44.60	-16.00	**395.003**	-4.76	-27.13	10.95	**394.924**	-3.3475	-49.15	-22.37
	143.7	-15.40	-112.70	10.50	**453.95**	-3.61	-45.30	-16.38	417.6	**404.80**	-1.93	-47.76	-32.30	654.3	**652.73**	-5.89			**402.48**	-1.10422	-45.3873	-36.5536	**398.923**	-2.275	-47.68	-29.48
	193.1	-13.37	-95.70	11.26	**459.62**	-3.12	-47.21	-22.28	432.79	**420.63**	-2.30	-45.95	-27.60	663.25	**661.32**	-4.59	-70.30	-34.30	**406.781**	-1.70939	-45.0282	-31.353	**403.935**	1.2575	-18.125	-28.185
					485.4	-3.80	-48.52	-18.15	445.08	**432.47**	-3.30	-48.54	-22.10	669.18	**667.49**	-3.26	-54.80	-28.80	**409.352**	-0.45	-35.215	-31.615	**409.314**	-2.4175	-47.6	-28.26
					513.35	-3.94	-50.69	-19.17	462.01	**452.43**	-3.02	-45.08	-20.90	671.02	**669.4**	-3.75	-50.60	-20.60	**414.491**	-5.49831	-59.1169	-15.1304	**414.91**	-3.045	-48.525	-24.165
					538.51	-3.53	-48.16	-19.92	478.13	**467.67**	-2.80	-49.35	-27.00	681.9	**680.72**	-4.52			**421.256**	-4.88958	-49.8023	-10.6856	**421.009**	-3.5825	-51.3375	-22.6775
					551.75	-3.68	-47.20	-17.78	496.75	**485.26**	-2.57	-47.39	-26.80	704.12	**703.06**	-4.47	-66.10	-30.40	**432.855**	-3.88898	-46.9667	-15.8549	**426.53**	-2.81333	-54.05	-31.5433
					578.15	-3.65	-47.16	-17.98	517.3	**504.68**	-3.24	-49.08	-23.10	716.15	**714.96**	-5.00	-64.90	-25.00	**437.553**	-2.87876	-48.6322	-25.6021	**431.766**	-5.72	-75.87	-30.11
					591.33	-3.58	-50.71	-22.09	539.46	**526.26**	-2.54	-49.54	-29.30	725.92	**724.76**	-6.04	-43.90	4.50	**440.848**	-1.96667	-40.99	-25.2567	**437.4**	-3.10667	-55.6967	-30.8433
					612.09	-3.54	-49.46	-21.16	559.95	**547.26**	-3.23	-50.50	-24.60	740.63	**739.53**	-5.34			**456.522**	-4.19219	-48.2069	-14.6694	**571.887**	-4.28971	-48.3883	-14.0706
					628.18	-4.46	-49.43	-13.73	581.28	**569.12**	-3.90	-53.67	-22.50	768.52	**767.33**	-5.91	-46.30	0.90	**472.359**	-3.81628	-46.9466	-16.4164	**578.38**	-3.73144	-45.2226	-15.3711
					634.49	-5.25	-50.95	-8.93	604.99	**593.42**	-3.46	-55.87	-28.20	772.19	**770.88**	-4.03	-32.10	-2.10	**472.359**	-4.685	-50.025	-12.545	**578.666**	-3.9234	-46.7906	-15.4034
					641.92	-4.67	-48.64	-11.30	629.38	**617.72**	-4.46	-59.52	-23.80	792.29	**790.64**	-7.94			**483.142**	-4.29189	-48.2865	-13.9514	**579.213**	-3.63836	-47.2188	-18.112
					648.75	-5.54	-56.54	-12.19	641	**628.76**	-4.47	-56.38	-20.60	801.1	**799.68**	-7.70	-39.20	22.40	**513.717**	-3.88646	-45.4365	-14.3449	**596.388**	-4.83489	-48.4127	-9.73356
					663.34	-6.43	-51.36	0.04	651.99	**639.20**	-4.50	-51.51	-15.50	816.24	**815.23**	-4.95	-35.40	4.20	**520.686**	-3.18094	-45.8612	-20.4137	**608.599**	-4.18002	-48.0919	-14.6517
					670.48	-5.83	-54.17	-7.55	662.21	**649.26**	-5.50	-59.06	-20.50	822.35	**821.5**	-7.36	-36.80	22.00	**552.586**	-4.59486	-45.9528	-9.19393	**652.86**	-5.4125	-49.64	-6.34
					681.45	-5.50	-51.79	-7.76	675.69	**662.27**	-4.97	-48.91	-9.20	842.27	**841.93**	-7.59	-36.90	23.90	**578.278**	-4.70555	-48.4416	-10.7972	**659.468**	-8.015	-78.41	-14.29
					689.45	-5.57	-57.80	-13.26	680.46	**667.17**	-5.03	-52.67	-12.40	845.65	**845.35**	-3.74	-32.90	-2.90	**601.561**	-4.38536	-47.4954	-12.4125	**667.896**	-6.16	-50.935	-1.655
					694.63	-5.38	-50.92	-7.86	687.1	**674.01**	-5.71	-48.01	-2.30	852.77	**852.47**	-4.09	-33.10	-0.40	**622.554**	-4.4964	-47.3265	-11.3554	**670.06**	-6.885	-57.8425	-2.7625
					699.58	-6.89	-55.47	-0.38	691.7	**678.74**	-5.23	-52.31	-10.50						**634.427**	-4.88509	-48.567	-9.48634	**674.638**	-5.02	-44.88	-4.72
					709.21	-6.73	-50.79	3.05	702.54	**689.78**	-5.50	-72.33	-28.30						**648.302**	-4.99575	-50.1777	-10.2117	**676.921**	-5.055	-30.0225	10.4175
					724.16	-7.70	-50.38	11.24	723.88	**710.38**	-6.18	-46.75	2.70						**665.604**	-5.35667	-38.15	-3.62	**681.895**	-6.32	-57.025	-6.465
					733.48	-6.54	-46.65	5.68	737.74	**724.06**	-6.23	-54.42	-4.90						**669.808**	-5.84	-56.4675	-9.7475	**686.141**			
					742.61	-8.73	-60.02	9.78	752.61	**738.96**	-5.45	-53.47	-9.90						**674.676**	-4.92667	-23.2067	16.20667	**692.076**	-5.8725	-38.02	8.96
					762.19	-7.72	-50.37	11.39	765.95	**752.33**	-7.25	-64.04	-6.80						**680.646**	-5.3675	-26.4875	16.4525	**694.282**	-6.29	-48.4833	1.836667
					797.5	-8.37	-45.77	21.20	783.2	**769.38**	-5.70	-40.57	5.00						**683.612**	-4.335	-21.8033	12.87667	**715.76**	-6.82667	-23.9	30.71333
					822.42	-8.78	-49.30	20.94	800.18	**785.91**	-8.32	-50.43	16.10						**686.334**	-5.40667	-42.74	0.513333	**715.76**	-6.3775	-31.2825	19.7375
					828.01	-5.28	-44.17	-1.97	814.42	**800.68**	-6.45	-47.62	4.00						**694.511**	-4.84667	-42.6	-3.82667	**723.09**	-7.6725	-43.4425	17.9375
					834.05	-5.84	-45.79	0.95	832.25	**819.16**	-7.96	-56.46	7.20						**696.501**	-4.89667	-37.65	1.523333	**729.32**	-7.7625	-62.1475	-0.0475
					835.73	-5.65	-48.14	-2.94	851.96	**839.71**	-6.31	-45.87	4.60						**704.338**	-4.34	-43.06	-8.34	**733.67**	-7.975	-42.5825	21.2175
					836.63	-5.94	-40.19	7.31	855.66	**843.96**	-5.35	-51.19	-8.40						**730.607**	-6.855	-41.3325	13.5075	**739.85**	-7.26977	-46.7933	11.3649
					839.69	-5.99	-44.62	3.30											**735.784**	-7.9575	-42.4075	21.2525	**744.06**	-7.89423	-47.9492	15.20468
					857.71	-4.73	-40.78	-2.92											**741.869**	-6.985	-32.625	23.255	**748.62**	-7.8624	-49.0575	13.84168
																			747.171	-7.84888	-49.5078	13.28329	**750.04**	-8.79	-70.2425	0.0775
																			753.648	-8.23667	-45.1567	20.73667	**758.94**	-6.9525	-20.4875	35.1325
																			753.648	-8.21976	-51.3775	14.38057	**761**			
																							764.07	-6.07333	-31.9033	16.68333
																							769.2	-8.705	-38.175	31.465
																							779.775	-9.565	-44.59	31.93
Groundwater					**844.73**	-4.97	-43.30	-3.48	339.66	**326.57**	-14.40	-104.30	10.90	327.08	**326.50**	-14.50	-102.70	-14.50								
					852.7	-4.71	-35.80	1.94	389.99	**376.92**	-2.30	-48.10	-29.70	377.42	**376.02**	-2.70	-50.00	-28.40								
									860.53	**848.83**	-4.80	-31.70	6.70	848.5	**848.20**	-5.20	-35.20	6.40								

Reproduced from (Raven et al, 2011 and Al et al., 2011)

11 Disclaimer

The Canadian Nuclear Safety Commission is not responsible for the accuracy of the statement made, or opinions expressed in this publication, and do not assume liability with respect to any damage or loss incurred as results of the use made of the information contained in this publication.